

Extensions Beyond Standard Models

by

Clemens Adolphs

A THESIS SUBMITTED IN PARTIAL FULFILLMENT OF
THE REQUIREMENTS FOR THE DEGREE OF

DOCTOR OF PHILOSOPHY

in

The Faculty of Graduate and Postdoctoral Studies

(Physics)

THE UNIVERSITY OF BRITISH COLUMBIA

(Vancouver)

April 2016

© Clemens Adolphs 2016

Abstract

In this thesis, we investigated a set of theoretical models frequently used in the field of solid state physics. These models describe coupling of charge carriers to bosonic modes such as phonons or magnons. In particular, the Holstein model describes coupling of charge carriers to dispersionless phonons, whereas the Emery model describes coupling of charge carriers to magnons in hole-doped antiferromagnets.

For the Holstein-like models, we studied how extending the model of the coupling beyond terms that are merely linear in the lattice distortion affects the ground state properties. Using appropriate extensions of the momentum average approximation, we could show that even small nonlinearities have a dramatic effect on the resulting quasi-particle's properties. We further investigated a particular type of nonlinear coupling, the double-well coupling model. After studying the properties of a single quasi-particle, we also showed that this system allows the formation of bound states between two charge carriers and a phonon cloud, the so-called bi-polaron. In contrast to the linear variation of the Holstein model, the resulting bi-polaron can be strongly bound yet lightweight.

For the Emery model, we consider an experimentally relevant extension. The original model describes a single layer of CuO_2 , relevant for the hole-doped cuprate superconductors. We consider recently synthesized layers of CuO , which can be viewed as two intercalated layers of CuO_2 . The resulting system is similar to CuO_2 , but different in important aspects. We use a variational method similar in spirit to MA but applicable to magnons instead of phonons to obtain the system's dispersion and compare it to that of the original CuO_2 layer. We observe a discrepancy between these dispersions that cannot be accounted for with a single-band model that is

Abstract

commonly used to model the CuO_2 dispersion. However, it has been a long-standing question whether or not this and other single-band models are appropriate for the description of cuprate physics. With our study of CuO , we demonstrated how a careful experimental analysis of this system can resolve that question.

Preface

- A version of the work discussed in chapter 2 is published as “C.P.J. Adolphs and M. Berciu, Europhysics Letters **102**, 47003 (2013)”. It relies on and advances further the techniques introduced previously by Professor M. Berciu published in [1] as well as techniques jointly developed in our group by M. Moeller, A. Mukherjee, C.P.J. Adolphs, D.J.J. Marchand and M. Berciu in [2].
- The work discussed in chapter 3 is published as “C.P.J. Adolphs and M. Berciu, Physical Review B **89**, 035122 (2014). It is based on the same techniques as cited above.
- The work presented in chapter 4 is published as “C.P.J. Adolphs and M. Berciu, Physical Review B **90**, 085149 (2014). It is based on the same previous work as cited above.
- A manuscript of the work discussed in 5 has been accepted for publication by Physical Review Letters and is expected to be published by the end of February 2016. It presents an extension of the work done in [3] and [4].

I carried out all the necessary analytical and numerical work for all four projects. I wrote the first drafts for all the manuscripts. Prof. M. Berciu assisted in the preparation of the final drafts of these works. The draft for the final project, currently under review for publication in Physical Review Letters, was also assisted by S. Moser and G.A.W. Sawatzky.

Table of Contents

Abstract	ii
Preface	iv
Table of Contents	v
List of Tables	viii
List of Figures	ix
Acknowledgements	xix
1 Introduction	1
1.1 Model Hamiltonians	2
1.2 The Holstein model for electron-phonon coupling	3
1.3 The three-band Emery model for a cuprate layer	21
1.4 Outline	26
2 Nonlinear Holstein model	29
2.1 Introduction	29
2.2 Model	31
2.2.1 Summary of model assumptions	33
2.3 Formalism	34
2.4 Results and discussion	38
2.4.1 Atomic limit	39
2.4.2 Negative nonlinear term	44
2.4.3 Small carrier concentrations	45

Table of Contents

2.4.4	Other types of el-ph coupling	48
2.5	Concluding remarks	48
3	Quadratic Holstein model	49
3.1	Introduction	49
3.2	Model	50
3.2.1	Summary of model assumptions	56
3.3	Formalism	57
3.3.1	The even sector	59
3.3.2	The odd sector	62
3.4	Results	62
3.4.1	Atomic limit: $t = 0$	62
3.4.2	Finite hopping	67
3.5	Summary and discussions	74
4	Bipolarons in the quadratic Holstein model	76
4.1	Introduction	76
4.2	Model	77
4.2.1	Summary of model assumptions	79
4.3	Formalism	80
4.3.1	Momentum average approximation	81
4.3.2	Exact diagonalization	84
4.4	Results	85
4.5	Conclusions and outlook	91
5	Single-polaron dispersion in the insulating limit of tetrago- nal CuO	94
5.1	Introduction	94
5.2	Model	97
5.2.1	Summary of model assumptions	101
5.3	Method	102
5.4	Results and discussion	104
5.4.1	The ZRS Bloch state	106
5.4.2	Low-energy effective model	107

Table of Contents

5.4.3 Comparison to ARPES	113
6 Conclusions	116
6.1 Summary of this work	116
6.2 Further developments	117
Bibliography	120
 Appendices	
A Various formal methods	136
B Appendix for Nonlinear Holstein Model	137
B.1 Free propagator for the quadratic model	137
B.2 Equations of motion for quartic model	138
C Appendix for Quadratic Holstein Model	142
C.1 Details for the even-sector	142
C.1.1 Coupling matrices	142
C.1.2 Manipulation of the EOMs	143
C.2 Details for the odd-sector	144
C.2.1 Equations of Motion	144
C.2.2 Momentum space Green's functions	146
C.3 Quadratic e-ph coupling with $g_2 > 0$	147
D Appendix for T-CuO	150
D.1 Exact Diagonalization with Lanczos	150

List of Tables

1.1	Relevant parameters for the 3-band Emery model in units of eV.	25
4.1	Some example values of the bipolaron binding energy and effective mass.	89

List of Figures

1.1	Sketch of the origin of the electron-phonon coupling term. Without an electron present, the nuclear potential $U_p(x)$ is given by the blue curve I. When an electron is present, the nuclear potential is instead given by the red curve II.	6
1.2	Sketch of the first two orders of the Dyson series represented by Feynman diagrams. Straight lines represent the free propagator of the charge carrying fermion. Squiggly lines represent the free propagator of the boson (the optical phonon in this case). A complete diagram would include labels at the vertices denoting the energies and momenta (or other relevant quantum numbers) of the particles.	9
1.3	Spectral function of the one-dimensional Holstein model as obtained with MA. The effective coupling $\lambda = -g^2/2dt\Omega$ is a dimensionless measure for the strength of el-ph interaction. The strong coupling regime occurs at around $\lambda \sim 1$	19
1.4	Phase diagram of the high-temperature superconducting cuprates for both electron and hole doping. The undoped compounds are antiferromagnetic insulators which become superconducting upon either hole or electron doping. Here, we focus on the hole-doped side of the phase diagram. Public domain figure from https://en.wikipedia.org/wiki/File:Cuphasediag.png	22

List of Figures

1.5	(a) Structure of a typical high-temperature superconducting cuprate compound, YBCO. Layers of copper and oxygen are contained within a host structure of rare-earth and transition metal elements. Figure used under the GFDL, as obtained from https://commons.wikimedia.org/wiki/File:Ybco002.svg . (b) The most relevant orbitals for cuprate physics are the copper $d_{x^2-y^2}$ orbital (round shapes) and the ligand oxygen p_x and p_y orbitals (lobes), forming a unit cell with three orbitals.	23
1.6	$E(\mathbf{k})$ along several cuts of the Brillouin zone for the three-band model in the variational approximation described in [3, 5] with (a) at most 2 magnons and (b) at most 3 magnons. Circles show exact diagonalization results from [6] for a cluster of 32 copper and 64 oxygen orbitals. Full lines show the results from the variational approximation, neglecting spin fluctuations. The overall agreement is excellent and can be further improved by including local spin fluctuations [5]. . .	27
2.1	(a) Sketch of a 1D chain of polar molecules; (b) The potential of the pair with (II) or without (I) an extra charge carrier (full lines) is approximated by a polynomial (thick dashed lines) .	32
2.2	GS quasiparticle weight (left panel) and GS average phonon number (right panel) vs. ζ , in the quadratic ($n = 2$, lines) and quartic ($n = 4$, symbols) models, for various values of λ and $\Omega = 0.5t$, in one dimension.	40
2.3	(left) Z_{at} , and (right) $N_{\text{ph}}^{(\text{at})}$ vs. ζ , for $g_1 = \sqrt{2}$ and $\Omega = 0.5$ (full lines). Dashed lines show the mean-field estimates, while the dot-dashed lines show the results of fitting $\tilde{g}/\tilde{\Omega}$ to exactly reproduce the other quantity. See text for more details. . . .	42

List of Figures

2.4	Estimate of the bipolaron phase diagram in 1D for $\Omega/t = 0.5$ and for different values of ζ , based on second order perturbation theory in t . In all four panels, the solid lines show the transition from S_0 (on-site) stable bipolarons to S_1 (nearest-neighbor) stable bipolarons, while the dashed lines show the unbinding transition above which bound polarons are unstable. Note that panels (c) and (d) have a significantly rescaled y -axis. See text for more details.	46
3.1	Sketch of the crystal structures discussed in this work: (a) 1D chain, and (b) 2D plane, consisting of light atoms (filled circles) intercalated between heavy atoms (empty circles). In the absence of carriers, the ionic potential of a light atom is a simple harmonic well. In the presence of a carrier, the ionic potential of the light atom hosting it remains an even function of its longitudinal displacement, so the linear e-ph coupling vanishes. In suitable conditions the effective ionic potential becomes a double well (see text for more details). .	51
3.2	(a) Overlap between the undoped ground-states with and without anharmonic corrections, and (b) the average number of phonons per site in the undoped system, due to anharmonic corrections, as a function of θ/Ω	55
3.3	Polaron ground-state properties in the atomic limit, for several values of the g_4 : a) quasiparticle weight, and b) average number of phonons in the phonon cloud. Other parameters are $\Omega = 0.5, t = 0$	64
3.4	Relative error in the ground state energy when computed in the semiclassical approximation (see text for details). The coupling $g_2 < -\Omega/4$ is restricted to values for which there is a double-well potential. Other parameters are like in Fig. 3.3.	66

List of Figures

3.5	(color online) Polaron ground-state properties in one dimension for various values of the quartic coupling term g_4 as a function of the quadratic coupling g_2 : a) quasiparticle weight, and b) average number of phonons in the phonon cloud. Other parameters are $t = 1$, $\Omega = 0.5t$	68
3.6	Polaron ground-state properties in two dimensions for various values of the quartic coupling term g_4 as a function of the quadratic coupling g_2 : a) quasiparticle weight, and b) average number of phonons in the phonon cloud. Other parameters are $t = 1$, $\Omega = 0.5t$	69
3.7	$A(k, \omega)$ in 1D, for $g_4 = 0.05$, $\Omega = 0.5$ and $t = 1$, for various values of g_2	70
3.8	$A(k, \omega)$ in 2D, for $g_4 = 0.05$, $\Omega = 0.5$ and $t = 1$, for various values of g_2	71
3.9	Real-space diagonal spectral function $A_{iii}(\omega)$ at $g_4 = 0.05$ for various values of (negative) g_2 in one dimension and for $\Omega = 0.5$. The y -axis has a logarithmic scale. The vertical bars indicate the position of $E_0^{\text{even}} + \Omega$	72
4.1	Sketch of the crystal structures discussed in this work: (a) 1D chain, and (b) 2D plane, consisting of light atoms (filled circles) intercalated between heavy atoms (empty circles). In the absence of carriers, the ionic potential of a light atom is a simple harmonic well. In the presence of a carrier, the ionic potential of the light atom hosting it remains an even function of its longitudinal displacement, so the linear e-ph coupling vanishes. In suitable conditions the effective ionic potential becomes a double well. (Reproduced from the previous chapter)	80
4.2	(a) Bipolaron ground-state energy, and (b) inverse effective mass for $t = 1$, $\Omega = 0.5$, $g_4 = 0.1$, computed with ED (solid black line) and MA (red dots).	85

List of Figures

4.3	Ground-state properties (total energy and inverse mass) of the S0 bipolaron and two independent polarons for $t = 1, \Omega = 0.5$ and $g_4 = 0.2, 0.1,$ and 0.05 for a), b), and c), respectively. For all panels, $U = 0$	87
4.4	Ground-state properties (total energy and inverse mass) of the S0 bipolaron and two independent polarons for $t = 1, \Omega = 2$ and $g_4 = 0.2, 0.1,$ and 0.05 for a), b), and c), respectively. For all panels, $U = 0$	88
4.5	Binding energy Δ and effective-mass ratio $m_{bp}/2m_p$ of the bipolarons for $\Omega = 0.5$ and $\Omega = 2$ at different values of g_4	88
4.6	Ionic potential (above) and ionic ground-state wavefunction (below) in the single-well and double-well models. Solid lines correspond to the situation without an additional carrier, dashed lines to the situation with an additional carrier.	90
4.7	Bipolaron energy (left) and effective mass (right) as a function of the Hubbard U , for $t = 1, \Omega = 0.4$ and $g_4 = 0.1$. Similar results are found for other parameters if U is not large enough to lead to bipolaron dissociation.	92
5.1	Structure of a layer of (a) T-CuO, and (b) CuO ₂ . Full circles are Cu, empty squares are O. The Cu $3d_{x^2-y^2}$ orbitals are drawn at a few sites, with white/dark lobes showing our choice for positive/negative signs. The corresponding ligand O $2p$ orbitals are also indicated on neighboring O sites. The T-CuO layer can be thought of as two intercalated CuO ₂ layers sharing common O. The coppers of the two sublattices hybridize with different O $2p$ orbitals. Panels (c) and (d) show the two degenerate ground-states of the undoped T-CuO layer. Different colors are used for the Cu spins on the two sublattices for better visibility.	98

List of Figures

- 5.2 Qp dispersion in units of J_{dd} for (a) $n_m = 1$, (b) $n_m = 2$, and (c) $n_m = 3$ with full/dashed lines for T-CuO/CuO₂. The Brillouin zone for the magnetic order of Fig. 5.1(c) is shown in red in (b). The shaded area is the smaller BZ for CuO₂. The points marked by circles and empty/full squares are equivalent in CuO₂ but not in T-CuO. (d) Hopping between two adjacent ZRSs, and (e) between a ZRS (red) and one with $x - y$ symmetry (blue). See text for more details. 105
- 5.3 (a) Unit cell for CuO₂, with two Cu spins and four ligand O orbitals. We use the location i of the down-spin Cu as the reference point. The white/shaded areas indicate our choice for positive/negative lobes. (b) Magnetic Brillouin zone (shaded region) vs. full Brillouin zone (unshaded). (c) ZRS between a hole occupying the linear combination of ligand orbitals with $x^2 - y^2$ symmetry, and the spin of the central Cu. The Bloch state is obtained from its translations on the corresponding magnetic sublattice. 106
- 5.4 Comparison between the one-magnon numerical dispersion and the effective calculations involving both the low-energy and first excited state quasiparticles. The results are in qualitative agreement, in particular the shift of the minimum along $k_x = k_y$. The dashed lines are a guide to the eye to demonstrate that the peak along $\Gamma - M$ gets shifted away from $\mathbf{k} = (\pi/2, \pi/2)$ yet remains there along $X - X'$ 111

List of Figures

5.5	The first two panels show the Brillouin zones corresponding to the two possible magnetic orders of Fig. 5.1(c) and (d). The symbols mark the deep minima (full squares), displaced shallower minima (circles) and very shallow minima (empty squares). The two figures are related by a C_4 rotation. The third panel shows the average of these two patterns, where at each special point the deepest local minimum was selected. This pattern has a restored C_4 symmetry and a Brillouin zone (blue line) corresponding to one Cu site/unit cell. The pattern of deep/shallower minima is like that found experimentally.	112
5.6	Quasiparticle dispersion for the two orientations of the magnetic background, along the contour considered in Ref. [20]. Top panel shows the results in the hole picture used throughout this work, whereas the low panel shows the same results in the electron picture relevant for experiments, with further tuning of the parameters. Also, we note that the slight displacements of the shallower minima have not been observed experimentally. This may be because of the very broad widths of the quasiparticle peaks and the loss of spectral weight on one side of these points, which may mask them. In “untwinned” samples the scattering rate should be lower, which may make the observation of these displacements towards Γ more easily visible. Of course, in that case the lack of C_4 symmetry and existence of really shallow minima should also become visible.	115
C.1	a) Quasiparticle weight Z , and (b) average number of phonons for a quadratic model with $g_2 > 0, g_4 = 0$ in the atomic limit $t = 0$, for $\Omega = 1$	148

List of Figures

C.2 Sketch of the lattice potential for i) Holstein, and ii) $g_2 > 0$ quadratic models. Full (dashed) lines indicate ionic potential and ground state wavefunction without (with) an extra charge on the site. 148

List of Symbols

H, \mathcal{H}	Generic Hamiltonian
MA	Momentum average, Momentum average approximation
el-ph	electron-phonon
qp	quasiparticle
t	A charge carrier's hopping amplitude
c_i^\dagger, c_i	Real-space fermionic creation/annihilation operators
$b_{\mathbf{k}}^\dagger, b_{\mathbf{k}}$	Momentum-space bosonic creation/annihilation operators
g	Electron-phonon coupling constant
g_n	n -th order electron-phonon coupling constants
Ω	Phonon frequency
$G(\dots)$	Generic symbol for Green's functions
$A(\dots)$	Generic symbol for spectral functions
ARPES	Angular resolved photoemission spectroscopy
Z	Quasi-particle weight
m^*	Effective mass
$\Sigma(\dots)$	Generic symbol for self-energy
$F_n(\mathbf{k}, i, \omega)$	Generalized Green's functions
ζ	Non-linearity parameter in non-linear Holstein model
EOM	Equation of motion
\bar{g}_0	Momentum-averaged approximate version of the free propagator
$\mathbf{W}_{\mathbf{n}}$	Vectors containing several generalized Green's functions
$\alpha_{\mathbf{n}}, \beta_{\mathbf{n}}, \gamma_{\mathbf{n}}$	Matrices in the EOM for the $\mathbf{W}_{\mathbf{n}}$
λ	Dimensionless coupling-constant of the linear Holstein model, $E_0(t = 0)/E_0(g = 0)$

List of Symbols

Ω_{at}	Effective phonon frequency $\sqrt{\Omega(\Omega + 4g_2)}$
U	On-site Coulomb repulsion
Θ	Energy-scale of free-phonon anharmonic terms
ED	Exact diagonalization
Δ	Binding energy of a bipolaron (Chapter 4) OR Charge-transfer energy
AFM	Antiferromagnetic
FM	Ferromagnetic
ZRS	Zhang-Rice singlet
T-CuO	Tetragonal copper oxide CuO
C_n	n-fold rotational symmetry
BZ	Brillouin zone
p^\dagger, p	Creation/annihilation operator for holes on oxygen p -orbitals
Γ	The $(0, 0)$ point in the Brillouin zone
M	The (π, π) point in the Brillouin zone
X, X'	The $(0, \pi)$ and $(\pi, 0)$ points in the Brillouin zone

Acknowledgements

I want to thank my supervisor, Dr. Mona Berciu, for guiding me through the process of my PhD. From my very first inquiry about open PhD positions to the final drafts of my thesis, she has been extremely helpful at every step of my academic path. I enjoyed working with her. Always available yet never micro-managing, she provided the perfect environment for me to grow as a researcher. I appreciate her focus on actual results as opposed to proxy measures such as time spent at the desk. That way I could explore the beauty of Vancouver and its surrounding mountains while still finishing my PhD at a good pace and with publications in major journals for each of my projects.

I also thank the supervisory committee, Dr. Sarah Burke, Dr. Moshe Rozali and Dr. George Sawatzky for their constructive feedback regarding my thesis.

An important part of my experience at UBC was the Varsity Outdoor Club and the many friendships forged in the snow or on the rock. They are too numerous to list them all here, but I have to especially mention Jens Vent-Schmidt, Ruanne Lai and Caroline Jung for their support in difficult times and for good times in the mountains.

I also thank my parents for their support and understanding along the way.

Finally, I want to thank Kasia Celler for her love and support and her patience and understanding during the final months of thesis preparation.

Chapter 1

Introduction

Solid states physics is concerned with the physics of many, many particles – on the order of 10^{23} – interacting with each other. From a purely theoretical point of view, this problem is merely one of applied math: The equation governing most of the phenomena occurring in materials is the non-relativistic Schrödinger equation,

$$H |\Psi\rangle = E |\Psi\rangle \quad (1.1)$$

for the Hamiltonian of electrons and nuclei,

$$H = - \sum_{\alpha=1}^{N_n} \frac{\mathbf{P}_\alpha^2}{2M_\alpha} - \sum_{j=1}^{N_e} \frac{\mathbf{p}_j^2}{2m} - \sum_{j=1}^{N_e} \sum_{\alpha=1}^{N_n} \frac{Z_\alpha e^2}{|\mathbf{r}_j - \mathbf{R}_\alpha|} + \sum_{j < k}^{N_e} \frac{e^2}{|\mathbf{r}_j - \mathbf{r}_k|} + \sum_{\alpha < \beta}^{N_n} \frac{Z_\alpha Z_\beta e^2}{|\mathbf{R}_\alpha - \mathbf{R}_\beta|}, \quad (1.2)$$

where N_e , \mathbf{p}_j and \mathbf{r}_j denote number, momentum and position of the electrons, while N_n , \mathbf{P}_α and \mathbf{R}_α are the number, momentum and position of the nuclei, whose atomic numbers are the Z_α and masses are M_α . The recipe, then, seems clear enough: Find the eigenvalues and eigenfunctions of the Hamiltonian (1.2) and then use them to obtain values for all desired observables of the system. So, in principle, we have a *theory of everything* for solid state systems.

There are two problems with this view. First, the vast number of particles involved makes the effort to solve the equation prohibitively expensive. In fact, there are not enough atoms in the universe to even store the wavefunction of an atom of Iron on a crude $10 \times 10 \times 10$ grid¹. Second, even

¹The wavefunction has a positional argument for each of the iron's 26 electrons, so we would need to store $1000^{26} = 10^{78}$. Assuming 16 bit precision and the ability to store one bit per atom, we would then need 10^{79} atoms, which is close to the estimated number of atoms in the observable universe.

if we were able to calculate and store the wavefunction, it would not provide a satisfactory answer, because it has no explanatory power. When we look to *explain* a phenomenon, we want to be able to find generalized rules from which we can predict the specific behaviour of a system but also make extrapolations about the expected behaviour of similar systems. The wavefunction, on the other hand, contains too much information to be useful in this way. For example, possessing all the eigenfunctions of the superconductor YBCO would indeed confirm that it was superconducting, but it still would not explain *why*. That insight would be hidden in the vast amount of information contained within the wavefunction.

1.1 Model Hamiltonians

The solid state community attempts to address the aforementioned problems through the use of *approximations* and *models*. These approaches can be broadly classified as *ab-initio methods* and *model Hamiltonians*. An ab-initio approach applies approximations to the initial Schrödinger equation to allow for its numerical solution without relying on any extra parameters; the input is merely the number of particles and type of nuclei. The most prominent example of an ab-initio method is Density Functional Theory (DFT) [7, 8]. It maps the interacting many-body problem to an effective non-interacting problem and has found considerable success in describing the ground state of weakly correlated system. With some caution, it can be used to compute the band structure of a material.

A model Hamiltonian approach, in contrast, attempts to find a simplified Hamiltonian which captures the essential physics of the system. The model Hamiltonian will be considerably easier to solve than the full Hamiltonian, at the cost of introducing adjustable parameters. They can sometimes be determined by fitting the model's predictions to experimental observations, or calculated using ab-initio methods. The great advantage of describing systems with simplified model Hamiltonians is that they allow us to study the importance of certain effects in isolation. As a consequence, model Hamiltonians have great explanatory power.

There are, however, certain caveats to keep in mind when working with model Hamiltonians:

- The particular choice of model Hamiltonian has to be motivated and informed based on external input such as experiments or ab-initio calculations.
- Balance has to be found between finding the simplest possible Hamiltonian and retaining enough of the physics relevant for the phenomenon to be studied.
- Special attention has to be paid to the origin and initial assumptions that went into the derivation or motivation of a particular model Hamiltonian to make sure it is not used in situations where they do not actually apply.

In this thesis, we will investigate a few model Hamiltonians that are used as the *standard models* for certain systems. In particular, we will study the effects of seemingly minor extensions to these models. Throughout, we will discover that even small modifications can often vastly alter the physics of the system and thereby invalidate generalized assumptions about them. The remainder of this chapter is devoted to introducing the standard models and their extensions that we are going to study.

1.2 The Holstein model for electron-phonon coupling

A universally applied approximation to the general Hamiltonian (1.2) is to decouple the movement of the electrons from that of the much heavier nuclei. This Born-Oppenheimer approximation [9] assumes that the nuclear coordinates are fixed parameters. The solution of the remaining electronic problem provides a ground-state energy $\mathcal{E}_0^{\text{el}}(\{\mathbf{R}_\alpha\})$ that is parameterized by these nuclear coordinates and thus provides an effective potential for the nuclei, the so-called Born-Oppenheimer surface. This surface determines the lattice structure and its dynamics. A common approximation expands the

1.2. The Holstein model for electron-phonon coupling

BO-surface to second order in the nuclear coordinates around the surfaces' minimum. The resulting Hamiltonian represents a collection of simple harmonic oscillators and the eigenmodes are the quanta of lattice vibrations, the so-called phonons.

These phonons interact with the electrons, since they influence the nuclear positions within (1.2). Detailed derivations are found in most advanced textbooks[10]; here we are concerned with a popular model Hamiltonian, the so-called Holstein model [11]. Its form is

$$\mathcal{H} = \mathcal{H}_{\text{el}} + \mathcal{H}_{\text{ph}} + \mathcal{H}_{\text{el-ph}}, \quad (1.3)$$

with the following components.

- \mathcal{H}_{el} describes electrons in a *tight-binding* model. It is of the form

$$\mathcal{H}_{\text{el}} = - \sum_{i,j} t_{ij} c_i^\dagger c_j$$

where i and j are generalized indices for single-particle orbitals, and t_{ij} is the hopping matrix-element between them.

- \mathcal{H}_{ph} describes the free phonon dispersion. In the Holstein model and most other standard electron-phonon models, the lattice potential is treated within the harmonic approximation. The resulting Hamiltonian has the form

$$\mathcal{H}_{\text{ph}} = \sum_{\mathbf{k}} \omega_{\mathbf{k}} b_{\mathbf{k}}^\dagger b_{\mathbf{k}}$$

where $b_{\mathbf{k}}^\dagger$ creates a phonon of momentum \mathbf{k} , which has energy $\omega_{\mathbf{k}}$. This form already contains several simplifying assumptions.

First, the mode is assumed to be *optical* (finite energy at $\mathbf{k} = 0$) instead of *acoustical* (energy proportional to $|\mathbf{k}|$ for small momenta). This is not so much an approximation as it is a modeling choice. Optical phonons are those associated with out-of-phase movement of the atoms. This is relevant, for example, for the longitudinal vibration of a diatomic molecule, or for the coupling of an ionic crystal – with

1.2. The Holstein model for electron-phonon coupling

alternating positive and negative ions – to a charge carrier. Such coupling is usually stronger than to acoustic phonons, where atoms move in-phase and their relative distances are unchanged. Second, only a single phonon mode is considered whereas real molecules and crystals typically have a multitude of vibrational modes. However, often there is one characteristic mode that has a low energy whereas other modes have very high energies and are, at low temperatures at least, frozen out. Additionally, often one mode couples more strongly to the charge carriers for symmetry reasons.

- Finally, \mathcal{H}_{ph} describes how the electrons interact with the phonons. In the Holstein model, it is given by

$$\mathcal{H}_{\text{el-ph}} = g \sum_i c_i^\dagger c_i (b_i^\dagger + b_i).$$

where g is the coupling strength. We will now discuss the motivation behind this form.

Within the tight-binding model, where electrons are confined to a discrete set of localized orbitals, a motivation of the Holstein electron-phonon coupling term can be performed as follows. We give the explanation for a one-dimensional potential and one electron orbital per site, but note that it is easily extended to the more general case.

The argument is sketched in Fig. 1.1. Consider a single lattice site i and let the potential for a single lattice coordinate be given by $U_p(x)$, (p standing for *phonon*). Recall that within the Born-Oppenheimer approximation, this potential is determined by the electronic state. If there is no electron present on site i , the lattice potential will have a particular form, such as the one shown as the blue curve I in the figure. If, on the other hand, an electron is present, the lattice potential will assume another form, such as the one shown as the red curve II. Now, the blue (no-electron) curve provides us with the free part, \mathcal{H}_{ph} whereas the *difference* of the red and blue curves provides us with the electron-phonon interaction part.

The specific form of the Holstein el-ph interaction term is obtained

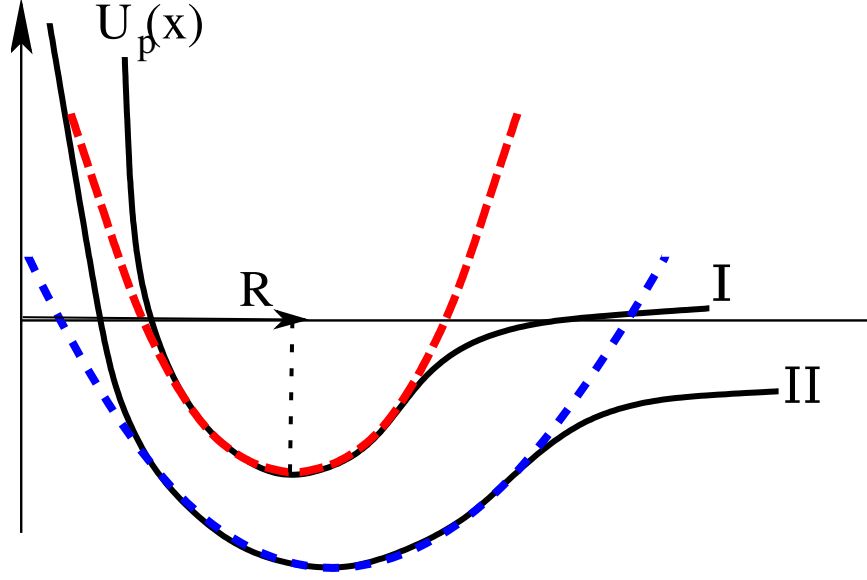


Figure 1.1: Sketch of the origin of the electron-phonon coupling term. Without an electron present, the nuclear potential $U_p(x)$ is given by the blue curve I. When an electron is present, the nuclear potential is instead given by the red curve II.

from this general argument as follows. First, the lattice potentials I and II are replaced by their harmonic approximations, which have some form $\sim \omega^2(x - x_0)^2$ with phonon frequency ω and equilibrium position x_0 . Next, it is assumed that the presence of an electron only changes the lattice's equilibrium position, but not its frequency. With this assumption, the quadratic terms of both curves I and II have the same coefficient. Therefore, their difference will be a *linear* function.

Properties of the linear Holstein model

Before we discuss our extension to the Holstein model, we will first study it in its simplest form,

$$\mathcal{H} = -t \sum_{\langle i,j \rangle} c_i^\dagger c_j + \Omega \sum_i b_i^\dagger b_i + g \sum_i c_i^\dagger c_i (b_i^\dagger + b_i). \quad (1.4)$$

1.2. The Holstein model for electron-phonon coupling

In this model, we have nearest-neighbor hopping t and dispersionless phonons with frequency Ω (sometimes called Einstein phonons). As theorists, we set $\hbar = 1$, so we will be using the terms frequency and energy interchangeably. Within this thesis, we will refer to the model (1.4) as the *linear* Holstein model.

We will now describe the *momentum average approximation* (MA) and how it can be used to provide accurate analytical results for the single-particle properties of the Holstein model. MA was introduced in [1, 12] and refined in subsequent work such as [13, 14]. For an in-depth look into MA, we refer the reader to these works and references therein. We will, however, provide an introduction to MA here in a formulation that is slightly more accessible than the initial derivation. It goes as follows.

We are interested in computing the single-particle Green's function for (1.4), which is defined as

$$G(\mathbf{k}, \omega) = \langle 0 | c_{\mathbf{k}} [\omega - \mathcal{H} + i\eta]^{-1} c_{\mathbf{k}}^\dagger | 0 \rangle \quad (1.5)$$

for momentum \mathbf{k} and energy ω where $\eta > 0$ is a small convergence factor. Good introductions to Green's functions are found in most advanced solid-state physics textbooks such as [15]. We note here that we are interested in the interaction of a single carrier with the phonons; therefore, the vacuum state $|0\rangle$ is understood to contain no other carriers, i.e., $c_i |0\rangle = 0$. We introduce the spectral function

$$A(\mathbf{k}, \omega) = -\frac{1}{\pi} \text{Im} G(\mathbf{k}, \omega) \quad (1.6)$$

which is directly related to a quantity accessible to experimentalists via Angular Resolved Photoemission Spectroscopy (ARPES)² By inserting a full set of eigenstates $|\psi_n\rangle$ of \mathcal{H} into (1.5), it is a textbook derivation to

²For an in-depth discussion of ARPES, see the excellent review in [16]. For a derivation of the ARPES intensity expressed through the spectral function, see the PhD Thesis of Dr. Ebrahimnejad [17].

1.2. The Holstein model for electron-phonon coupling

show that

$$A(\mathbf{k}, \omega) = \sum_n \left| \langle \psi_n | c_{\mathbf{k}}^\dagger | 0 \rangle \right|^2 \delta(\omega - E_n(\mathbf{k})). \quad (1.7)$$

That is, the spectral function is a set of peaks³ located at the Hamiltonian's eigenenergies, with their weights given by the overlap of the corresponding eigenstate with that of a free particle. In particular, the lowest-lying (in energy) peak tells us where the groundstate of the system is, and its weight is called the *quasi-particle weight* Z . This quantity can range from 0 to 1 and indicates how similar to a free particle's state the ground state is. In a system where a carrier interacts with bosonic degrees of freedom, we expect the free carrier to become *dressed* with a cloud of bosons and thus acquire a larger effective mass, expressed through a reduced qp weight Z .

Let us at this point introduce another quantity that is often mentioned in solid state physics, the self-energy. We begin by noting that for a free particle with dispersion $E_0(\mathbf{k})$ the momentum-space Green's function – also called the free propagator – is given by

$$G_0(\omega, \mathbf{k}) = \frac{1}{\omega - E_0(\mathbf{k}) + i\eta}$$

for small convergence factor $\eta > 0$. For an interacting particle, the Green's function will be modified. Via simple algebra, one can, however, always write it as

$$G(\omega, \mathbf{k}) = \frac{1}{\omega - E_0(\mathbf{k}) - \Sigma(\omega, \mathbf{k}) + i\eta}$$

for some complex-valued function Σ , the *self-energy*. The real part of Σ renormalizes the energy of the quasi-particle whereas the imaginary part changes its lifetime.

An advantage of working with the Green's function G instead of the Hamiltonian \mathcal{H} is that the Green's function has a *diagrammatic expansion* that allows us to separate out the "easy", free part from of the Hamiltonian

³The δ -peaks are, in fact, Lorentzians with width given by η

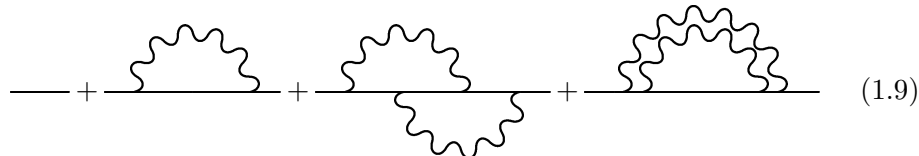


Figure 1.2: Sketch of the first two orders of the Dyson series represented by Feynman diagrams. Straight lines represent the free propagator of the charge carrying fermion. Squiggly lines represent the free propagator of the boson (the optical phonon in this case). A complete diagram would include labels at the vertices denoting the energies and momenta (or other relevant quantum numbers) of the particles.

from the "hard", interacting part. If we write this separation as

$$\mathcal{H} = \mathcal{H}_0 + \mathcal{H}_1$$

and introduce the operator version of the Green's function as $\hat{G}(\omega) = [\omega - \mathcal{H} + i\eta]^{-1}$, then simple algebra shows that

$$\hat{G}(\omega) = \hat{G}_0(\omega) + \hat{G}(\omega)\mathcal{H}_1\hat{G}_0(\omega) \quad (1.8)$$

which is the so-called *Dyson's identity* and $\hat{G}_0(\omega) = [\omega - \mathcal{H}_0 + i\eta]^{-1}$ is the *free propagator*. The decomposition of \mathcal{H} is ideally chosen such that G_0 is easy to compute.

Dyson's identity prescribes an iterative way to compute the Green's function: By reinserting the identity into itself, an infinite series is obtained where each term is of the form $\hat{G}_0[\mathcal{H}_1\hat{G}_0]^n$. When going to a particular basis, such as momentum space, these terms can be represented as Feynman diagrams, with vertices representing the interaction \mathcal{H}_1 and edges representing the free propagator $\hat{G}_0(\omega)$.

A good introduction to the use of Feynman diagrams in many-body physics is found in [18]. We show a sketch of them in Fig. 1.2. It represents the first few iterations of Dyson's identity in a simplified form. In a complete representation, the various propagating lines would be labeled with the energies and momenta (or other relevant quantum numbers of the particles).

1.2. The Holstein model for electron-phonon coupling

The first term in Fig. 1.2 describes a carrier propagating freely. The second term describes the creation and subsequent absorption of a phonon. The final two terms describe the creation and absorption of two phonons, one term where the phonons get destroyed in the order they were created and one term where they get destroyed in the inverse order. For completeness, we note that if we had defined our vacuum $|0\rangle$ as a state with a number of charge carriers below the Fermi level instead of a state with no carriers at all, the diagrammatic expansion would also include diagrams where the carrier creates a phonon and that phonon then creates a carrier-hole pair by exciting a carrier from below the Fermi level into a state above it. Since we are only concerned with the physics of a single carrier interacting with a cloud of bosons, the vacuum is defined to contain no extra carriers and thus these terms do not arise.

While these diagrams are an excellent tool for visualizing many-body interaction processes, the sum over the infinite number of diagrams cannot be carried out except in the most basic cases. Instead, several different approaches exist:

- If the interactions in \mathcal{H}_1 are sufficiently weak, the diagrammatic expansion can be terminated after a reasonably low number of iterations. This works very well in other fields such as quantum electrodynamics, but usually fails in many-body physics due to the stronger interactions. In our specific case, it works if $g \leq \Omega$ and provides the weak-coupling limit perturbation expansion of the Holstein model.
- More common in solid state physics are approaches that sum an infinite subset of diagrams. These diagrams are chosen in such a way that the infinite sum can be carried out analytically. An example relevant for the Holstein model is the Self-Consistent Born Approximation (SCBA) [19] where only those diagrams are included where phonon lines do not overlap (such as the last term shown in Fig. 1.2). While these approaches are very popular, a common problem is that they are not controlled because they lack a "small parameter" and the diagrams that are omitted may have contributions comparable to the ones that

1.2. The Holstein model for electron-phonon coupling

are included.

In short, the first approach sums all diagrams up to a certain order in the interaction \mathcal{H}_1 whereas the second approach sums diagrams of all orders, but only a subset of them. In both approaches, the diagrams that do get included are included with their exact contributions. The momentum average approximation provides a unique third approach: It sums *all* diagrams of *all* orders, but it individually approximates each diagram with a simplified expression in a way that allows us to analytically carry out the summation.

Let us demonstrate this now. Dyson's equation for the Holstein model yields

$$\begin{aligned} G(\mathbf{k}, \omega) &= \langle 0 | c_{\mathbf{k}} \hat{G}(\omega) c_{\mathbf{k}}^\dagger | 0 \rangle \\ &= \langle 0 | c_{\mathbf{k}} \left(\hat{G}_0(\omega) + \hat{G}(\omega) \mathcal{H}_1 \hat{G}_0(\omega) \right) c_{\mathbf{k}}^\dagger | 0 \rangle. \end{aligned}$$

In the following, we will omit the hats and the argument ω whenever this can be done unambiguously.

The first part of the expansion of G yields just the non-interacting Green's function. Since the vacuum has no phonons and $c_{\mathbf{k}}^\dagger$ only adds a fermion, this gives just $1/(\omega - \varepsilon_{\mathbf{k}} + i\eta)$ for $\eta \rightarrow 0^+$, where $\varepsilon_{\mathbf{k}}$ is the free carrier dispersion. It depends of course on the particular form \mathcal{H}_{el} . For d -dimensional nearest-neighbor hopping in a cubic lattice, the dispersion is $-2t \sum_{i \in \{x, y, z\}} \cos(k_i a)$ where k is the momentum and a the lattice constant. For the second part, we insert $1 = \sum_{\mathbf{k}} |\mathbf{k}\rangle \langle \mathbf{k}|$ and use the fact that G_0 is diagonal in \mathbf{k} . This finally yields

$$G(\mathbf{k}, \omega) = \frac{1}{\omega - \varepsilon_{\mathbf{k}} + i\eta} \cdot \left[1 + \langle 0 | c_{\mathbf{k}} G \mathcal{H}_1 c_{\mathbf{k}}^\dagger | 0 \rangle \right]. \quad (1.10)$$

To study how \mathcal{H}_1 acts on $c_{\mathbf{k}}^\dagger | 0 \rangle$, we transform the momentum to real space via

$$c_{\mathbf{k}}^\dagger = \frac{1}{\sqrt{N}} \sum_i e^{i\mathbf{k} \cdot \mathbf{r}_i} c_i^\dagger$$

1.2. The Holstein model for electron-phonon coupling

and obtain

$$G(\mathbf{k}, \omega) = \frac{1}{\omega - \varepsilon_{\mathbf{k}} + i\eta} \cdot \left[1 + \frac{1}{\sqrt{N}} \sum_i e^{i\mathbf{k}\cdot\mathbf{r}_i} \langle 0 | c_{\mathbf{k}} G \mathcal{H}_1 c_i^\dagger | 0 \rangle \right].$$

Let us focus on just the evaluation of the bracket. \mathcal{H}_1 contains a sum over sites j ; because of the term n_j , its contribution is zero except for the site i where we have created an electron. Since we have no bosons in the system, only the term with b_i^\dagger gives a contribution. The resulting state then is

$$\mathcal{H}_1 c_i^\dagger | 0 \rangle = g c_i^\dagger b_i^\dagger | 0 \rangle.$$

The resulting matrix element with the Green's function gets its own name:

$$F_1(\mathbf{k}, i, \omega) := \langle 0 | c_{\mathbf{k}} \hat{G}(\omega) c_i^\dagger b_i^\dagger | 0 \rangle \quad (1.11)$$

where the subscript 1 denotes that there is *one* phonon in the system.

We use the Dyson equation a second time to derive an equation of motion (EOM) for F_1 .

$$\begin{aligned} F_1(\mathbf{k}, i, \omega) &= \langle 0 | c_{\mathbf{k}} \hat{G}(\omega) c_i^\dagger b_i^\dagger | 0 \rangle \\ &= \langle 0 | c_{\mathbf{k}} \hat{G}(\omega) \hat{\mathcal{H}}_1 \hat{G}_0(\omega) c_i^\dagger b_i^\dagger | 0 \rangle. \end{aligned}$$

Note that we dropped the single term $\hat{G}_0(\omega)$ from the Dyson expansion. This is valid because F_1 is a matrix element between states with differing number of phonons (1 and 0); since G_0 conserves the phonon number, this matrix element is 0. As an intermediate result, we obtain

$$F_1(\mathbf{k}, i, \omega) = \sum_j G_0(j - i, \omega - \Omega) \cdot \langle 0 | c_{\mathbf{k}} \hat{G}(\omega) \hat{\mathcal{H}}_1 c_j^\dagger b_i^\dagger | 0 \rangle.$$

where we have switched the basis representation of G_0 from momentum space to position space,

$$G_0(j - i, \omega) = \langle 0 | c_j \hat{G}_0(\omega) c_i^\dagger | 0 \rangle.$$

1.2. The Holstein model for electron-phonon coupling

Now we have to study the action of \mathcal{H}_1 . This time, both the bosonic annihilation and creation part have a contribution. Let us treat the destruction part first. Although cumbersome to write down, it should be clear what happens: We can only destroy a phonon on sites where there is one, and only if there is also an electron on that site. This introduces a term δ_{ij} , so we obtain $\langle 0 | c_{\mathbf{k}} \hat{G}(\omega) c_i^\dagger | 0 \rangle = G(\mathbf{k}, i, \omega)$, where $G(\mathbf{k}, i, \omega)$ is just the Green's function in *mixed basis* representation: We add a particle on site i and remove it with momentum \mathbf{k} . The creation part will create another boson at the site the electron is at.

Up to this point, the derivation has been exact. Now we introduce the crucial approximation: Bosons will be allowed only at a single site i . To get bosons at another site, one has to first get rid of all the bosons at site i . This approximation leads to a form for the creation part that is similar to the form for the destruction part, i.e. $\langle 0 | c_{\mathbf{k}} \hat{G}(\omega) c_i^\dagger (b_i^\dagger)^2 | 0 \rangle =: F_2(\mathbf{k}, i, \omega)$. Putting everything together gives us

$$F_1 = gG_0(0, \omega - \Omega) \cdot [G(\mathbf{k}, i, \omega) + F_2(\mathbf{k}, i, \omega)]$$

where G_0 is given in real space. This is the Fourier transform of $G_0(\mathbf{k}, \omega - \Omega)$, and the dc-value is just the *integral* over the transformed function, i.e.

$$G_0(0, \omega - \Omega) = \frac{1}{N} \sum_{\mathbf{k}} G_0(\mathbf{k}, \omega - \Omega) =: \bar{g}_0(\omega - \Omega).$$

In other words, the exact form of the free propagator is replaced by its *momentum-averaged* form, giving the method its name. The variational interpretation of this approximation is that the full Hilbert space is replaced by a restricted Hilbert space containing only states of the nature

$$|i, j, n\rangle = c_i^\dagger (b_j^\dagger)^n |0\rangle.$$

This restriction can be systematically relaxed by allowing states with 1 cloud and one extra phonon, which gives rise to the first systematic improvement of MA, called MA(1). In turn, the basic form of MA is called MA(0). Any

1.2. The Holstein model for electron-phonon coupling

number of improved versions MA(n) can be formulated, where n gives the number of additional phonons allowed outside the “main” cloud⁴. Obviously in the limit $n \rightarrow \infty$ the full Hilbert space is recovered and the approximation converges to the exact result. However, it turns out that for the Holstein model, adequate accuracy for quasi-particle properties is obtained already for MA(0). For now, we return to the evaluation of the equations of motion.

We see that the equation of motion for F_1 contains $G(= F_0)$ and F_2 . We can see that an equation of motion for F_2 would contain F_1 and F_3 , since each additional application of \mathcal{H}_1 will either remove or add a phonon. Thus, let us now derive the general expression for F_n . It is

$$\begin{aligned} F_n(\mathbf{k}, i, \omega) &= \langle 0 | c_{\mathbf{k}} \hat{G}(\omega) c_i^\dagger (b_i^\dagger)^n | 0 \rangle \\ &= \langle 0 | c_{\mathbf{k}} \hat{G}(\omega) \mathcal{H}_1 \hat{G}_0(\omega) c_i^\dagger (b_i^\dagger)^n | 0 \rangle \\ &= \sum_j G_0(j - i, \omega - n\Omega) \langle 0 | \hat{G}(\omega) \mathcal{H}_1 c_j^\dagger (b_i^\dagger)^n | 0 \rangle \end{aligned}$$

The destruction part of \mathcal{H}_1 will give us again a δ_{ij} . Next, note that $[b_i, f(b_i^\dagger)] = \partial/\partial b_i^\dagger f(b_i^\dagger)$ for any function f . Hence $[b_i, (b_i^\dagger)^n] = n(b_i^\dagger)^{n-1}$. For the creation part, we make again use of the approximation that additional bosons can be added only to sites where bosons are already present. It is then straightforward to arrive at the recursion relation for F_n ,

$$\begin{aligned} F_0(\mathbf{k}, i, \omega) &= \langle 0 | c_{\mathbf{k}} \hat{G}(\omega) c_i^\dagger | 0 \rangle \\ F_n(\mathbf{k}, i, \omega) &= g\bar{g}_0(\omega - n\Omega) \cdot [n \cdot F_{n-1}(\mathbf{k}, i, \omega) + F_{n+1}(\mathbf{k}, i, \omega)]. \end{aligned} \quad (1.12)$$

By introducing a cut-off in n , we can find an explicit solution for these relations. The index n denotes the number of phonons we add to the system. The quantity $F_n(\mathbf{k}, i, \omega)$ then is the amplitude for putting n phonons and

⁴We remark that MA(n) as formulated in, e.g., [13] are not exactly equivalent to variational models with states $c_i^\dagger b_{a_1}^\dagger \dots b_{a_n}^\dagger (b_j^\dagger)^m$; instead, they are defined by how many orders in the Dyson expansion retain the full form of the free propagator: MA(0) keeps the free propagator only in the 0-th order and replaces it with its momentum averaged version beginning at the first order, whereas MA(1) would treat the free propagators in both the 0-th order and the 1st order exactly and only replace it with the momentum averaged version beginning at the second order.

1.2. The Holstein model for electron-phonon coupling

one electron at site i into the system and later having a state where the electron has momentum \mathbf{k} and there are no phonons left in the system. We can therefore expect that $F_n \rightarrow 0$ for $n \rightarrow \infty$. For a cut-off N , we set $F_n = 0$ for all $n > N$. How to determine a good value for the cut-off will be discussed later. Let us for now just see how we can solve the recursion relations for F_n . With the cut-off, we have

$$F_N(\mathbf{k}, i, \omega) = g\bar{g}_0(\omega - N\Omega) \cdot N \cdot F_{N-1}(\mathbf{k}, i, \omega)$$

since $F_{N+1} = 0$. This means that $F_N(\mathbf{k}, i, \omega)$ is proportional to $F_{N-1}(\mathbf{k}, i, \omega)$ and we introduce $A_N = g\bar{g}_0(\omega - N\Omega) \cdot N$ to write

$$F_N(\mathbf{k}, i, \omega) = A_N \cdot F_{N-1}(\mathbf{k}, i, \omega).$$

With F_N now being given in terms of F_{N-1} only, we can continue. Let us omit the arguments (\mathbf{k}, i, ω) from the F_n as they do not change anyway. Let us also introduce the shorthand $\bar{g}_0(N)$ for $\bar{g}_0(\omega - N\Omega)$.

$$\begin{aligned} F_{N-1} &= g\bar{g}_0(N-1) \cdot [(N-1)F_{N-2} + F_N] \\ &= g\bar{g}_0(N-1) \cdot [(N-1)F_{N-2} + A_N F_{N-1}]. \end{aligned}$$

This equation contains only F_{N-1} and F_{N-2} . It can be rearranged to give $F_{N-1} = A_{N-1}F_{N-2}$. We see that this continues all the way down to F_1 , which then will be given as $F_1 = A_1G$. Let us derive a general expression for the A_n . For A_N , we have the explicit expression from above. The other A_n are defined via

$$\begin{aligned} F_n &= g \cdot \bar{g}_0(n) \cdot [nF_{n-1} + F_{n+1}] \\ &= g \cdot \bar{g}_0(n) \cdot [nF_{n-1} + A_{n+1}F_n] \end{aligned}$$

1.2. The Holstein model for electron-phonon coupling

This can be rearranged to

$$\begin{aligned} (1 - g\bar{g}_0(n)A_{n+1}) \cdot F_n &= g\bar{g}_0(n)nF_{n-1} \\ \Leftrightarrow F_n &= \frac{n \cdot g\bar{g}_0(n)}{1 - g\bar{g}_0(n)A_{n+1}} \cdot F_{n-1}. \end{aligned}$$

Thus, by definition,

$$A_n = \frac{n \cdot g\bar{g}_0(n)}{1 - g\bar{g}_0(n)A_{n+1}}. \quad (1.13)$$

We are interested in A_1 , because via $F_1 = A_1G$, we can obtain an explicit expression for G . A_1 is given in terms of a continued fraction.

$$A_1 = \frac{g\bar{g}_0(1)}{1 - g\bar{g}_0(1) \frac{2 \cdot g\bar{g}_0(2)}{1 - g\bar{g}_0(2) \frac{3 \cdot g\bar{g}_0(3)}{1 - \ddots}}}$$

We will come back to the evaluation of this expression in an instant, but first let us see how knowledge of A_1 helps us determining the Green's function.

Inserting what we have derived so far into (1.10) yields

$$\begin{aligned} G(\mathbf{k}, \omega) &= \frac{1}{\omega - \varepsilon_{\mathbf{k}} + i\eta} \cdot \left[1 + \frac{g}{\sqrt{N}} \sum_i e^{i\mathbf{k} \cdot \mathbf{r}_i} A_1 G(\mathbf{k}, i\omega) \right] \\ &= \frac{1}{\omega - \varepsilon_{\mathbf{k}} + i\eta} \cdot [1 + gA_1 G(\mathbf{k}, \omega)] \end{aligned}$$

We can rearrange this to obtain

$$G(k, \omega) = \frac{1}{\omega - \varepsilon_{\mathbf{k}} + i\eta - gA_1(\omega)}. \quad (1.14)$$

A closer look reveals that now we not only have an explicit expression for $G(k, \omega)$ in terms of A_1 , we also see that gA_1 is the *self-energy* of the system. Since A_1 involves only the momentum-averaged expression $g_0(\omega)$, the self-energy is \mathbf{k} -independent.

There are several ways to solve the continued fraction. Let us define A_1^k

1.2. The Holstein model for electron-phonon coupling

as the value for A_1 that is obtained when choosing $N = k$ as the cut-off, i.e., all A_n with $n > N$ are zero. Then one can compute A_1^k for increasing values of k until the change $A_1^{k+1} - A_1^k$ is below a certain threshold. This is the straight-forward approach. The disadvantage is that it involves a lot of computation, and to make the step from k to $k + 1$ one has to repeat the complete computation as the result from the computation of A_1^k cannot be used to arrive at A_1^{k+1} . A better method is the modified Lentz method as described in [20]. The advantage of that method is that we do not have to set a cut-off N in advance. Instead, the n -th convergent can be computed using the $n - 1$ -th convergent. To use this method, we have to write our continued fraction in the canonical form,

$$x = b_0 + \frac{a_1}{b_1 + \frac{a_2}{b_2 + \frac{a_3}{b_3 + \ddots}}}$$

In our case, we have

$$\begin{aligned} b_0 &= 0 & a_1 &= g\bar{g}_0(1) \\ b_n &= 1 & a_n &= -g^2 \cdot n \cdot \bar{g}_0(n-1) \cdot \bar{g}_0(n). \end{aligned}$$

The calculation of the b_n and a_n does not require any recursion, so it is trivial to write a function that returns for a given n the appropriate coefficient a_n or b_n . The modified Lentz method is given in Alg. 1. The value of 10^{-30} can be any small value and is needed to avoid division by zero. The value of ε denotes the desired accuracy of our computation.

Figure 1.3 shows some typical spectral functions of the one-dimensional Holstein model as obtained via MA. It is customary to introduce the dimensionless coupling constant $\lambda = g^2/2dt\Omega$. As we'll show later, this is the ratio of the model's ground state energies in the strong and the weak interaction limits. In the first panel, $\lambda = 0$, we just recover the free electron's dispersion $-2t \cos(ka)$, with lattice constant a set to 1. At weak coupling,

Algorithm 1: Modified Lentz Method

```
begin
   $x := b_0$ 
  if  $b_0 = 0$  then
    |  $x := 10^{-30}$ 
  end
   $C := x$ 
   $D := 0$ 
   $j := 0$ 
   $\Delta := 0$ 
  while  $|\Delta - 1| > \varepsilon$  do
    |  $j := j + 1$ 
    |  $b := b(j, \omega)$ 
    |  $a := a(j, \omega)$ 
    |  $D := b + a \cdot D$ 
    | if  $D = 0$  then
      | |  $D := 10^{-30}$ 
    | end
    |  $C := b + a/C$ 
    | if  $C = 0$  then
      | |  $C := 10^{-30}$ 
    | end
    |  $D := 1/D$ 
    |  $\Delta := C \cdot D$ 
    |  $x = x \cdot \Delta$ 
  end
end
```

1.2. The Holstein model for electron-phonon coupling

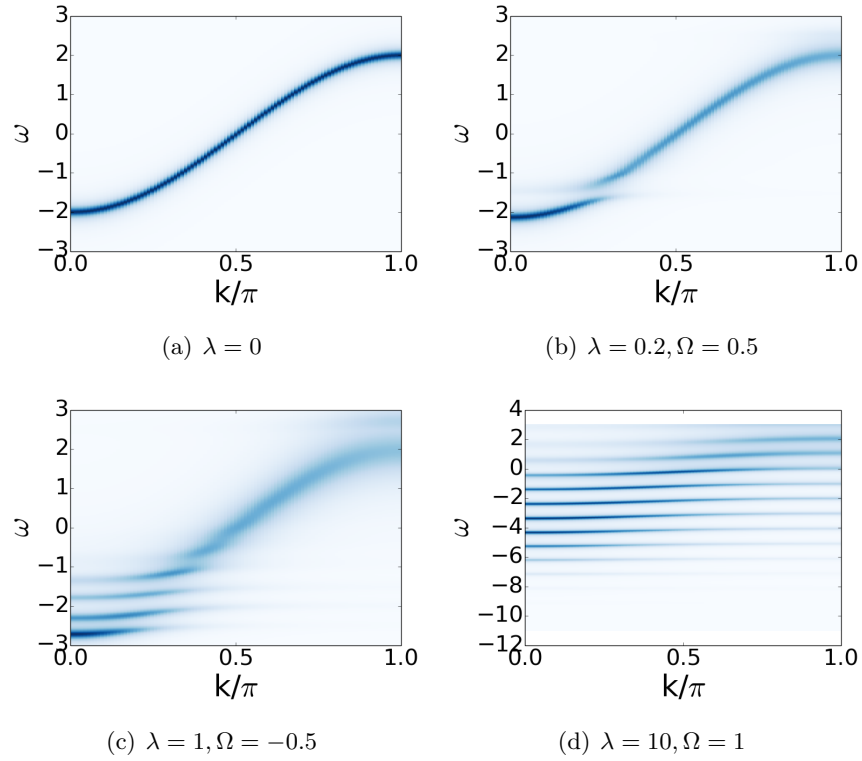


Figure 1.3: Spectral function of the one-dimensional Holstein model as obtained with MA. The effective coupling $\lambda = -g^2/2dt\Omega$ is a dimensionless measure for the strength of el-ph interaction. The strong coupling regime occurs at around $\lambda \sim 1$.

1.2. The Holstein model for electron-phonon coupling

$\lambda = 0.2$, we observe two things: The dispersion of the lowest lying state still has roughly a cosine shape $-2t^* \cos(ka)$ but with $t^* < t$. This is because the carrier becomes *dressed* with phonons, which increases its effective mass. In addition, the spectral function also shows a *continuum* of energies. These are the “polaron+1-phonon” states: For some momentum \mathbf{k} , the system’s state can either be a polaron with energy $E_0(\mathbf{k})$ or it could be a polaron with energy $E_0(\mathbf{k} - \mathbf{q})$ and, far away, a phonon with momentum \mathbf{q} and energy Ω . The energy of this state would be $E_0(\mathbf{k} - \mathbf{q}) + \Omega$. Since \mathbf{q} can be any momentum, at momentum \mathbf{k} the polaron + phonon states span all the energies from $\min(E_0) + \Omega$ to $\max(E_0) + \Omega$. That is, the continuum starts at exactly Ω above the polaronic ground state. Close inspection of the spectral function as obtained from MA, however, shows that the continuum instead originates at $-2t + \Omega$, i.e., precisely Ω above the free-electron ground state. This discrepancy is easiest explained in the variational picture of MA. Recall that $\text{MA}(0)$ is equivalent to restricting the Hilbert space to states where all phonons are located on the same site. Therefore, within this Hilbert space we cannot describe states that have a phonon cloud in one location and a single phonon in another location. Higher orders of MA obtain more accurate estimates of the start of the continuum by allowing states where there are phonons away from the cloud. A more detailed discussion is found elsewhere [13]. The main observation is that $\text{MA}(n)$ predicts the continuum to start an energy Ω above the polaronic ground state of $\text{MA}(n-1)$. Further increasing the coupling λ leads to a further reduction of the polaronic bandwidth and the appearance of additional continua separated by Ω . Finally, in the very strong interacting limit, the spectrum consists of flat bands with spacing Ω . In fact, the atomic limit $t \rightarrow 0$ can be solved exactly. We do not show the derivation here because we will solve a more general case – but with the same underlying method – in Chapter 2. To summarize, the main properties observed for the Holstein model are:

- Interaction with phonons leads to a bound state, the *polaron*.
- The dressing of a free carrier with a cloud of phonons increases its *effective mass*

- The larger the coupling, the larger the effective mass.
- MA works best for ground-state properties.

For more in-depth discussion and some of the finer points of MA, such as its difference to Dynamical Mean Field Theory (DMFT), we refer the reader to the literature [1, 12, 13, 21].

These results set the stage for our extensions to the standard (linear) Holstein model. In our derivation and motivation of the electron-phonon coupling term, there was no a-priori reason for assuming that the two ionic potentials I and II in Fig. 1.1 only differ in the equilibrium position but not in the phonon frequency. Furthermore, the harmonic approximation for potentials I and II is only valid for *small* lattice distortions, whereas large coupling, as we have seen, predicts *large* lattice distortions. Hence, the linear model's predictions at strong coupling invalidate its assumptions and a more thorough approach is required. In Chapter 2, we study the effect of including terms up to fourth order in the lattice coordinates. We will show how even small non-linear terms have a big qualitative and quantitative effect on the polaron properties. Next, we study a particularly interesting special case of a non-linear electron-phonon model where the lattice potential contains only *even* terms in the phonon coordinates. For certain parameters, this leads to a model where the carrier's presence turns the local single-well lattice potential into a double-well. This is studied in the single-carrier case in Chapter 3 and for the two-carrier case in Chapter 4. We find that the peculiar nature of the el-ph interaction leads to quasiparticles and bound pairs of quasiparticles (so-called bipolarons) that have properties that are distinctly different from those of linear models.

1.3 The three-band Emery model for a cuprate layer

One of the longest standing puzzles in solid state physics is the microscopic origin of high-temperature superconductivity in the cuprates [22]. We show

1.3. The three-band Emery model for a cuprate layer

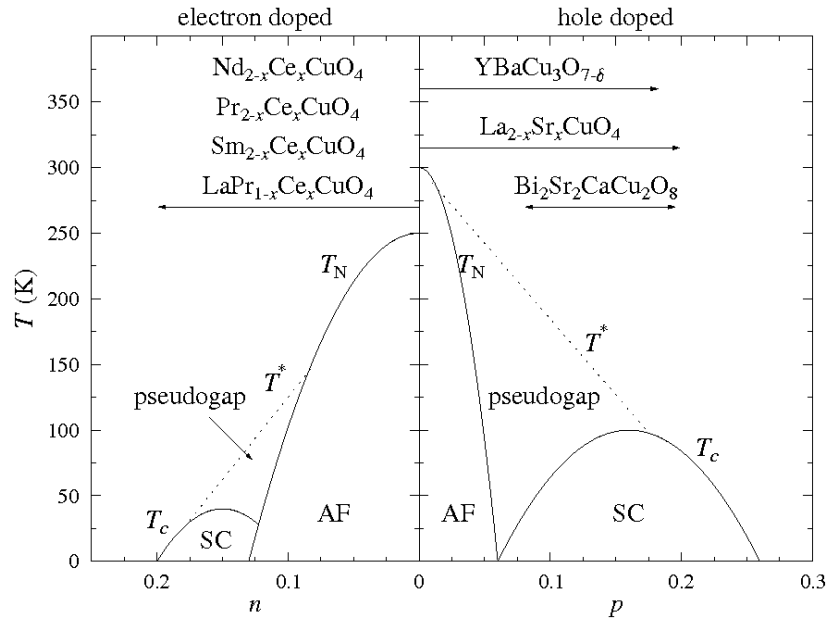


Figure 1.4: Phase diagram of the high-temperature superconducting cuprates for both electron and hole doping. The undoped compounds are antiferromagnetic insulators which become superconducting upon either hole or electron doping. Here, we focus on the hole-doped side of the phase diagram. Public domain figure from <https://en.wikipedia.org/wiki/File:Cuphasediag.png>.

1.3. The three-band Emery model for a cuprate layer

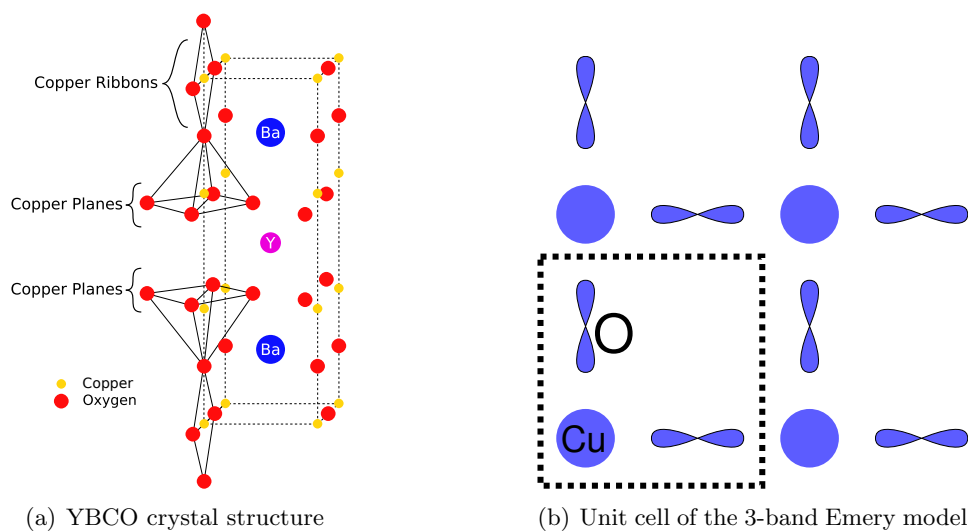


Figure 1.5: (a) Structure of a typical high-temperature superconducting cuprate compound, YBCO. Layers of copper and oxygen are contained within a host structure of rare-earth and transition metal elements. Figure used under the GFDL, as obtained from <https://commons.wikimedia.org/wiki/File:Ybco002.svg>. (b) The most relevant orbitals for cuprate physics are the copper $d_{x^2-y^2}$ orbital (round shapes) and the ligand oxygen p_x and p_y orbitals (lobes), forming a unit cell with three orbitals.

1.3. The three-band Emery model for a cuprate layer

their crystal structure and typical phase diagram in Fig. 1.4. The parent compounds are antiferromagnetic insulators. Upon doping electrons or holes into them, they become superconducting. Here, we focus on the case of doping a single hole into the insulating parent compound. While superconductivity only arises at finite doping, the “simple” case of having a single carrier doped into the system is already very complex, as we shall see below.

With the goal of arriving at a model Hamiltonian that is simple enough, but not too simple, we will discuss the progression of proposed model Hamiltonians. Experiments have shown that the important physics happen in two-dimensional CuO₂ layers of copper and oxygen. In the un-doped case, the relevant orbitals close to the Fermi energy are the copper’s in-plane $d_{x^2-y^2}$ orbital and the oxygen’s p_x and p_y orbitals. The cuprates are so-called charge-transfer insulators. This means that inserting an electron (removing a hole) takes place on the copper sites whereas removing an electron (inserting a hole) takes place on the oxygen sites [23]. A popular model Hamiltonian, then, is the so-called p - d or Emery model [24]. We give here the so-called 3-band version, where as a further approximation we note that the copper orbital has the largest overlap with those oxygen orbitals that are aligned with it. A unit cell for this model thus contains three sites and three orbitals as shown in Fig. 1.5(b). Its Hamiltonian is then given by (compare also its extensive discussion in [6])

$$H_{3B} = T_{pd} + T_{pp} + \Delta_{pd} \sum n_{l+\epsilon, \sigma} + U_{pp} \sum n_{l+\epsilon, \uparrow} n_{l+\epsilon, \downarrow} + U_{dd} \sum n_{l\uparrow} n_{l\downarrow} \quad (1.15)$$

with

$$T_{pd} = t_{pd} \sum \left(-p_{l+\epsilon, \sigma}^\dagger + p_{l-\epsilon, \sigma}^\dagger \right) d_{l\sigma} + h.c. \quad (1.16)$$

$$T_{pp} = t_{pp} \sum s_\delta p_{l+\epsilon+\delta}^\dagger p_{l+\epsilon, \sigma} - t'_{pp} \sum \left(p_{l-\epsilon, \sigma}^\dagger + p_{l+3\epsilon, \sigma}^\dagger \right) p_{l+\epsilon, \sigma} \quad (1.17)$$

$$n_{l, \sigma} = d_{l, \sigma}^\dagger d_{l, \sigma} \quad (1.18)$$

$$n_{l+\epsilon, \sigma} = p_{l+\epsilon, \sigma}^\dagger p_{l+\epsilon, \sigma} \quad (1.19)$$

In this Hamiltonian, T_{pd} describes hopping between oxygen and copper,

1.3. The three-band Emery model for a cuprate layer

Table 1.1: Relevant parameters for the 3-band Emery model in units of eV.

t_{pd}	t_{pp}	t'_{pp}	Δ_{pd}	U_{pp}
1.3	0.65	0.38	3.6	4

T_{pp} describes oxygen-oxygen nearest (t_{pp}) and next-nearest (t'_{pp}) neighbor hopping. The next-nearest neighbor hopping is, in fact, mediated by the copper $4s$ orbitals. Other hoppings, such as y -direction hopping between two p_x orbitals, is neglected. s_δ is the sign of the matrix elements between various oxygen p orbitals. It depends on our arbitrary choice of the orbitals' phases. We make our choice such that $s_\delta = 1$ for hopping along the main diagonal (upper-right and lower-left) and -1 for the other directions. The charge-transfer energy, i.e., the energy cost of moving a hole from a copper to an oxygen site, is given by Δ_{pd} . The on-site Coulomb repulsions are given by U_{dd} and U_{pp} , respectively. Numerical values for these parameters have been obtained from ab-initio calculations in [25] and are presented in Table 1.1.

Despite being a relatively simple Hamiltonian, the model in (1.15) already contains a variety of approximations, such as neglecting longer-range Coulomb interaction and longer range hopping. Despite this, it is still regarded as too complex to be solved directly due to its many degrees of freedom. Hence, a simpler model Hamiltonian is required. Zhang and Rice, in their seminal work, argued that although hole insertion occurs on the oxygen sites, a particular linear combination of the four ligand oxygen orbitals around a copper orbital forms a singlet with that orbital, the so-called Zhang Rice singlet [26]. By discarding all other linear combinations of the oxygen orbitals, one arrives at an effective single-band model where the Zhang Rice singlet (ZRS) combines the hole's charge degree of freedom with the copper ion's spin degree of freedom into a singlet object. This object then hops in the antiferromagnetic (AFM) background of the copper sites and gives rise to the so-called tJ -model, where t refers to the single-band hopping and J to the exchange interaction of the AFM background. As it turns out, the tJ -model itself does not adequately describe the single-particle dispersion of the

hole-doped cuprates. To obtain agreement with experiments, longer range hopping is added to the model to arrive at the t - t' - t'' - J model. With this extended model, quantitative agreement with the experimental dispersion is reached for a suitable choice of the parameters.

While these models have received considerable attention from the physics community [26–34], a clear and convincing picture of superconductivity in the cuprates has still not emerged. There is some evidence that one-band models fail to capture the essential physics of the cuprates. However, we still need to simplify the Hamiltonian (1.15). This is achieved in two steps: First, we apply the $U_{dd} \rightarrow \infty$ limit to the three-band Emery model instead of the single-band Hubbard model. The resulting model contains a variety of interesting higher-order effective terms which will be discussed in Chapter 5. It has been studied numerically via exact diagonalization in Bayo Lau’s dissertation [6]. A further significant approximation was made by Hadi Ebrahimejad [3, 5]; it neglects spin-fluctuations between the copper holes. While these fluctuations are important in the $t - J$ model, he showed that they play only a very little role in the Emery model. This approximation allows for a variational approach much like MA in the phonon case, where the variational space restricts the number of magnons present in the system. Good qualitative convergence is obtained for even just one magnon, and excellent quantitative convergence is obtained for two magnons, as demonstrated in Fig. 1.6.

Curiously, despite being based on vastly differing physics, these single- and many-band models agree on the single-particle dispersion. It is therefore not quite clear which of them more appropriately describes the cuprate physics. In Chapter 5, we consider an extension to the cuprates based on the newly synthesized tetragonal copper oxide T-CuO. We show how careful experiments with this material can settle this longstanding modeling question.

1.4 Outline

The remainder of this thesis is organized as follows. Chapter 2 discusses in detail the single-polaron physics of the nonlinear Holstein model. We

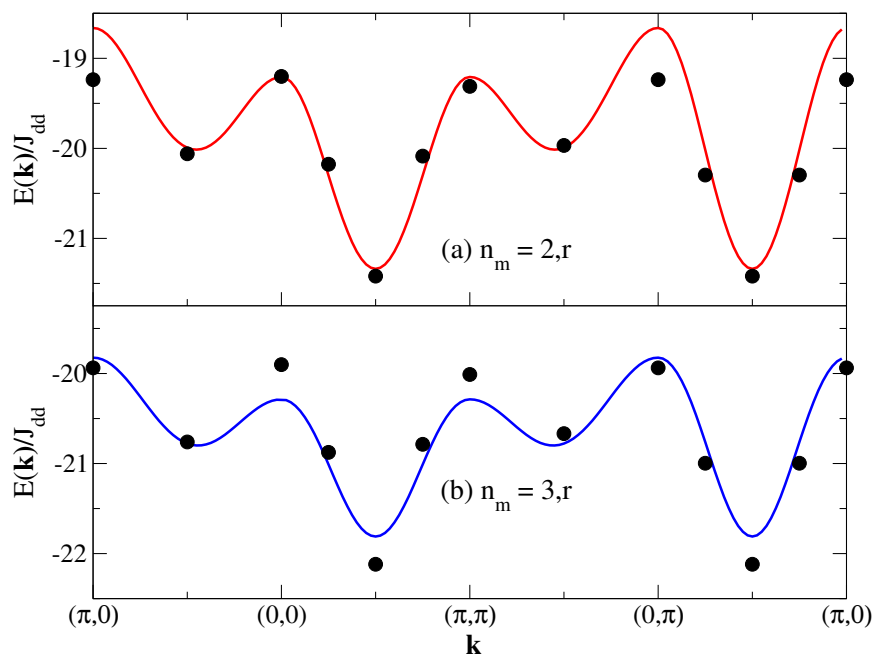


Figure 1.6: $E(\mathbf{k})$ along several cuts of the Brillouin zone for the three-band model in the variational approximation described in [3, 5] with (a) at most 2 magnons and (b) at most 3 magnons. Circles show exact diagonalization results from [6] for a cluster of 32 copper and 64 oxygen orbitals. Full lines show the results from the variational approximation, neglecting spin fluctuations. The overall agreement is excellent and can be further improved by including local spin fluctuations [5].

find that at moderate to strong linear coupling, the addition of even small quadratic terms drastically alters the polaron properties. Chapter 3 introduces a special variation of the nonlinear Holstein model, the double-well electron-phonon coupling model. In this model, the presence of a charge carrier switches the local lattice potential from a single- to a double-well. We study in detail the single-polaron properties of this model and find that they cannot be described with an effective linear Holstein model. We continue the study of this model in Chapter 4, where we investigate the bi-polaron, a bound state made of two charge carriers and a cloud of phonons. Our results here indicate that realistic parameter regimes exist for which the bi-polaron is strongly bound yet lightweight, in contrast to the results of other el-ph coupling models where the bi-polaron's mass increases drastically the stronger it is bound. Finally, in Chapter 5 we study a system where the relevant bosons are magnons instead of phonons; for a layer of tetragonal copper oxide (T-CuO) we study the dispersion of a single hole doped into the oxygen orbitals. Here, our finding is that the small inter-sublattice hopping sufficiently changes the symmetry properties of the resulting quasiparticle (a spin-polaron) from those of CuO_2 that experimental studies of T-CuO will be able to settle longstanding questions regarding the single-particle physics of the underdoped cuprates.

Chapter 2

Nonlinear Holstein model

In this chapter, we introduce a generalized Holstein model with nonlinear electron-phonon couplings. The model is then studied with the momentum-average approximation. We find that the inclusion of even small non-linear terms can have drastic effects on the properties of the system. This chapter also provides further review of the momentum average approximation.

2.1 Introduction

Coupling of carriers to phonons and the properties of the resulting quasiparticles, the polarons, are important for many materials, *e.g.* organic semiconductors [35, 36], cuprates [37–42], manganites [43], two-gap superconductors like MgB₂ [44–47], etc. In some cases the effective electron-phonon (el-ph) coupling λ is known quite accurately. For others, like the cuprates, estimates range from very small ($\lambda \sim 0.3$) to very large ($\lambda \sim 10$) [48, 49]. One possible explanation for this is that, especially for stronger couplings where simple perturbational expressions are no longer valid, properly fitting the experimental data to theoretical models can be quite involved [50].

Here we consider another possible explanation, namely that at strong el-ph coupling, simple theoretical models may not be valid anymore.

As mentioned in the introduction to this thesis, all widely-used models [11, 51] assume at the outset that the displacements x_i of the atoms out of equilibrium are small enough to justify expanding the electron-lattice interactions to linear order in x_i . These linear models generically predict the formation of small polarons or bipolarons at strong coupling, with the carrier(s) surrounded by a robust phonon cloud. As a result, lattice distortions $\langle x_i \rangle$ are considerable near the carrier(s). Hence, the linear models are based

2.1. Introduction

on assumptions which are in direct opposition to their predictions.

In this chapter we investigate this issue in the *single polaron limit*, relevant for the study of weakly doped materials like very underdoped cuprates [52, 53] and organic semiconductors [35, 36], and for cold atoms/molecules simulators [54–57]. We study the ground-state (GS) of a single polaron in a generalized Holstein model including el-ph coupling up to quartic order in x_i to test the importance of the higher order terms. We find that for strong linear coupling even very small quadratic terms *drastically* change the properties of the polaron. Moreover, we show that these effects go beyond a mere renormalization of the parameters of the linear Holstein model. As a result, attempts to find effective parameters appropriate for a linear model by using its predictions to fit the properties of real systems are doomed to failure, as different values will be obtained from fitting different properties. This offers another possible explanation for the wide range of estimates of the el-ph coupling in some materials. More importantly, it means that we must seriously reconsider how to characterize such interactions when they are strong. Furthermore, this calls for similar investigations of the validity of these linear models at finite carrier concentrations, since it is reasonable to expect that they also fail in the strong coupling limit.

To the best of our knowledge, we present here the first systematic, non-perturbative study of the importance of higher-order el-ph coupling terms on single polaron properties. We note that in previous work going beyond linear models, purely quadratic (no linear term) but weak el-ph coupling was discussed for organic metals using perturbation theory [58, 59], while linear and quadratic el-ph coupling was studied in the context of high- T_C superconductivity in Ref. [60]. A semi-classical study of some non-linear coupling potentials was carried out in Ref. [61].

This chapter is organized as follows: in Section 2.2 we introduce and motivate the nonlinear Holstein model in more detail than we did in the introduction. In Section 2.3 we show the modifications to the momentum average approximation necessary to solve the model. The results are discussed in Section 2.4. An outlook and concluding remarks are given in Section 2.5.

2.2 Model

We start this section with stating the model Hamiltonian for the generalized nonlinear Holstein model introduced in [62] and the introduction.

$$\mathcal{H} = \mathcal{H}_{\text{el}} + \mathcal{H}_{\text{ph}} + \mathcal{H}_{\text{el-ph}}, \quad (2.1)$$

The remainder of this section will derive, motivate and explain these terms.

The Holstein Hamiltonian models a charge carrier in a molecular crystal like the 1D example sketched in Fig. 2.1(a). A charge carrier introduced in such a crystal hops between “molecules”, as described by

$$\mathcal{H}_{\text{el}} = \sum_{\mathbf{k}} \epsilon_{\mathbf{k}} c_{\mathbf{k}}^{\dagger} c_{\mathbf{k}}, \quad \text{with} \quad \epsilon_{\mathbf{k}} = -2t \sum_{\alpha=1}^d \cos(k_{\alpha}) \quad (2.2)$$

for nearest-neighbor hopping on a d -dimensional simple cubic lattice.

Fig. 2.1(b) illustrates how the lattice part is handled. In the absence of a carrier, the potential has some form (curve I) which is approximated as a parabola and leads to $\mathcal{H}_{\text{ph}} = \Omega \sum_i b_i^{\dagger} b_i$. This describes harmonic oscillations of each “molecule” about its equilibrium distance R . If a carrier is present, the potential has some other form (curve II). The difference between I and II leads to $\mathcal{H}_{\text{el-ph}}$. Its details are material specific; here we propose two models and choose a generic form based on them.

The first model assumes that the carrier occupies an orbital of the ion with opposite charge. The attraction between them is then some constant, whereas the Coulomb repulsion between the carrier and the ion of like charge is

$$U(x_i) = \frac{U_0 n_i}{1 - \frac{x_i}{R}} = U_0 n_i \sum_{n=0}^{\infty} \left(\frac{x_i}{R} \right)^n$$

where $n_i = 1$ ($n_i = 0$) if the carrier is (is not) present and $U_0 > 0$ is the characteristic energy. Using the expression of the position operator in terms of the phonon creation and annihilation operators, $x_i = \sqrt{\frac{\hbar}{2\mu\Omega}} (b_i + b_i^{\dagger})$ where μ is the reduced mass of the molecule, and truncating the series at $n = 4$

2.2. Model

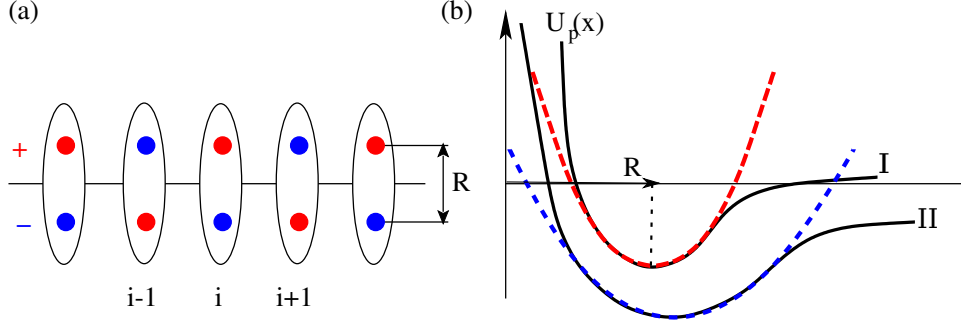


Figure 2.1: (a) Sketch of a 1D chain of polar molecules; (b) The potential of the pair with (II) or without (I) an extra charge carrier (full lines) is approximated by a polynomial (thick dashed lines)

leads to:

$$\mathcal{H}_{\text{el-ph}} = \sum_{n=1}^4 \mathcal{H}_{\text{el-ph}}^{(n)} = \sum_{n=1}^4 g_n \sum_i c_i^\dagger c_i (b_i + b_i^\dagger)^n, \quad (2.3)$$

where $g_n = g_1 \zeta^{n-1}$ with $\zeta = A/R$ and $A = \sqrt{\hbar/(2\mu\Omega)}$ the zero-point amplitude of the harmonic oscillator.

The second model assumes that the carrier is an electron (hole) that occupies an anti-bonding (bonding) orbital of the molecule; all bonding orbitals are initially full since the parent crystal is an insulator. In both cases the energy increases by an overlap integral which decreases exponentially with the distance:

$$U(x_i) \sim n_i e^{-\frac{R-x_i}{a_B}} \quad (2.4)$$

where a_B is the Bohr radius. A Taylor expansion to fourth order in x_i leads again to Eq. (2.3) but now

$$\frac{g_n}{g_1} = 2^{n-1} \frac{\zeta^{n-1}}{n!} \quad \text{for} \quad \zeta = \frac{g_2}{g_1} = \frac{A}{2a_B}, \quad (2.5)$$

where again $A = \sqrt{\hbar/(2\mu\Omega)}$.

We define the following special cases:

Linear model The case where only $g_1 \neq 0$. This is the standard Holstein model.

Quadratic model The case where only $g_1 \neq 0$ and $g_2 \neq 0$.

Quartic model The case where all $g_n \neq 0$ for $n \leq 4$.

The case with only $g_4 = 0$ is not considered because it is unstable: A polynomial with degree 3 will always diverge to $-\infty$ for one of the directions $x \rightarrow \pm\infty$.

As discussed in the introduction, the linear Holstein model is characterized by two dimensionless parameters: the effective coupling strength $\lambda = g_1^2/(2dt\Omega)$, where d is the dimension of the lattice, and the adiabaticity ratio $\Omega/(4dt)$. As long as the latter is not very small, the former controls the phenomenology, with the crossover to small polaron physics occurring for $\lambda \sim 1$ [63]. For ease of comparison, we continue to use these parameters when characterizing the higher order models. For the quadratic model, the new energy scale g_2 results in a third dimensionless parameter $\zeta = g_2/g_1$. For the quartic model there are two more parameters g_n/g_1 , $n = 3, 4$. Both scale like ζ^{n-1} but with different prefactors. We use $g_n/g_1 = \zeta^{n-1}$ like in the first model since for the second model the prefactors are less than 1, making these terms smaller and thus less important.

For specificity, from now we assume $\zeta > 0$ ($\zeta < 0$ is briefly discussed at the end of this chapter, and extensively in later chapters). As we show below, in this case we find that while quadratic terms are important when the linear coupling is large, addition of the $n = 3, 4$ terms only leads to small quantitative changes and can be ignored. This justifies *a posteriori* why we do not include anharmonic corrections in \mathcal{H}_{ph} and/or higher order terms with $n > 4$ in the electron-phonon coupling.

2.2.1 Summary of model assumptions

Recalling the caveat for model Hamiltonians, we summarize here the assumptions that went into the model Hamiltonian and give their justification.

First, quartic terms in the free-phonon part of the Hamiltonian were neglected. This will be justified *a posteriori* by the results, which will show that quartic terms in the el-ph coupling have only a small effect on the polaron properties.

Second, the coefficients g_n follow a power-law dependence on the linear coupling, $g_n \sim \zeta^{n-1}g_1$. This is motivated by observing this relation for two different physical origins of electron-phonon coupling.

Finally, we assume $\zeta > 0$. This is not so much a model assumptions as it is a focus on one region of parameter space. The case of $\zeta < 0$ will be explored in the next chapter.

2.3 Formalism

We now describe in detail the MA solution for the quadratic model. The calculations for the quartic model are analogous but much more tedious.

We want to find the single particle Green's function

$$G(\mathbf{k}, \omega) = \langle 0 | c_{\mathbf{k}} \hat{G}(\omega) c_{\mathbf{k}}^\dagger | 0 \rangle \quad (2.6)$$

where $\hat{G}(\omega) = [\omega - \mathcal{H} + i\eta]^{-1}$ is the resolvent for this Hamiltonian, with $\eta \rightarrow 0$ a small positive number and $|0\rangle$ the vacuum state. From this we can extract all the polaron's GS properties [12]. We rewrite the quadratic Hamiltonian as $\mathcal{H} = \mathcal{H}_0 + \mathcal{H}_1$, where

$$\mathcal{H}_0 = \mathcal{H}_{\text{el}} + \mathcal{H}_{\text{ph}} + g_2 \sum_i c_i^\dagger c_i \left(2b_i^\dagger b_i + 1 \right) \quad (2.7)$$

$$\mathcal{H}_1 = \sum_i c_i^\dagger c_i \left[g_1 (b_i^\dagger + b_i) + g_2 (b_i^{\dagger 2} + b_i^2) \right]. \quad (2.8)$$

The equation of motion (EOM) for the propagator is obtained recursively from Dyson's identity,

$$\hat{G}(\omega) = \hat{G}_0(\omega) + \hat{G}(\omega) \mathcal{H}_1 \hat{G}_0(\omega) \quad (2.9)$$

where $\hat{G}_0(\omega) = [\omega - \mathcal{H}_0 + i\eta]^{-1}$ is the resolvent for \mathcal{H}_0 . Using it in $G(\mathbf{k}, \omega)$ yields the EOM

$$G(\mathbf{k}, \omega) = G_0(\mathbf{k}, \omega) \left[1 + \sum_{n=1}^2 \sum_i \frac{e^{i\mathbf{k} \cdot \mathbf{r}_i}}{\sqrt{N}} g_n F_n(\mathbf{k}, \omega; i) \right] \quad (2.10)$$

2.3. Formalism

where $F_n(\mathbf{k}, \omega; i) = \langle 0 | c_{\mathbf{k}} \hat{G}(\omega) c_i^\dagger (b_i^\dagger)^n | 0 \rangle$, which we call a generalized propagator.

So far, everything has been exact and very similar to the treatment of the linear Holstein model in Chapter 1, with the exception that our \mathcal{H}_0 is slightly more complicated, since in addition to free electron propagation it also contains a potential scattering term off the phonons. Following the basic steps of the momentum average approximation (MA) [12, 13] we let

$$\tilde{g}_0(\omega) = \frac{1}{N} \sum_{\mathbf{k}} \frac{1}{\omega - \epsilon_{\mathbf{k}} + i\eta} \quad (2.11)$$

denote the *momentum averaged* propagator of a free particle with dispersion $\epsilon_{\mathbf{k}}$. Now consider the propagator associated with \mathcal{H}_0 in real space:

$$G_0(i - j, \omega; n) = \frac{1}{n!} \langle 0 | c_i b_i^n \hat{G}_0(\omega) (b_i^\dagger)^n c_i^\dagger | 0 \rangle. \quad (2.12)$$

This is the on-site real-space propagator of an otherwise free carrier being scattered by the on-site potential $2g_2n$ while there are n phonons in the system, as described by (2.7). We show in B.1 that for $i = j$, we have

$$G_0(i - j = 0, \omega; n) = \left[\frac{1}{\tilde{g}_0(\omega - n\Omega - g_2)} - 2g_2n \right]^{-1}. \quad (2.13)$$

The momentum average approximation now consists of setting

$$G_0(i - j, \omega; n) \approx \delta_{ij} G_0(i - j, \omega; n) = \bar{g}_0(\omega; n) \text{ for any } n \geq 1. \quad (2.14)$$

with $\bar{g}_0(\omega; n) = \tilde{g}_0(\omega - n\Omega - g_2)$. In words, the real-space free propagator appearing in the higher-order iterations of Dyson's identity is approximated as being purely on-site. This is justified because the polaron GS energy lies below the free particle spectrum, and for such energies the free-particle propagator decreases exponentially with $|i - j|$. Thus, MA keeps the largest contribution and ignores the exponentially smaller ones. This becomes exact in the strong-coupling limit $t \rightarrow 0$. Since phonon creation and annihilation is contained within \mathcal{H}_1 , the effect of this approximation is that new phonons

2.3. Formalism

can only be created at a site where there already are phonons. At this level of approximation, MA can be viewed as a variational method where only states of the form

$$\sum_{ij} c_i^\dagger (b_j^\dagger)^n |0\rangle \quad (2.15)$$

are considered, i.e., states with at most one single-site phonon cloud.

By eliminating propagators that take the carrier away from the phonon cloud, MA allows us to obtain a simplified hierarchy of EOM involving only the generalized Green's functions F_n . For any $n \geq 1$, they read:

$$F_n(\mathbf{k}, \omega; i) = \bar{g}_0(\omega; n) \cdot [n(n-1)g_2 F_{n-2}(\mathbf{k}, \omega; i) + ng_1 F_{n-1}(\mathbf{k}, \omega; i) + g_1 F_{n+1}(\mathbf{k}, \omega; i) + g_2 F_{n+2}(\mathbf{k}, \omega; i)].$$

Since the arguments of all F_n propagators are the same, we suppress them in the following for simplicity. The important achievement is that now each generalized propagator is linked via its EOM to only a finite set of generalized propagators.

In the original MA approach for the linear Holstein model, the EOM coupled the generalized propagator of order n to those of orders $n \pm 1$. Here, now the connection is to propagators of orders $n \pm 1, n \pm 2$. As a consequence, the EOM cannot be reduced to a simple continued fraction anymore. Instead, we will obtain a *continued matrix fraction*: Following the technique introduced in Ref. [2], we reduce these EOMs to a simple recursive relation. This is achieved by introducing a vector $\mathbf{W}_n = (F_{2n-1}, F_{2n})$. The EOM for \mathbf{W}_n are $\gamma_n \mathbf{W}_n = \alpha_n \mathbf{W}_{n-1} + \beta_n \mathbf{W}_{n+1}$, where the α_n , β_n and γ_n are 2×2 matrices whose coefficients are read off of the EOM, namely

$$\alpha_n|_{11} = (2n-1)(2n-2)g_2\bar{g}_0(\omega; 2n-1), \quad (2.16)$$

$$\alpha_n|_{12} = (2n-1)g_1\bar{g}_0(\omega; 2n-1), \quad (2.17)$$

$$\alpha_n|_{21} = 0, \quad (2.18)$$

$$\alpha_n|_{22} = 2n(2n-1)g_2\bar{g}_0(\omega; 2n), \quad (2.19)$$

while

$$\beta_{\mathbf{n}} = \begin{pmatrix} g_2 \bar{g}_0(\omega; 2n-1) & 0 \\ g_1 \bar{g}_0(\omega; 2n) & g_2 \bar{g}_0(\omega; 2n) \end{pmatrix}, \quad (2.20)$$

$$\gamma_{\mathbf{n}} = \begin{pmatrix} 1 & -g_1 \bar{g}_0(\omega; 2n-1) \\ -2ng_1 \bar{g}_0(\omega; 2n) & 1 \end{pmatrix}. \quad (2.21)$$

This simple recursive relation for $\mathbf{W}_{\mathbf{n}}$ has the solution $\mathbf{W}_{\mathbf{n}} = \mathbf{A}_{\mathbf{n}} \mathbf{W}_{\mathbf{n}-1}$ for any $n \geq 1$, where $\mathbf{A}_{\mathbf{n}}$ are 2×2 matrices obtained from the infinite continued fraction

$$\mathbf{A}_{\mathbf{n}} = [\gamma_{\mathbf{n}} - \beta_{\mathbf{n}} \mathbf{A}_{\mathbf{n}+1}]^{-1} \alpha_{\mathbf{n}}. \quad (2.22)$$

In practice, we start with $A_N = 0$ for a sufficiently large cutoff N , chosen so that the results are insensitive to further increases in it ($N \sim 100$ is usually sufficient).

We find $\mathbf{A}_{\mathbf{1}} = \begin{pmatrix} 0 & a_{12} \\ 0 & a_{22} \end{pmatrix}$, where a_{12} and a_{22} are obtained after using Eq. (2.22) $N-1$ times. As a result, $F_1 = a_{12} F_0$, $F_2 = a_{22} F_0$, where

$$G(\mathbf{k}, \omega) = \sum_i \frac{e^{i\mathbf{k} \cdot \mathbf{r}_i}}{\sqrt{N}} F_0(\mathbf{k}, \omega; i). \quad (2.23)$$

Using these in Eq. (2.10) leads to a solution of the form

$$G(\mathbf{k}, \omega) = \frac{1}{\omega - \epsilon_{\mathbf{k}} - \Sigma(\omega) + i\eta}, \quad (2.24)$$

with the MA self-energy for the quadratic model:

$$\Sigma(\omega) = g_1 a_{12}(\omega) + g_2 a_{22}(\omega). \quad (2.25)$$

The reason why the self-energy is local at this level of MA is the simplicity of this Hamiltonian, whose vertices are momentum independent; this issue is discussed at length for the linear Holstein model in Ref. [13]. At this point, we emphasize that MA is *not* equivalent – let alone inferior – to Dynamical Mean Field Theory. The latter *always* leads to a momentum-independent self-energy, whereas MA – even at its simplest level – achieves

momentum dependence for more complicated models, and becomes momentum dependent for even the simple Holstein model when higher orders of the approximation are used.

The quartic model is solved analogously. The main difference is that here the EOM for F_n involves 9 consecutive terms, from F_{n-4} to F_{n+4} . These can also be rewritten as simple recurrence relations $\gamma_{\mathbf{n}} \mathbf{W}_{\mathbf{n}} = \alpha_{\mathbf{n}} \mathbf{W}_{\mathbf{n}-1} + \beta_{\mathbf{n}} \mathbf{W}_{\mathbf{n}+1}$, but now $\alpha_{\mathbf{n}}$, $\beta_{\mathbf{n}}$ and $\gamma_{\mathbf{n}}$ are 4×4 matrices. Their expressions are too long to be listed here, but they can be found in Appendix B.2.

2.4 Results and discussion

To gauge the relevance of the higher-order el-ph coupling terms we plot in Fig. 2.2 the evolution with ζ of a polaron property that can be directly measured, namely the quasiparticle weight $Z = m/m^*$ where m, m^* are the carrier and the polaron mass, respectively. We also show the average phonon number N_{ph} . The results are for a one-dimensional chain. Results in higher dimensions are qualitatively similar to these 1D results for small λ , and become quantitatively similar to them in the interesting regime of large λ where all of them converge towards those of the atomic limit $t = 0$.

First, we note that the $\zeta = 0$ intercepts trace the predictions of the linear model: with increased coupling λ , Z decreases while N_{ph} increases as the polaron acquires a robust phonon cloud [63, 12]. From these intercepts, we estimate that the linear model predicts the crossover to the small polaron regime to occur around $\lambda \sim 1.5$ for this adiabaticity ratio and dimension.

The quadratic model, whose predictions are indicated by lines, shows a very strong dependence of ζ for strong linear coupling $\lambda \geq 1.5$: here both Z and N_{ph} vary by about an order of magnitude as ζ increases from 0 to 0.1. For higher ζ , Z and N_{ph} have a slight turnaround towards smaller/larger values, for reasons explained below, but are still consistent with a large polaron. These results indicate that the quadratic term can completely change the behavior of the polaron in the limit of medium and large λ . For example, in the quadratic model at $\lambda = 1.5$ and $\zeta \sim 0.1$ the polaron is light and with a small phonon cloud, in total disagreement with the linear model

prediction of a heavy small polaron at this λ .

Of course, this raises the question of how large ζ is. The answer is material specific, but as an extreme case, let H_2 be the unit of the molecular crystal. This case is described by model two, so $\zeta \sim 2A/a_B$, where $a_B \approx 0.5\text{\AA}$ while $A \approx 0.1\text{\AA}$ if we use $\Omega \approx 0.5\text{eV}$ appropriate for a H_2 molecule [64]. This leads to a very large $\zeta \sim 0.4$. Other atoms are heavier but phonon frequencies are usually much smaller than 0.5eV , so it is not clear whether $A \sim 1/\sqrt{\mu\Omega}$ changes much. The Bohr radius (or distance R between atoms, for model 1) is usually larger than 0.5\AA but not by a lot, maybe up to a factor 5 for R ; thus we expect smaller ζ in real materials but the change is likely not by orders of magnitude. Fig. 2.2 shows that values as small as $\zeta \sim 0.05$ already lead to significant quantitative changes in m^* .

Inclusion of cubic and quartic terms (the symbols show the results of the quartic model) further changes Z and N_{ph} , but these changes are much smaller for all ζ , of up to $\sim 10\%$ when compared to the quadratic model values, as opposed to order of magnitude changes between the quadratic and the linear models. Thus, these terms are much less relevant and can be ignored without losing much accuracy. As discussed, their small effect explains why we do not consider terms with even higher order n , nor $n = 4$ anharmonic terms in the phonon Hamiltonian.

2.4.1 Atomic limit

To understand the effects of the quadratic term at large λ , we study it in the atomic limit $t = 0$ ($\lambda = \infty$) where the carrier remains at one site and interacts only with the phonons of that site. Focusing on this site, its quadratic Hamiltonian $\mathcal{H}_{\text{at}}^{(2)} = \Omega b^\dagger b + \sum_{n=1}^2 g_n (b^\dagger + b)^n$ is well-studied in the field of quantum optics, where it describes so-called squeezed coherent states [65]. The extra charge changes the origin and spring constant of the original harmonic oscillator which means that the Hamiltonian is easily diagonalized by changing to new bosonic operators $\gamma^\dagger = ub^\dagger + vb + w$, where u , v and w

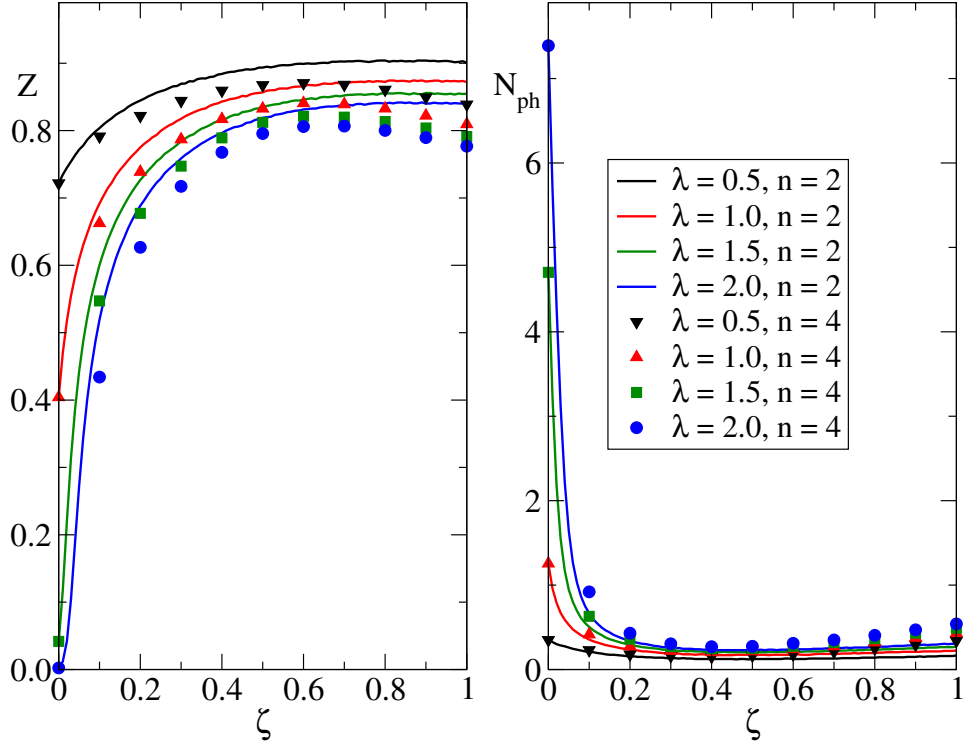


Figure 2.2: GS quasiparticle weight (left panel) and GS average phonon number (right panel) vs. ζ , in the quadratic ($n = 2$, lines) and quartic ($n = 4$, symbols) models, for various values of λ and $\Omega = 0.5t$, in one dimension.

2.4. Results and discussion

are such that $\mathcal{H}_{\text{at}}^{(2)} = \Omega_{\text{at}} \gamma^\dagger \gamma + E_{\text{GS}}^{(\text{at})}$. We find

$$\Omega_{\text{at}} = \sqrt{\Omega(\Omega + 4g_2)} \quad (2.26)$$

$$u = \sqrt{(\Omega + 2g_2 + \Omega_{\text{at}}) / (2\Omega_{\text{at}})} \quad (2.27)$$

$$w = g_1 \sqrt{\Omega / \Omega_{\text{at}}^3} \quad (2.28)$$

$$v = \text{sgn}(g_2) \sqrt{(\Omega + 2g_2 - \Omega_{\text{at}}) / (2\Omega_{\text{at}})}. \quad (2.29)$$

From these, we obtain

$$E_{\text{GS}}^{\text{at}} = -\frac{g_1^2 \Omega}{\Omega_{\text{at}}^2} + \frac{1}{2}(\Omega_{\text{at}} - \Omega) \quad (2.30)$$

$$N_{\text{ph}}^{(\text{at})} = \frac{1}{2} \left[\frac{\Omega + 2g_2}{\Omega_{\text{at}}} - 1 \right] + \frac{g_1^2}{(\Omega + 4g_2)^2} \quad (2.31)$$

$$Z_{\text{at}} = \frac{1}{u} \exp \left[-w^2 \left(1 - \frac{v}{u} \right) \right]. \quad (2.32)$$

The latter result requires the expansion of the squeezed coherent states in the number state basis [66].

Figure 2.3 shows Z_{at} and $N_{\text{ph}}^{(\text{at})}$ vs. ζ (thick lines), which agree well with the corresponding $\lambda = 2$ results of Fig. 2.2. In particular, for $\zeta \rightarrow 0$ we find

$$\Omega_{\text{at}} = \Omega + 2g_1\zeta + \mathcal{O}(\zeta^2) \quad (2.33)$$

$$N_{\text{ph}}^{(\text{at})} = \frac{g_1^2}{\Omega^2} \left[1 - \frac{8g_1}{\Omega} \zeta + \mathcal{O}(\zeta^2) \right] \quad (2.34)$$

explaining their linear increase/decreases for small ζ .

The slight turnaround of the Z and N_{ph} curves at larger values of ζ is also observed in the atomic limit of the quadratic model. The reason is that the first term in $N_{\text{ph}}^{(\text{at})}$ *increases* whereas the second term *decreases* with ζ . As discussed above, for small ζ the second term dominates and the overall number of phonons decreases. For large ζ , however, the second term vanishes whereas the first term diverges as $\sqrt{g_2} = \sqrt{\zeta g_1}$. Hence, as ζ increases $N_{\text{ph}}^{\text{at}}$ has a minimum, and then starts to increase with ζ . Basically, here the $g_2(b^\dagger + b^2)$ coupling dominates over the linear coupling $g_1(b^\dagger + b)$ and

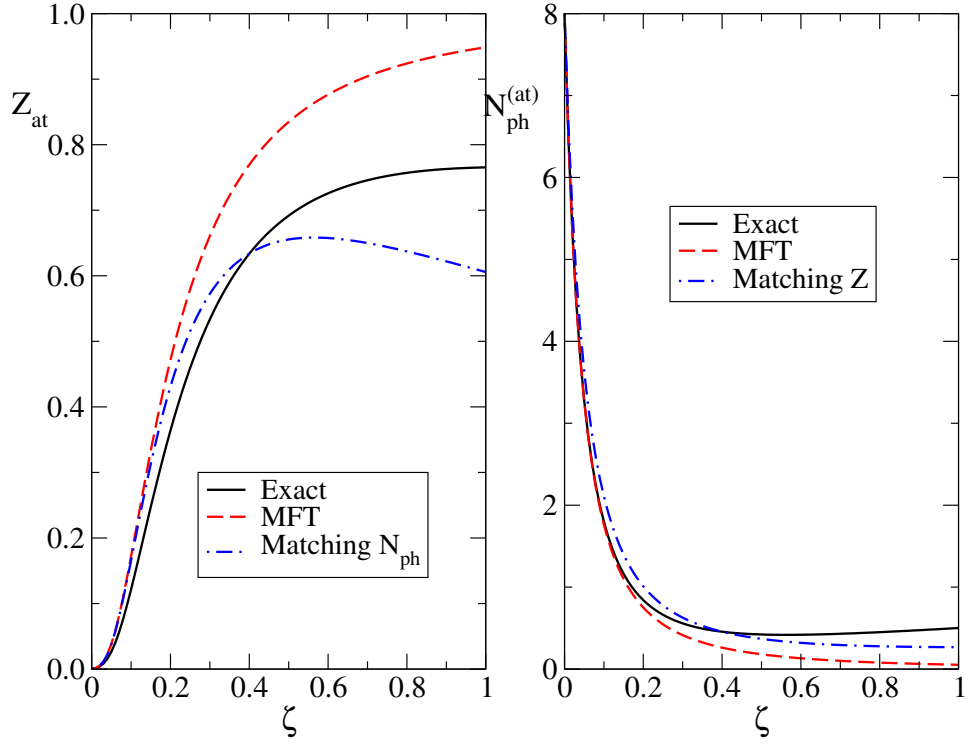


Figure 2.3: (left) Z_{at} , and (right) $N_{\text{ph}}^{(\text{at})}$ vs. ζ , for $g_1 = \sqrt{2}$ and $\Omega = 0.5$ (full lines). Dashed lines show the mean-field estimates, while the dot-dashed lines show the results of fitting $\tilde{g}/\tilde{\Omega}$ to exactly reproduce the other quantity. See text for more details.

2.4. Results and discussion

changes the trend. Physically, at small ζ the dominating effect is a narrowing of the harmonic potential, making phonons more costly to generate. At even larger ζ , the effect of shifting the origin to a new position dominates.

This leads us to pose the question whether these exact results of the quadratic atomic model can be fit well by an effective *linear* model $\mathcal{H}_{\text{at}}^{(1)} = \tilde{\Omega}b^\dagger b + \tilde{g}(b^\dagger + b)$, for some appropriate choice of the effective parameters $\tilde{\Omega}, \tilde{g}$. One way to achieve this is with a mean-field ansatz

$$b^{\dagger 2} \approx 2\langle b^\dagger \rangle b^\dagger - \langle b^\dagger \rangle^2, \quad (2.35)$$

with $\langle b^\dagger \rangle$ the GS expectation value of b^\dagger . The self-consistency condition

$$\langle b^\dagger \rangle = -\frac{g_1 + 2g_2\langle b^\dagger \rangle}{\Omega + 2g_2} \quad (2.36)$$

leads to the mean-field estimates

$$\tilde{\Omega}_{\text{MF}} = \Omega + 2g_2 \quad \tilde{g}_{\text{MF}} = g_1 - \frac{2g_1g_2}{\Omega + 4g_2}. \quad (2.37)$$

Thus, for small $\zeta = g_2/g_1$, $\tilde{\Omega}_{\text{MF}}$ increases whereas \tilde{g}_{MF} decreases with increasing ζ so the effective coupling $\tilde{\lambda} = \tilde{g}^2/(2dt\tilde{\Omega})$ decreases with ζ . This is consistent with the observed move away from the small polaron limit with increasing ζ . Quantitatively, however, these mean-field results (dashed lines in Fig. 2.3) are not very accurate for small ζ , and fail to capture even qualitatively the correct behavior when $\zeta \gg 1$, since here $N_{\text{ph}}^{(\text{at})} \rightarrow \infty$ while $N_{\text{ph}}^{(MF)} = \tilde{g}_{\text{MF}}^2/\tilde{\Omega}_{\text{MF}}^2 \rightarrow 0$.

In fact, there is no choice for effective linear parameters \tilde{g} and $\tilde{\Omega}$ that reproduces the results of the quadratic model. This is because in the linear model, both \tilde{Z} and \tilde{N}_{ph} are functions of $\tilde{g}/\tilde{\Omega}$ only. Fig. 2.3 shows that if one chooses this ratio so that $N_{\text{ph}}^{(\text{at})} = \tilde{N}_{\text{ph}}$, then \tilde{Z} (dot-dashed line in the left panel) disagrees with Z_{at} , and vice versa. Even more significant is the fact that even if one could find a way to choose $\tilde{g}, \tilde{\Omega}$ so that the overall agreement is satisfactory for all GS properties, the linear model's prediction for higher energy features would still be *completely wrong*. For example, it would

predict the polaron+one-phonon continuum to occur at $E_{GS} + \tilde{\Omega}$ instead of the proper $E_{GS} + \Omega$ threshold. Since in the atomic limit the predictions of the quadratic model cannot be reproduced with a renormalized linear model, we conclude that this must hold true at finite hopping t as well, at least for large λ where the quadratic terms are important.

So far we discussed moderate values of the adiabaticity ratio $\Omega/t = 0.5$, as well as the anti-adiabatic (atomic) limit. MA predicts similar results in the adiabatic limit $\Omega/t \rightarrow 0$ for large λ , where it remains accurate, but is unsuitable to study small and moderate couplings [13]. We expect that here the quadratic coupling is essential even for small couplings $\lambda \rightarrow 0$, because the term $2g_2 \sum_i b_i^\dagger b_i$ ensures that phonons are gapped even though $\Omega = 0$.

2.4.2 Negative nonlinear term

So far we also only discussed the case $\zeta > 0$. The behavior of models with $\zeta < 0$ can be glimpsed at from the exact results in the atomic limit. For small negative ζ , the results listed above show that the average phonon number $N_{\text{ph}}^{(\text{at})}$ increases with $|\zeta|$ while the qp weight Z_{at} decreases fast, i.e. the polaron moves more strongly into the small polaron limit. This is in agreement with the MA predictions for the quadratic model (not shown). Here, however, we must limit ourselves to values $|\zeta| < \Omega/(4g_1)$ so that Ω_{at} remains a real quantity (a similar threshold is found for the full quadratic model. Note that the value of this threshold decreases with increasing λ). For values of $|\zeta|$ above this threshold the quadratic model becomes unstable. This, of course, is unphysical. In reality, here one is forced to include higher order (anharmonic) terms in the phonon Hamiltonian \mathcal{H}_{ph} since they guarantee the stability of the lattice if the quadratic terms fail to do so. Such anharmonic terms may have little to no effect in the absence of the carrier, but clearly become important in its presence, in this limit. They can be treated with the same MA formalism we used here. Their effects, as well as a full analysis of all possible signs of the non-linearities and the resulting polaron physics will be presented in the next chapter. For now, it is obvious that in the case $\zeta < 0$, higher order terms in el-ph coupling also

play a key role in determining the polaron properties unless λ is very small, and therefore cannot be ignored.

2.4.3 Small carrier concentrations

The results presented so far clearly demonstrate the importance of non-linear el-ph coupling terms if the linear coupling λ is moderate or large, through their significant effects on the properties of a single Holstein polaron.

A reasonable follow-up question is whether such dramatic effects are limited to the single polaron limit or are expected to extend to finite carrier concentrations. While the limit of large carrier concentrations cannot be tackled with our approach, here we present strong evidence that quadratic terms are likely to be equally important at small but finite carrier concentrations.

Of course, for finite carrier concentrations one needs to supplement the Hamiltonian with a term describing carrier-carrier interactions. The simplest such term is an on-site Hubbard repulsion $\mathcal{H}_U = U \sum_i n_{i\uparrow} n_{i\downarrow}$, and gives rise to the Hubbard-Holstein Hamiltonian. The linear version of this Hamiltonian has been studied extensively by a variety of numerical methods [63]. In particular, for low carrier concentrations and focusing on the small polaron/bipolaron limit, the phase diagram has been shown to consist of three regions: (i) for large λ and small U , the deformation energy favours the formation of on-site bipolarons, also known as the S_0 bipolarons; (ii) increasing U eventually makes having two carriers at the same site too expensive, and the S_0 bipolarons evolve into weakly-bound S_1 bipolarons, where the two carriers sit on neighboring sites. The binding is now provided by virtual hopping processes which allow each carrier to interact with the cloud of its neighbor. However, at smaller λ and larger U this binding mechanism is insufficient to stabilize the S_1 bipolaron, and instead one finds (iii) a ground state consisting of unbound polarons.

This phase diagram has been found numerically in 1D [67] and 2D [68] for the linear Hubbard-Holstein model. Some results in 3D have also become available very recently [69]. In 1D and 2D, the separation lines between the

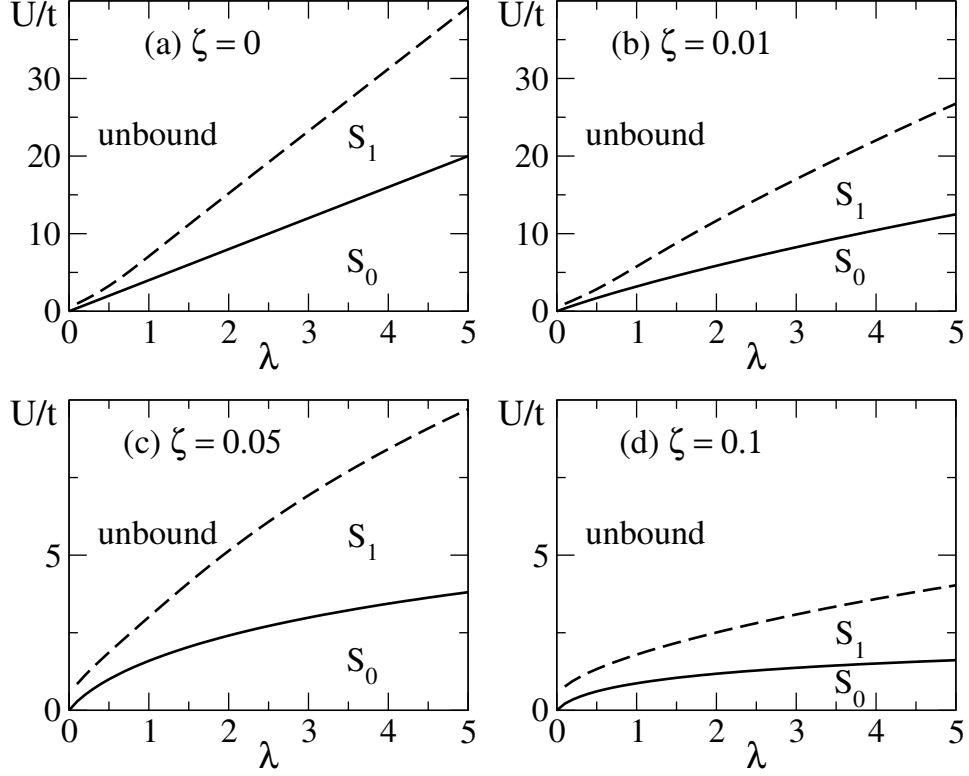


Figure 2.4: Estimate of the bipolaron phase diagram in 1D for $\Omega/t = 0.5$ and for different values of ζ , based on second order perturbation theory in t . In all four panels, the solid lines show the transition from S_0 (on-site) stable bipolarons to S_1 (nearest-neighbor) stable bipolarons, while the dashed lines show the unbinding transition above which bound polarons are unstable. Note that panels (c) and (d) have a significantly rescaled y -axis. See text for more details.

various phases are found to be close to those estimated using second order perturbation theory in the hopping t , starting from the atomic limit [67, 68]. This is expected since for large linear coupling λ , the results always converge toward those predicted by the atomic limit.

Since the quadratic Hamiltonian can be diagonalized exactly in the atomic limit, we use second order perturbation theory to estimate the location of the separation lines for various values of $\zeta > 0$. The results are shown in Fig. 2.4. Panel (a) shows the rough phase diagram for $\zeta = 0$, in agreement with the asymptotic estimates shown in Refs. [67, 68] (note that the definition of the effective coupling used in those works differs by various factors from our definition for λ). Panels (b)-(d) show a very significant change with increasing ζ . Even the presence of an extremely small quadratic term $\zeta = 0.01$ moves the two lines to considerably lower U values, as shown in panel (b), while for $\zeta = 0.05$ and 0.1 , the bipolarons are stable only in a very narrow region with small values of U (note that the vertical axes are rescaled for panels (c) and (d)).

The dramatic change with increasing ζ in the location of these asymptotic estimates for the various bipolaron transitions/crossovers strongly suggests that non-linear el-ph coupling terms remain just as important in the limit of small carrier concentrations as they have been shown to be in the single polaron limit. In particular, these results suggest that the presence of non-linear el-ph coupling terms leads to a significant suppression of the phonon-mediated interaction between carriers, so that the addition of a small repulsion U suffices to break the bipolarons into unbound polarons (whose properties are also strongly affected by the non-linear terms, as already shown).

Since publication of the work reported in this chapter, research carried out by Steve Johnston has used quantum Monte Carlo methods to study the nonlinear Holstein model at finite carrier concentration [70, 71]. They find that in a two-dimensional Hubbard model, Charge-Density-Wave correlations are dramatically suppressed, even for small non-linear terms. Their findings confirm our earlier remarks that non-linear terms remain important at finite carrier concentration.

2.4.4 Other types of el-ph coupling

The Holstein model is the simplest example of a $g(q)$ model, i.e. a model where the electron-phonon interaction depends only on the momentum of the phonon. Physically, such models appear when the coupling to the lattice manifests itself through a modulation of the on-site energy of the carrier. The Fröhlich model is another famous example of $g(q)$ coupling. Models of this type are found to have qualitatively similar behavior, with small polarons forming when the effective coupling increases. These small polarons always have robust clouds, with significant distortions of the lattice in their vicinity. We therefore expect that non-linear terms become important for all such models at sufficiently large linear coupling.

2.5 Concluding remarks

To summarize, we have shown that non-linear terms in the el-ph coupling *must* be included in a Holstein model if the linear coupling is large enough to predict small polaron formation, and that doing so may very significantly change the results. We also argued that these changes cannot be accounted for by a linear Holstein model with renormalized parameters. These results show that we have to (re)consider carefully how we model interactions with phonons (more generally, with any bosons) in materials where such interactions are expected to be strong, at least for models where this coupling modulates the on-site energy of the carriers.

Chapter 3

Quadratic Holstein model

In this chapter, we show that in crystals where light ions are symmetrically intercalated between heavy ions, the electron-phonon coupling for carriers located at the light sites cannot be described by a Holstein model. We introduce the double-well electron-phonon coupling model to describe the most interesting parameter regime in such systems, and study it in the single carrier limit using the momentum average approximation. For sufficiently strong coupling, a small polaron with a robust phonon cloud appears at low energies. While some of its properties are similar to those of a Holstein polaron, we highlight some crucial differences. These prove that the physics of the double-well electron-phonon coupling model cannot be reproduced with a linear Holstein model.

3.1 Introduction

We recall that in most standard electron-phonon coupling models, it is assumed that the electron-phonon coupling is *linear* in the lattice displacements. This is a natural assumption because if the displacements are small, the linear term is the most important contribution. However, the coefficient of the linear term of the Holstein-like local electron phonon coupling may vanish due to symmetries of the crystal. In such cases, the most important contribution is the *quadratic* term.

Here we introduce, motivate and study in detail a Hamiltonian describing such quadratic electron-phonon (e-ph) coupling relevant for many common crystal structures, consisting of intercalated sublattices of heavy and light atoms. We focus on the single carrier limit and the parameter regime where the carrier dynamically changes the effective lattice potential from a single-

well to a double-well; hence, we call this *the double-well e-ph coupling*. We use the momentum-average approximation [1, 12] to compute the properties of the resulting polaron with high accuracy. We find that although the polaron shares some similarities with the Holstein polaron, it also differs in important aspects. Indeed, we show that the physics of the double-well e-ph coupling model cannot be described by a renormalized linear Holstein model.

To the best of our knowledge, this is the first systematic, non-perturbative study of such a quadratic model. In the previous chapter and in [62] we studied the effect of quadratic (and higher) corrections added to a linear term. Weak, purely quadratic coupling was studied using perturbation theory in Refs. [58, 59]. Other works considered complicated non-linear lattice potentials and couplings but treated the oscillators classically, [72, 73, 61] or discussed anharmonic lattice potentials but for purely linear coupling [74, 75]. Away from the single-carrier limit, the Holstein-Hubbard model in infinite dimensions was shown to have parameter regions where the effective lattice potential has a double-well shape; [76–78] this was then used to explain ferroelectricity in some rare-earth oxides. See [79] and references therein. However, the effect of a double-well e-ph coupling on the properties of a single polaron were not explored in a fully quantum-mechanical model on a low-dimensional lattice.

This work is organized as follows: in Section 3.2 we introduce the Hamiltonian, motivate its use for relevant systems, and discuss all approximations made in deriving it. In Section 3.3 we review the theoretical means by which we study our Hamiltonian. In Section 3.4 we present our results, and in Section 3.5 we give our concluding discussion and an outlook for future work.

3.2 Model

The crystal structures of interest are illustrated in Fig. 3.1(a) for 1D, and Fig. 3.1(b) for 2D cases. The 3D crystal would have a perovskite structure but we do not discuss it explicitly because, as we show below, dimensionality

3.2. Model

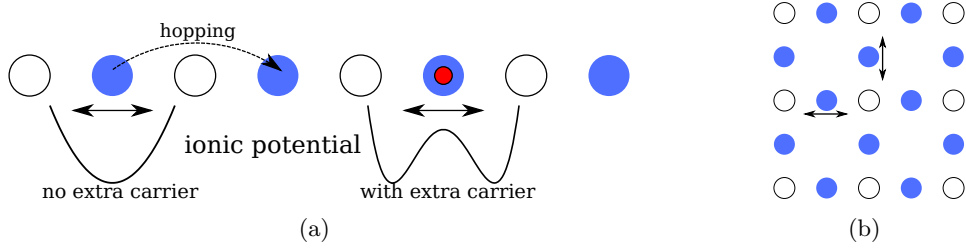


Figure 3.1: Sketch of the crystal structures discussed in this work: (a) 1D chain, and (b) 2D plane, consisting of light atoms (filled circles) intercalated between heavy atoms (empty circles). In the absence of carriers, the ionic potential of a light atom is a simple harmonic well. In the presence of a carrier, the ionic potential of the light atom hosting it remains an even function of its longitudinal displacement, so the linear e-ph coupling vanishes. In suitable conditions the effective ionic potential becomes a double well (see text for more details).

plays no strong role in determining the polaron properties.

The undoped compound is an insulator made of light atoms, shown as filled circles, intercalated between heavy ones, shown as empty circles. To zeroth order, the vibrations of the heavy atoms can be ignored while those of the light atoms are described by independent harmonic oscillators $\mathcal{H}_{\text{ph}} = \Omega \sum_i b_i^\dagger b_i$, where b_i annihilates a phonon at the i^{th} light atom. (We set the mass of the light ions $M = 1$, and also $\hbar = 1$). In reality there is weak coupling between these oscillators giving rise to a dispersive optical phonon branch. However, the dispersion can be ignored if its bandwidth is small compared to all other energy scales. We do so in the following.

Consider now the addition of a carrier. If it occupies orbitals centered on the heavy atoms, its coupling to the oscillations of the light atoms is described by breathing-mode coupling models [80, 81, 14, 82]. Here we are instead interested in the case where the carrier is located on the light atoms. Such is the situation for a CuO_2 plane as shown in Fig. 3.1(b), since the parent compound is a charge-transfer insulator[23] so that upon doping, the holes reside on the light O sites (of course, there are additional

3.2. Model

complications due to the magnetic order of the Cu spins; we ignore these degrees of freedom in the following). The carrier moves through nearest-neighbor hopping between light atoms: $\hat{T} = -t \sum_{\langle i,j \rangle} (c_i^\dagger c_j + h.c.)$, where c_i is the carrier annihilation operator at light atom i .

Given the symmetric equilibrium location of the light ion hosting the carrier between two heavy ions, it is clear that the on-site e-ph coupling cannot be linear in the displacement δx_i of that light ion: the sign of the displacement cannot matter. Thus, e-ph coupling in such a material is not described by a Holstein model. This assertion is supported by detailed modelling. For simplicity, we assume that the interactions with the neighboring heavy atoms are dominant (longer-range interactions can be easily included but lead to no qualitative changes). There are, then, two distinct contributions to the e-ph coupling:

Electrostatic coupling: The carrier changes the total charge of the light ion it resides on. If the distance between adjacent light and heavy ions is d , and if $U(x)$ is their additional Coulomb interaction due to the carrier, then the potential increases by $U(d + \delta x_i) + U(d - \delta x_i)$. This is an even function and thus has no linear (or any odd) terms in δx_i . The coefficient of the quadratic term $(\delta x_i)^2$ can be either positive or negative, depending on the charge of the carrier (electron or hole).

Hybridization: Even though charge transport is assumed to take place in a light atom band, there is always some hybridization t_{lh} allowing the carrier to hop onto an adjacent heavy ion. If Δ is the corresponding energy increase, assumed to be large, then the carrier can lower its on-site energy by $-t_{lh}^2/\Delta$ through virtual hopping to a nearby heavy ion and back. The hopping t_{lh} depends on the distance between ions; for small displacements $t_{lh}(\delta x) \approx t_{lh}(1 + \alpha\delta x)$ where α is some material-specific constant. Because the light ion is centered between two heavy ions, such contributions add to $\frac{-t_{lh}^2}{\Delta} [(1 + \alpha\delta x)^2 + (1 - \alpha\delta x)^2] = \frac{-2t_{lh}^2}{\Delta} [1 + \alpha^2(\delta x)^2]$. The potential is again even in δx . In this case, the coefficient of the quadratic term is always negative.

3.2. Model

Given that $\delta x_i \sim b_i + b_i^\dagger$, it follows that the largest (quadratic) contribution to the e-ph coupling for such a crystal has the general form:

$$\mathcal{H}_{\text{e-ph}}^{(2)} = g_2 \sum_i c_i^\dagger c_i \left(b_i + b_i^\dagger \right)^2$$

where all prefactors have been absorbed into the energy scale g_2 , and the sum is over all light ions. From the analysis above we know that g_2 may have either sign.

Physically, $\mathcal{H}_{\text{e-ph}}^{(2)}$ shows that the presence of a carrier modifies the curvature of its ion's lattice potential, and thus changes the phonon frequency at that site from Ω to $\Omega_{\text{at}} = \sqrt{\Omega^2 + 4\Omega g_2}$. If $g_2 > 0$ then $\Omega_{\text{at}} > \Omega$, making phonon creation more costly. As we show in Appendix C.3, this leads to a rather uninteresting large polaron with very weakly renormalized properties. This is why in the following we focus on the case with $g_2 < 0$.

We note at this point that what we have shown is that the linear term of a *Holstein*-like model vanishes in these symmetric cases. The same is not necessarily true for more complicated models of electron-phonon coupling. As a simple example, if we include coupling of the carrier on one site to phonons of the *neighboring* light atoms, the coupling will not be symmetric in the neighboring sites' displacements and thus retains a linear term. Such linear terms arise whether this coupling is electrostatic in nature or due to hybridization (see discussion above). These terms, however, are not included in the original, linear, Holstein model as it is intended for cases where the on-site terms are dominant. In this case, then, it is valid for us to also not include them in the non-linear Holstein model. These longer-range terms are likely to be smaller than the on-site terms we keep given that all these interactions decrease quickly with distance. In particular, we do not expect them to change the double-well physics we discuss.

For sufficiently negative g_2 , Ω_{at} vanishes or becomes imaginary, *i.e.* the lattice is unstable. This is unphysical; in reality the bare ionic potential contains higher order terms that stabilize the lattice. This means that for $g_2 < 0$ we must include anharmonic (quartic) terms in the phonon Hamil-

3.2. Model

tonian and, for consistency, also in the e-ph coupling, so that

$$\begin{aligned}\mathcal{H}_{\text{ph}} &= \Omega \sum_i b_i^\dagger b_i + \Theta \sum_i (b_i^\dagger + b_i)^4 \\ \mathcal{H}_{\text{el-ph}}^{(4)} &= \sum_{n \in \{2,4\}} g_n \sum_i c_i^\dagger c_i (b_i^\dagger + b_i)^n,\end{aligned}$$

where Θ is the scale of the anharmonic corrections. In physical situations $\Theta \ll \Omega$ and $0 < g_4 \ll |g_2|$, or the Taylor expansions would not be sensible starting points.

The anharmonic terms in \mathcal{H}_{ph} make the total Hamiltonian unwieldy, because the phonon vacuum $|0\rangle$ is no longer the undoped ground-state, and the new undoped ground state $|\tilde{0}\rangle$ has no simple analytical expression. In order to be able to proceed with an analytical approximation, we argue that these terms can be absorbed into the e-ph coupling; this is a key approximation of the model. The reasoning is as follows: At those lattice sites that do not have a carrier, the quartic terms have little effect if $\theta \ll \Omega$. This statement is verified by exact diagonalization of \mathcal{H}_{ph} . Results are shown in Fig. 3.2 where we plot the overlap $O = |\langle 0|\tilde{0}\rangle|^2$ (per site) between the undoped ground-states with and without anharmonic corrections, as well as the average number of phonons at a site of the undoped lattice. Even for unphysically large values $\Theta/\Omega \sim 1$, the overlap O remains close to 1 while $N_{\text{ph}} \ll 1$, showing that the undoped ground-state has not changed significantly in the presence of anharmonic corrections. From now we ignore these corrections at sites without an additional carrier.

However, for sites that have a carrier present, we cannot ignore the anharmonic term: As discussed, it is crucial for stabilizing the lattice. Since this term is similar to the quartic term in the e-ph coupling, they can both be grouped together, resulting in the approximate Hamiltonian for our crystal:

$$\begin{aligned}\mathcal{H} = \hat{T} + \Omega \sum_i b_i^\dagger b_i + g_2 \sum_i c_i^\dagger c_i (b_i^\dagger + b_i)^2 \\ + (g_4 + \Theta) \sum_i c_i^\dagger c_i (b_i^\dagger + b_i)^4 \quad (3.1)\end{aligned}$$

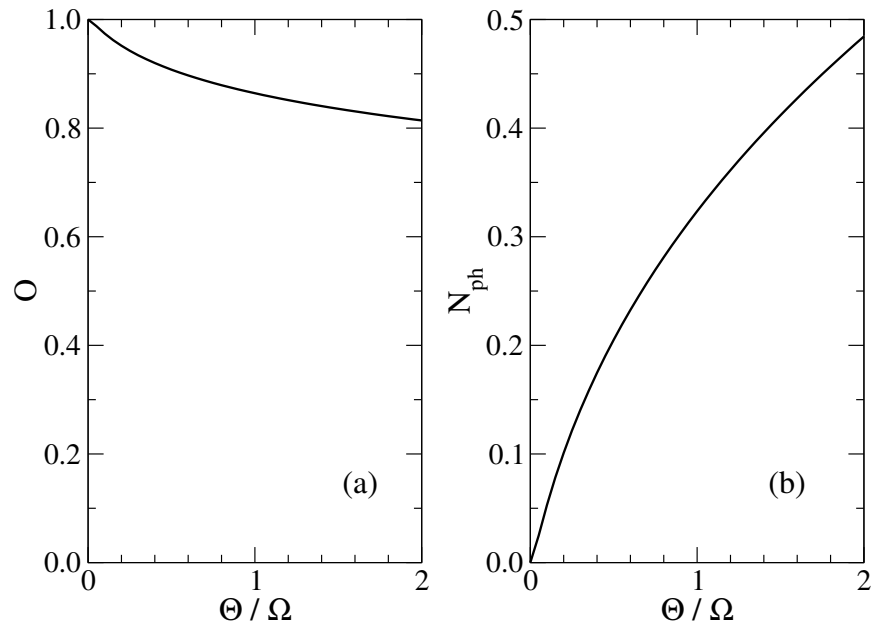


Figure 3.2: (a) Overlap between the undoped ground-states with and without anharmonic corrections, and (b) the average number of phonons per site in the undoped system, due to anharmonic corrections, as a function of θ/Ω .

3.2. Model

with an effective quartic e-ph coupling term $g_4 + \Theta$, which from now on we will simply call g_4 . This is the Hamiltonian that we investigate in this work.

Before proceeding, let us review what we are neglecting when we discard the anharmonic corrections at the unoccupied sites. Besides ignoring the change in the undoped ground state from $|0\rangle$ to $|\tilde{0}\rangle$ (which is a reasonable approximation if $\theta/\Omega \ll 1$, as discussed), we also assume that only the e-ph coupling can change the number of phonons in the system, whereas in the full model the phonon number is also changed by anharmonic corrections. This latter approximation is valid if the timescale for anharmonic phonon processes $\tau_4 \sim 1/\Theta$ is much longer than the characteristic polaron timescale $\tau_p \sim m^*/(mt)$, where m^* is the effective polaron mass.

Let us briefly summarize the basic properties of the lattice potential, which equals $V_e(\delta x) = \Omega^2(\delta x)^2/2$ for sites without an extra carrier, and $V_c(\delta x) = \Omega_{\text{at}}^2(\delta x)^2/2 + 4\Omega^2 g_4(\delta x)^4$ for sites with one carrier. If $g_2 > -\Omega/4$, the first term describes a harmonic well with frequency Ω_{at} and $V_c(\delta x)$ describes a single well centered at $\delta x = 0$. If $g_2 < -\Omega/4$, however, Ω_{at} becomes purely imaginary. In this case, $V_c(\delta x)$ becomes a double-well potential with a local maximum at $\delta x = 0$. The two wells are centered at $\pm x_{\text{eq}} = \pm \sqrt{\frac{-\Omega - 4g_2}{16\Omega g_4}}$. For $\delta x \approx \pm x_{\text{eq}}$ we obtain $V_c(\delta x) \approx V(x_{\text{eq}}) - \Omega_{\text{at}}^2(\delta x \mp x_{\text{eq}})^2$, which locally describes a harmonic well of frequency $\Omega_{\text{eff}}^2 = -2\Omega_{\text{at}}^2$. Interestingly, this is independent of g_4 , whose only role is to control the location and depth of the two wells (they are further apart and deeper for *smaller* g_4).

3.2.1 Summary of model assumptions

As in the previous chapter, we will summarize here the assumptions that went into the model.

First, quartic terms of the free-phonon part of the Hamiltonian got absorbed into the el-ph coupling. We justify this by explicitly studying the effect of quartic terms on the phonons and showing that they do not significantly change the free-phonon behaviour, especially in the physical situation of $\Theta \ll \Omega$.

Second, it is assumed that the timescale of these anharmonic processes

3.3. Formalism

is much slower than the polaronic timescale. We justify this as follows. Assuming an overall small anharmonic contribution Θ , a light polaron will certainly move on a faster timescale than $1/\Theta$. A heavy polaron, on the other hand, implies that the carrier cannot travel far from the phonon cloud; thus, anharmonic effects predominantly occur when the carrier is present, and again the effect of free-phonon anharmonic terms can be neglected.

Finally, we assume that models exist where the quadratic coupling term can be sufficiently negative. Since the hybridization term is always negative, we show here a back-of-the-envelope calculation for the Coulomb term. For our example, we assume a chain of hydrogen ions intercalated between some unspecified heavier ions with charge $+1$, and that the charge carrier is an electron. Assuming that longer range interactions are screened, the Coulomb potential experienced by the extra charge carrier is then given by

$$U(\delta x) = \frac{-e^2}{4\pi\epsilon_0} \left[\frac{1}{a + \delta x} + \frac{1}{a - \delta x} \right].$$

Here we set $a \approx 1\text{\AA}$, which is slightly larger than the length of a hydrogen molecule. Expanding the potential to second order in δx provides us with an estimate for g_2 . Assuming a phonon frequency of $\Omega = 0.5eV$, just as in the previous chapter, gives a zero-point amplitude of $A \sim 0.1\text{\AA}$ and finally leads to $g_2 \approx -0.14eV$, so the condition of $g_2 > -\Omega/4$ is satisfied. Again, parameters will be slightly different in actual materials, but not by orders of magnitude. It is thus very plausible that the double-well electron-phonon coupling is realized in some materials.

3.3 Formalism

We want to find the single particle Green's function $G(k, \omega) = \langle 0 | c_k \hat{G}(\omega) c_k^\dagger | 0 \rangle$, where $\hat{G}(\omega) = [\omega - \mathcal{H} + i\eta]^{-1}$ is the resolvent of Hamiltonian (3.1). From this, we can obtain all the polaron's ground state properties as well as its dispersion [12].

Grouping terms in the Hamiltonian according to how they affect the

3.3. Formalism

phonon number, we rewrite

$$\mathcal{H} = \mathcal{H}_0 + \mathcal{H}_p + \mathcal{H}_2 + \mathcal{H}_4 \quad (3.2)$$

with

$$\mathcal{H}_0 = \hat{T} + \Omega \sum_i b_i^\dagger b_i + g_2 + 3g_4 \quad (3.3)$$

$$\mathcal{H}_p = \sum_i n_i b_i^\dagger b_i (2g_2 + 6g_4 + 6g_4 b_i^\dagger b_i) \quad (3.4)$$

$$\mathcal{H}_2 = \sum_i n_i \left[(g_2 + 6g_4)(b_i^{\dagger,2} + b_i^2) + 4g_4(b_i^{\dagger,3} b_i + b_i^\dagger b_i^3) \right] \quad (3.5)$$

$$\mathcal{H}_4 = g_4 \sum_i n_i \left(b_i^{\dagger,4} + b_i^4 \right). \quad (3.6)$$

We note that \mathcal{H}_0 and \mathcal{H}_p conserve phonon number whereas \mathcal{H}_2 and \mathcal{H}_4 change it by ± 2 and ± 4 , respectively. The constant $g_2 + 3g_4$ in \mathcal{H}_0 is absorbed into ω in the following derivations, but plots of the spectral weight will show actual energies.

One important property of this Hamiltonian is that it preserves the phonon number parity on each site: because its terms only change the number of phonons by multiples of two, any eigenstate is a sum of basis states having only even (or only odd) number of phonons. The Hilbert space can thus be divided into an *even* and an *odd* (phonon number) sector, which can be diagonalized separately. We emphasize that this symmetry is different from the parity symmetry under a global lattice inversion $\mathbf{r} \rightarrow -\mathbf{r}$. The latter has been studied extensively for the linear Holstein model [83], where it was shown that polaron states with total momentum $K = 0, \pi$ have well defined (spatial) parity. The phonon number parity, on the other hand, corresponds to a unitary transformation $b_i^\dagger \rightarrow -b_i^\dagger$, i.e., a local inversion of the phonon coordinates. The number parity symmetry also correlates with the *local* spatial parity of the ions, since the spatial parity operator for site i can be written as $\hat{P}_i = \exp(i\pi b_i^\dagger b_i)$.

3.3.1 The even sector

We compute the Green's function via the same continued matrix fractions method[2] previously used by us to compute the Green's function of a generalized Holstein model with linear and higher-order terms[62] within the framework of the momentum average (MA) approximation. This approximation was shown to be highly accurate for models with Holstein coupling [1, 12]. The reasons for this (such as obeying exact sum rules) can be verified to hold for this model, too. To be specific, here we implement the MA⁽²⁾ flavor which allows us to also locate the continuum lying above the polaron band. Recall from the introduction that this version of MA means that the exact form of the free propagator is used for those orders of the Dyson series where there are at most 2 phonons in the system [13].

We begin our derivation by dividing the Hamiltonian into $\mathcal{H} = \mathcal{H}_0 + \mathcal{H}_1$ with $\mathcal{H}_1 = \mathcal{H}_p + \mathcal{H}_2 + \mathcal{H}_4$. Using Dyson's identity $\hat{G}(\omega) = \hat{G}_0(\omega) + \hat{G}(\omega)\mathcal{H}_1\hat{G}_0(\omega)$, where $\hat{G}_0(\omega) = [\omega - \mathcal{H}_0 + i\eta]^{-1}$, we obtain

$$G(k, \omega) = G_0(k, \omega) \left[1 + \sum_i \frac{e^{ikR_i}}{\sqrt{N}} (g_2 + 6g_4) F_1(k, \omega; i, i) + g_4 F_2(k, \omega; i, i) \right] \quad (3.7)$$

with $F_n(k, \omega; i, j) = \langle 0 | c_k \hat{G}(\omega) c_i (b_i^\dagger)^{2n-2} (b_j^\dagger)^2 | 0 \rangle$ being the generalized propagator for a system with $2n$ phonons in total, $2n - 2$ of them on site i with the other two on site j . The difference between MA⁽²⁾ and the original MA, which we also call MA⁽⁰⁾, is that for F_1 we also use its exact equation of motion (EOM),

$$\begin{aligned} F_1(k, \omega; i, j) &= G(k, \omega; j) G_0(j - i, \omega - 2\Omega) (2g_2 + 12g_4) \\ &\quad + F_1(k, \omega; j, j) G_0(j - i, \omega - 2\Omega) (4g_2 + 36g_4) \\ &\quad + 8g_4 F_2(k, \omega; j, j) G_0(j - i, \omega - 2\Omega) + \\ &\quad \sum_l G_0(l - i, \omega - 2\Omega) [F_2(k, \omega; l, j) (g_2 + 6g_4) + F_3(k, \omega; l, j) g_4]. \end{aligned} \quad (3.8)$$

3.3. Formalism

which is obtained by applying Dyson's identity again, and introducing

$$G(k, \omega; j) = \langle 0 | c_k \hat{G}(\omega) c_j^\dagger | 0 \rangle, \quad G_0(j - i, \omega) = \langle 0 | c_j \hat{G}_0(\omega) c_i^\dagger | 0 \rangle.$$

The equations of motion for the F_n propagators with $n \geq 2$ are approximated by replacing the free propagator $G_0(j - i, \omega - 2n\Omega) \rightarrow \delta_{i,j} \bar{g}_0(\omega - 2n\Omega)$, where $\bar{g}_0(\omega) = \frac{1}{N} \sum_k G_0(k, \omega)$ is the momentum averaged free propagator. At low energies this is a good approximation because $G_0(j - i, \omega - 2n\Omega)$ decays exponentially with the distance $|j - i|$ if $\omega - 2n\Omega < -2dt$ in d dimensions. This is also justified by the variational meaning of the MA approximations already discussed. Essentially, MA⁽²⁾ assumes that all phonons in the cloud are at the same site but also allows for a pair of phonons to be created at a site away from the cloud.

The resulting EOMs are different depending on whether $i = j$ or $i \neq j$. If we define $F_n^=(k, \omega; i) = F_n(k, \omega; i, i)$ and $F_n^\neq(k, \omega; i, j) = F_n(k, \omega; i, j)$ for $i \neq j$, we obtain

$$\begin{aligned} F_n^=(k, \omega; i) = & \bar{g}_0(\omega - 2n\Omega) \left[F_{n-2}^=(2n)^{\bar{4}} g_4 + F_{n-1}^= \left((g_2 + 6g_4)(2n)^{\bar{2}} + 4g_4(2n)^{\bar{3}} \right) + \right. \\ & \left. (4ng_2 + 12ng_4 + 24n^2 g_4) F_n^= + (g_2 + 6g_4 + 8ng_4) F_{n+1}^= + g_4 F_{n+2}^= \right]. \quad (3.9) \end{aligned}$$

$$\begin{aligned} F_n^\neq(k, \omega; i, j) = & \bar{g}_0(\omega - 2n\Omega) \left[g_4(2n - 2)^{\bar{4}} F_{n-2}^\neq + \right. \\ & \left((g_2 + 6g_4)(2n - 2)^{\bar{2}} + (2n - 2)^{\bar{3}} \cdot 4g_4 \right) F_{n-1}^\neq + \\ & [2(2n - 2)g_2 + 12(n - 1)g_4 + 6(2n - 2)^2 g_4] F_n^\neq + \\ & \left. [g_2 + 6g_4 + 4(2n - 2)g_4] F_{n+1}^\neq + g_4 F_{n+2}^\neq \right] \quad (3.10) \end{aligned}$$

where we use the notation $x^{\bar{n}} = x!/(x - n)!$. We also omitted the arguments from the F_n appearing on the right hand sides, as they remain unchanged.

These EOMs connect generalized Green's functions F_n with $F_{n\pm 1}$ and $F_{n\pm 2}$. We reduce this to a first order recurrence relation[62] by introducing

3.3. Formalism

vectors $W_n^- = (F_{2n}^-, F_{2n+1}^-)$ and analogously for W_n^\neq . Below, we write W_n without the index $=$ or \neq for results that apply to both W_n^- and W_n^\neq . By inserting the EOMs into the definition of W_n , we obtain a matrix EOM for the W_n ,

$$\gamma_n W_n = \alpha_n W_{n-1} + \beta_n W_{n+1}. \quad (3.11)$$

The coefficients of these matrices are read off from the EOM for the F_n . They are listed in appendix C.1.1.

Using the fact that $\lim_{n \rightarrow \infty} A_n = 0$ we can show[62] that

$$W_n = A_n W_{n-1}, \quad \text{with} \quad A_n = [\gamma_n - \beta_n A_{n+1}]^{-1} \alpha_n.$$

By introducing a suitably large cut-off N where we set $A_{N+1} = 0$, we can compute all A_n with $n \leq N$ as continued matrix fractions. Knowledge of A_1 allows us to express F_2 and F_3 in terms of F_1 and $F_0 = G$. Following a series of steps presented in appendix C.1.2, we obtain a closed equation for F_1 in terms of G , which we then finally use to compute G . The end result of these manipulations is the self energy

$$\Sigma(\omega) = \frac{(g_2 + 6g_4 + A_1^- |_{12} g_4) \tilde{g}_0(\omega) a_0^-}{1 - \tilde{g}_0(\omega) (a_1^- - a^\neq)} + g_4 A_1^- |_{11}.$$

with $\tilde{g}_0(\omega) = \bar{g}_0(\omega - 2\Omega - a^\neq)$ and the other coefficients defined in appendix C.1.2. The independence of the self-energy on momentum is the consequence of the local form of the coupling and of the non-dispersive phonons, similar to the MA results for the Holstein model [13]. Momentum-dependence would be acquired in a higher flavor of MA, but is likely to be weak. Finally, the Green's function is:

$$G(k, \omega) = \frac{1}{\omega - \epsilon_k - \Sigma(\omega) + i\eta}. \quad (3.12)$$

One can now use the matrices A_n to generate the generalized propagators F_n , which allow one to reconstruct the entire polaron wavefunction (within this variational space) [84]. For the quantities of interest here, however, the single-particle Green's function suffices.

3.3.2 The odd sector

Here we calculate the Green's function for a state that already has a phonon in the system. Since the phonon number can only change by 2 or 4, this single phonon can never be moved to another site, so it is natural to compute the Green's function in real space. The most general such real space Green's function is:

$$G_{ijl}(\omega) = \langle 0 | b_l c_j \hat{G}(\omega) c_i^\dagger b_l^\dagger | 0 \rangle.$$

Applying the Dyson identity leads to the EOM

$$G_{ijl}(\omega) = G_0(j - i, \omega - \Omega) + \sum_{i'} G_0(i' - i, \omega - \Omega) \langle 0 | b_l c_j \hat{G}(\omega) \mathcal{H}_1 c_{i'}^\dagger b_l^\dagger | 0 \rangle.$$

We then split the sum over all lattice sites into a term $i' = l$ where the electron is on the same site as the extra phonon, and a sum over all the other sites. The subsequent steps are very similar to those for the even-sector Green's function. We summarize them in Appendix C.2, where we also discuss how various propagators that enforce translational symmetry – *i.e.* propagators defined in momentum space – can be obtained from these real-space Green's functions.

The end result for the real-space Green's functions is $G_{ijl}(\omega) = G_0(j - i, \tilde{\omega}) + G_0(l - i, \tilde{\omega}) G_0(j - l, \tilde{\omega}) (a_o^- - a_o^\#) [1 - \bar{g}_0(\tilde{\omega}) (a_o^- - a_o^\#)]^{-1}$ where $\tilde{\omega} = \omega - a_o^\# - \Omega$. The coefficients a_o^- and $a_o^\#$ are listed in appendix C.2.

3.4 Results

3.4.1 Atomic limit: $t = 0$

We begin our analysis with the atomic limit since it is a good starting point for understanding the properties of the small polaron, which is the more interesting regime. However, we note an important distinction between the Holstein model and our double-well model. In the former, the atomic limit is the infinite-coupling limit. In the latter, g_4 sets an additional energy scale.

Thus, the atomic limit is not the same as the strong coupling limit; the latter also requires that $g_4/|g_2|$ be small.

Before doing any computations, we can describe some general features of the spectrum. As already discussed, the phonon component of the wavefunctions has either even or odd phonon number parity. Since this is due to the spatial symmetry in the local ionic displacement, in any eigenstate the ion is equally likely to be found in either well. As usual, the ground state has *even* symmetry since it has no nodes in its wavefunction. Subsequent eigenstates always have one more node than the preceding eigenstate, so states with even and odd parity alternate. The exception is the limit of infinite well separation, $g_4/|g_2| \rightarrow 0^+$, where the $2n^{\text{th}}$ and $2n + 1^{\text{st}}$ eigenstates become degenerate. The system can then spontaneously break parity to have the ion definitely located in the left or in the right well, like in a ferroelectric. For a finite g_4 this is not possible in the single carrier limit, but it can be achieved at finite carrier concentration through spontaneous symmetry breaking.

As discussed, our results are obtained with MA. In the atomic limit MA is exact[1] because for $t = 0$ the free propagator is diagonal in real-space so the terms ignored by MA vanish. Thus, MA results must be identical here to those obtained by other exact means. To check our implementation of MA, we used exact diagonalization (ED) with up to a few thousand phonons; this suffices for an accurate computation of the first few eigenstates. ED and MA results agree, as required.

Figure 3.3 shows the ground-state quasiparticle weight Z (the overlap between the polaron ground-state and the non-interacting carrier ground-state), and the ground-state average number of phonons in the cloud, N_{ph} , as a function of $g_2 < 0$, for various values of g_4 . Z has an interesting behavior. At $g_2 = 0$ it is slightly below 1 because of the quartic terms. As $|g_2|$ is increased, Z first rises towards a value close to 1 and then sharply drops. This turnaround is caused by the terms that involve both g_2 and g_4 , *i.e.* $(2g_2 + 6g_4) \sum_i n_i b_i^\dagger b_i$ from \mathcal{H}_p and $(g_2 + 6g_4) \sum_i n_i (b_i^{\dagger,2} + b_i^2)$ from \mathcal{H}_2 . Starting from $g_2 = 0$ and making it increasingly more negative will at first decrease these coefficients, thereby renormalizing the ground state less. For even

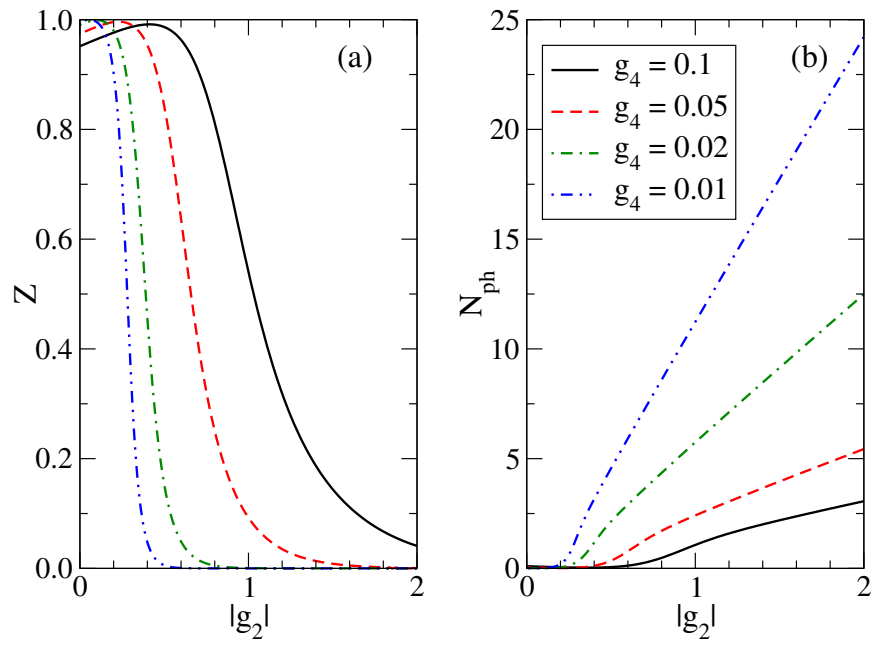


Figure 3.3: Polaron ground-state properties in the atomic limit, for several values of the g_4 : a) quasiparticle weight, and b) average number of phonons in the phonon cloud. Other parameters are $\Omega = 0.5, t = 0$.

3.4. Results

more negative g_2 , however, Z decreases sharply as the absolute value of these coefficients increases; this is paralleled by a strong increase in N_{ph} . Based on this argument, the peak in Z should occur for $-6g_4 < g_2 < -3g_4$, which is indeed the case. The strong-coupling limit of a small polaron (corresponding to small Z , large N_{ph} values) is therefore reached either by increasing $|g_2|$ or by lowering g_4 .

While this allows us to conclude that in the atomic limit the crossover into the small polaron regime occurs at $\frac{g_2}{3g_4} \approx -1.5$, it also illustrates the difficulty in defining an effective coupling for this model. For the Holstein model, the dimensionless effective coupling λ is the ratio between the ground-state energies in the atomic limit and in the free electron limit; the crossover to the small polaron regime occurs at $\lambda \sim 1$. For the double-well model the introduction of an effective coupling is not as straightforward, because the atomic limit has vastly different properties depending on the ratio g_2/g_4 , so comparing the energy in this limit to that of a free electron is not sufficient. (Moreover, there is no analytic expression for the ground state energy of the double well potential). For these reasons, we continue to use the *bare* coupling parameters g_2 and g_4 to characterize our model.

For strong coupling, we can accurately estimate the ground state energy by using the barrier depth and effective harmonic frequency of the double-well potential, $E_{0,\text{sc}} = V_c(x_{\text{eq}}) + \Omega_{\text{eff}}/2$. Fig. 3.4 shows the relative error of this estimate, which indeed decreases as parameters move deeper into the small polaron regime. Since here the tunnelling between the two wells also becomes increasingly smaller, one may think that we can describe this regime accurately by assuming that the carrier becomes localized in one of the wells (thus breaking parity), *i.e.* that we can approximate the full lattice potential as being a single harmonic well centered at either x_{eq} or $-x_{\text{eq}}$. Of course, the latter situation can be modelled with a linear Holstein model.

It turns out that this is not the case. In the standard Holstein model, the charge carrier cannot change the curvature of the lattice potential and thus cannot account for the difference between Ω and Ω_{eff} . To account for the change in the curvature of the well, one would have to consider at least a Holstein model with both linear and quadratic e-ph coupling terms.

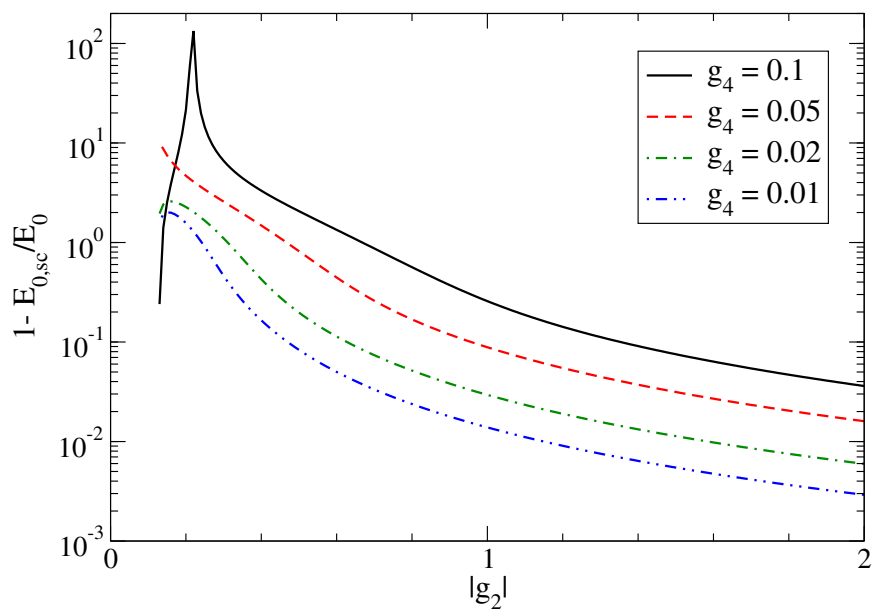


Figure 3.4: Relative error in the ground state energy when computed in the semiclassical approximation (see text for details). The coupling $g_2 < -\Omega/4$ is restricted to values for which there is a double-well potential. Other parameters are like in Fig. 3.3.

Although it is possible to find effective parameters $g_{1,\text{eff}}$, $g_{2,\text{eff}}$ and Ω_{eff} so that the resulting lattice potential in the presence of the carrier has the same location and curvature as one of the wells of the double-well potential, the corresponding quasi-particle weight Z_{eff} severely underestimates Z . This is because the single well approximation severely overestimates the lattice potential at $x = 0$, thereby reducing the overlap between the ground state of the shifted well and that of the original well. We conclude that the double-well coupling cannot be accurately described by a (renormalized) Holstein coupling even in this simplest limit.

3.4.2 Finite hopping

We focus on results from the *even* sector because it describes states accessible by injecting the carrier in the undoped ground-state. The odd sector is accessed only if the carrier is injected into an excited state with an odd number of phonons present in the undoped system; we briefly discuss this case at the end of the section.

We begin by plotting the ground-state values of Z and N_{ph} , for 1D and 2D lattices, in Figs. 3.5 and 3.6 respectively. Since the MA self-energy is local, the effective polaron mass $m^* = m/Z$, where m is the free carrier mass; we therefore do not plot m^* separately. Apart from $t = 1$, the parameters are like in Fig. 3.3. Note that the kinks in the N_{ph} curves for $g_4 = 0.02$ are not physical; they arise from numerical difficulties in resolving the precise location of the ground state peak when $Z \rightarrow 0$.

Qualitatively, the polaron properties show the same dependence on g_2 as in the atomic limit, but the shape and location of the turnarounds is slightly modified: As one would expect, the presence of finite hopping counteracts the formation of a robust polaron cloud and increases the quasi-particle weight Z for any given g_2 and g_4 when compared to the atomic limit.

The results in one and two dimensions are strikingly similar. The 2D Z is slightly larger than the 1D Z , and N_{ph} in 2D is slightly lower than in 1D. This is expected because in higher dimensions, the polaron formation energy is competing against a larger carrier kinetic energy. These results

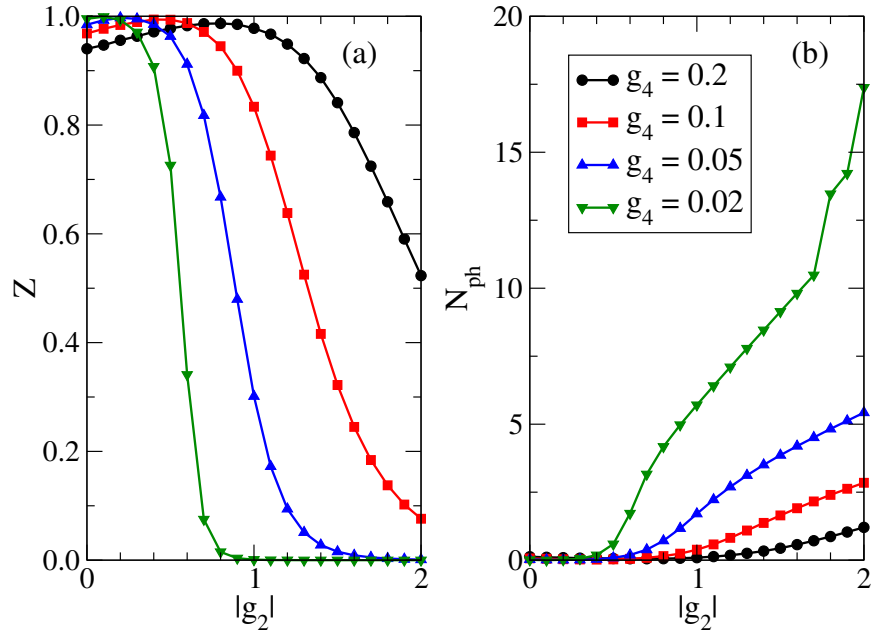


Figure 3.5: (color online) Polaron ground-state properties in one dimension for various values of the quartic coupling term g_4 as a function of the quadratic coupling g_2 : a) quasiparticle weight, and b) average number of phonons in the phonon cloud. Other parameters are $t = 1$, $\Omega = 0.5t$.

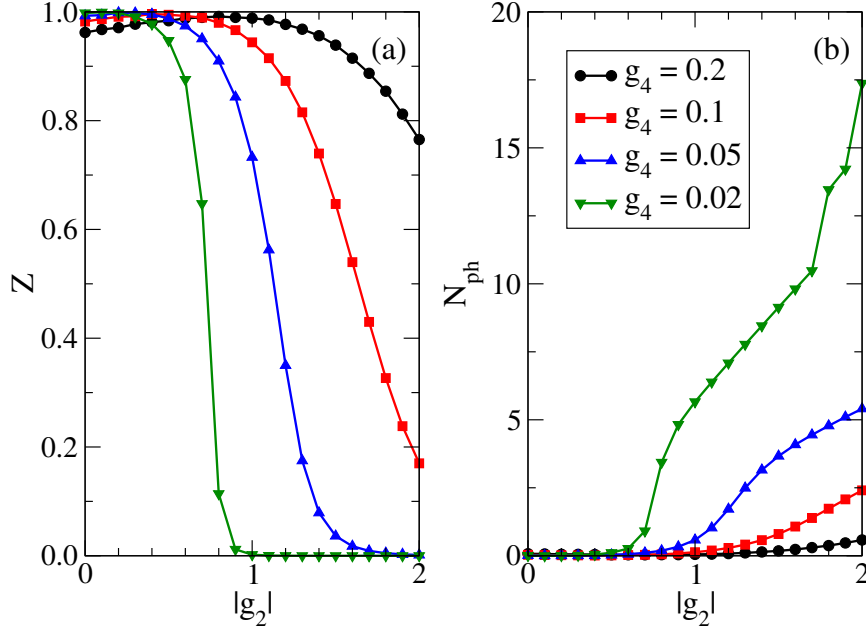


Figure 3.6: Polaron ground-state properties in two dimensions for various values of the quartic coupling term g_4 as a function of the quadratic coupling g_2 : a) quasiparticle weight, and b) average number of phonons in the phonon cloud. Other parameters are $t = 1$, $\Omega = 0.5t$.

suggest that dimensionality is not playing a key role for the double-well model, similar to the situation for the Holstein model. This is why we did not consider 3D systems explicitly.

We now move on to discuss the evolution of the spectral weight $A(k, \omega) = -\frac{1}{\pi} \text{Im}G(k, \omega)$ with increasing $|g_2|$, at a fixed value of g_4 . This is shown in Fig. 3.7 for 1D, and in Fig. 3.8 for 2D. Because the evolution is again qualitatively similar in the two cases, we analyze in more detail the 1D results. Here, at small quadratic coupling $g_2 = -0.5$, we observe the appearance of a polaron band below a continuum of states. This continuum begins at $E_0 + 2\Omega$, and consists of excited states comprising the polaron plus two phonons far away from it. (In our MA⁽²⁾ approximation, the continuum actually begins at $E_0^{\text{MA}^{(0)}} + 2\Omega$, not at $E_0^{\text{MA}^{(2)}} + 2\Omega$, for reasons detailed in Ref. [13]).

3.4. Results

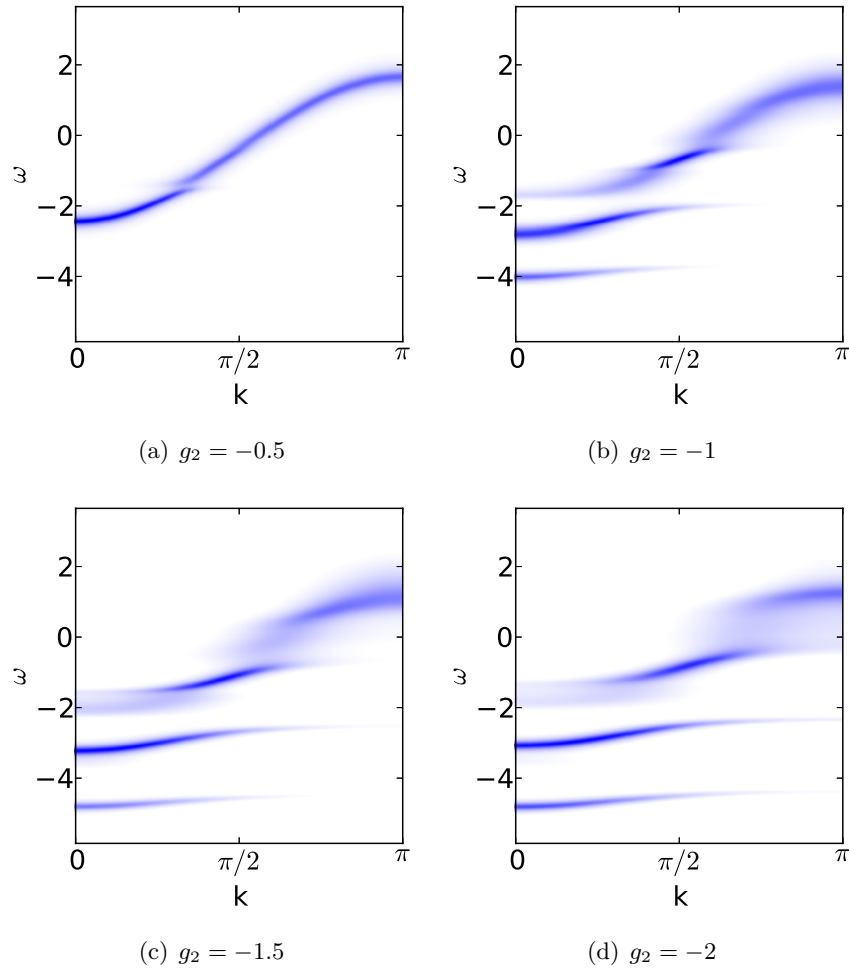
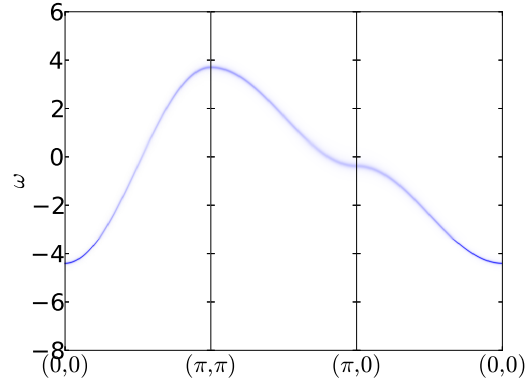
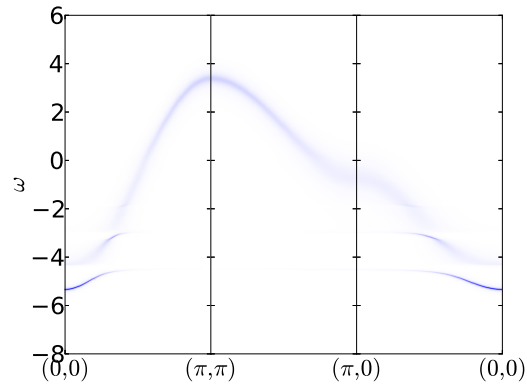


Figure 3.7: $A(k, \omega)$ in 1D, for $g_4 = 0.05$, $\Omega = 0.5$ and $t = 1$, for various values of g_2 .

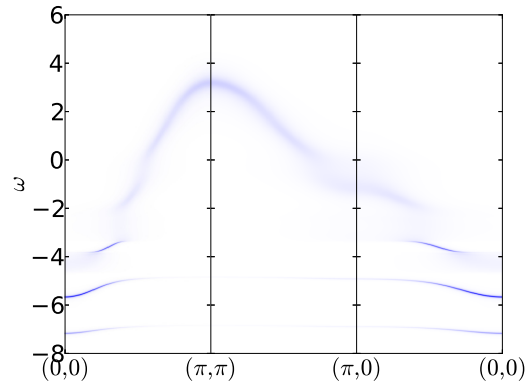
3.4. Results



(a) $g_2 = -0.5$



(b) $g_2 = -1$



(c) $g_2 = -1.5$

Figure 3.8: $A(k, \omega)$ in 2D, for $g_4 = 0.05$, $\Omega = 0.5$ and $t = 1$, for various values of g_2 . 71

3.4. Results

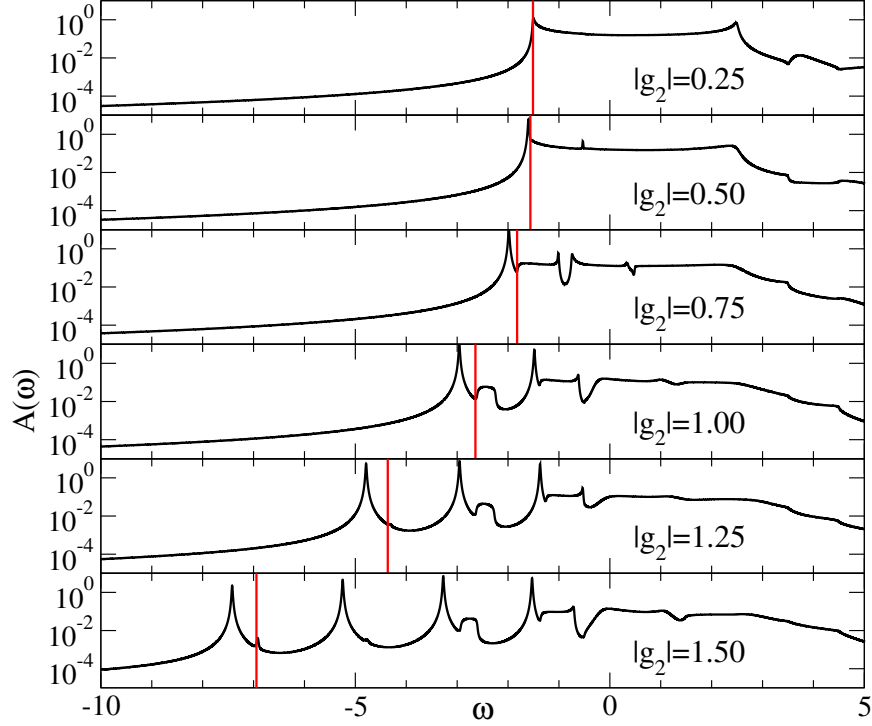


Figure 3.9: Real-space diagonal spectral function $A_{iii}(\omega)$ at $g_4 = 0.05$ for various values of (negative) g_2 in one dimension and for $\Omega = 0.5$. The y -axis has a logarithmic scale. The vertical bars indicate the position of $E_0^{\text{even}} + \Omega$.

Note that due to the parity-preserving nature of the Hamiltonian there is no analog of the polaron+one-phonon continuum starting at $E_0 + \Omega$, which is observed in all linear coupling models. Trying to mimic the results of the double-well coupling with a linear model will, therefore, lead to a wrong assignment for the value of Ω .

At small $|g_2|$, the polaron band flattens out just below the polaron+two-phonon continuum. With increasing $|g_2|$, its bandwidth decreases as the polaron becomes heavier, and additional bound states appear below the continuum. This is similar to the evolution of the spectrum of a Holstein polaron when moving towards stronger effective coupling [12]. However, as already discussed, this does not mean that the two Hamiltonians can be mapped onto one another.

For completeness, let us also discuss some of the features of the odd sector. In particular, we focus on the local Green's function $G_{iii}(\omega)$, which can be written as

$$G_{iii}(\omega) = \bar{g}_0(\tilde{\omega}) + \frac{\bar{g}_0(\tilde{\omega})^2(a^{\bar{}} - a^{\neq})}{1 - \bar{g}_0(\tilde{\omega})(a^{\bar{}} - a^{\neq})}$$

with $\tilde{\omega} = \omega - \Omega - a^{\neq}$. One can verify that a^{\neq} equals the MA⁽⁰⁾ self-energy for the *even* sector, up to a shift by Ω of its frequency. The equation for $G_{iii}(\omega)$ then shows that the odd sector spectral function comprises two parts: (i) the first term is just the momentum-averaged spectral function of the even-sector, shifted in energy by Ω due to the presence of the extra phonon. One can think of these as states where the even-sector polaron does not interact with the extra phonon. This contribution therefore has weight starting from $E_0 + \Omega$; (ii) the second part describes interactions between the polaron and the extra phonon. An interesting question is whether these can lead to a bound state, *i.e.* to a new polaron with odd numbers of phonons in its cloud.

This question is answered in Fig. 3.9 where we plot $A_{iii}(\omega) = -\frac{1}{\pi}\text{Im}G_{iii}(\omega)$ for different values of $|g_2|$ and $g_4 = 0.05$, $\Omega = 0.5$, $t = 1$, in one dimension. The vertical bars indicate the position of $E_0 + \Omega$, where indeed a continuum begins, as expected from the previous discussion. At sufficiently strong coupling $|g_2|$ we find a discrete bound state below that continuum, showing that the polaron can bind the extra phonon. In fact, it is more proper to say that the extra phonon (which is localized somewhere on the lattice) binds the polaron to itself and therefore localizes it. One can think of this as an example of “self-trapping”, except here there is an external trapping agent in the form of the extra phonon.

One might wonder whether this localized bound state in the odd sector could ever be at an energy below the polaron ground-state energy E_0 of the even sector, *i.e.* become the true ground-state. This is not the case; as explained above, in the atomic limit the ionic states alternate between even and odd symmetry. Introducing a finite hopping allows the polaron to further lower its energy by delocalizing, but this is only possible in the even sector. Thus, we always expect the even-sector polaron to have an energy

below that of this localized state.

As stated before, the two subspaces with even and odd phonon number are never mixed, at least at zero temperature. At finite temperature, the extra charge is inserted not into the phonon vacuum but into a mixed state containing a number of thermally excited phonons. We therefore expect the resulting spectral function to show features of both the even and odd sectors. To be more precise, some spectral weight should be shifted from the even-sector spectral weight to the odd-sector spectral weight as T increases and there is a higher probability to find one or more thermal phonons in the undoped state. We plan to study the temperature depend properties of this double-well coupling elsewhere.

3.5 Summary and discussions

Here we introduced and motivated a model for purely quadratic e-ph coupling, relevant for certain types of intercalated lattices, wherein the carrier dynamically changes the on-site lattice potential from a single well into a double well potential. All the approximations made in deriving this model were analyzed. In particular, we argued that ignoring the anharmonic lattice terms at the sites not hosting the carrier should be a good approximation. However, a more in-depth numerical analysis might be needed to further validate this assumption.

We used the momentum average approximation to obtain the model's ground state properties and its spectral function in the single polaron limit, in one and two dimensions. We found that for sufficiently strong quadratic coupling a small polaron forms. Although the polaron behaves somewhat similarly to the polaron of the linear Holstein model, the double-well model cannot be mapped onto an effective linear model: apart from the difference in the location of the continuum in the even sector, the double-well model also has an odd sector that should be visible at finite T , and which is entirely absent in the Holstein model. This is due to the double-well potential model's invariance to local inversions of the ionic coordinate; this symmetry is not found in the Holstein model. The polaron in this odd sector is also

qualitatively different from the Holstein polaron, in that it is localized near the additional phonon present in the system when the carrier is injected. Of course, if the assumption of an Einstein mode is relaxed, then the phonon acquires a finite speed and this polaron would become delocalized, as expected for a system invariant to translations. However, this would still be qualitatively different than a regular polaronic solution because this polaron's dispersion would be primarily controlled by the phonon bandwidth, not the carrier hopping.

Our results suggest that researchers interpreting their measurements from, *e.g.*, angular-resolved photoemission spectroscopy, must carefully consider the nature of their system's e-ph coupling: if they assume linear coupling where the lattice symmetry calls for a quadratic one, the parameters extracted from fitting to such models will have wrong values.

While we have laid here the basis for a thorough investigation of the properties of the double-well e-ph coupling model, much work remains to be done. We believe that adjusting already existing numerical schemes such as diagrammatic Monte Carlo to this model is straightforward and look forward to a comparison of numerically exact results with our MA results. In addition, there are certain ranges of parameters for which MA is not well-suited, such as the adiabatic limit $\Omega \rightarrow 0$ at weak coupling, or systems with finite carrier densities. We anticipate that these regimes will be explored with a range of numerical and analytical tools, especially the finite carrier regime which should be relevant for modelling ferroelectric materials.

We plan to extend our study of the double-well e-ph coupling beyond the single-polaron limit. We deem especially interesting the parameter range where the lattice potential remains a single well if only one carrier is present, but changes into a double well when a second charge is added. In this case, we anticipate the appearance of a strongly bound bipolaron while the single polarons are relatively light. Such states are not possible in the Holstein model.

Finally, extending our MA treatment to finite temperature should yield interesting insights into the interplay between the two symmetry sectors revealed by the spectral weight.

Chapter 4

Bipolarons in the quadratic Holstein model

In this chapter, we use the Momentum Average approximation (MA) to study the ground-state properties of strongly bound bipolarons in the double-well electron-phonon (el-ph) coupling model, whose single polaron solution was discussed in the previous chapter. We show that this model predicts the existence of strongly bound yet lightweight bipolarons in some regions of the parameter space. This provides a novel mechanism for the appearance of such bipolarons, in addition to long-range el-ph coupling and special lattice geometries.

4.1 Introduction

As pointed out in the previous chapters, when a charge carrier becomes dressed by a cloud of phonons, the quasi-particle that forms – the polaron – may have quite different properties from the free particle, such as a larger effective mass and renormalized interactions with other particles. One particularly interesting effect of the latter is the formation of bipolarons, where an effective attraction mediated by exchange of phonons binds the carriers together. If the binding is strong enough, the two phonon clouds merge into one, resulting in a so-called S0 bipolaron. Weaker binding, where each polaron maintains its cloud and the binding is mediated by virtual visits to the other carrier’s cloud, is also possible and results in a S1 bipolaron [67, 68].

The existence of bipolarons is interesting for many reasons. For instance, it has been suggested that Bose-Einstein condensation of bipolarons

might be responsible for superconductivity in some high- T_c materials. For an overview, see [85]. For this to occur, the bipolaron must be strongly bound so it can survive up to high temperatures. However, such strong binding generally requires strong electron-phonon coupling. In most simple models of el-ph coupling such as the Holstein model,[11] this also results in a large effective mass of the bipolaron[67, 68] which severely reduces its mobility and makes it likely to become localized by even small amounts of disorder.

For this reason, much of the theoretical work on bipolarons is focused on finding models and parameter regimes for which the bipolaron is strongly bound yet relatively light. So far, successful mechanisms are based either on longer-range electron-phonon interactions[86–88, 69] or on special lattice geometries such as one-dimensional ladders or triangular lattices [89].

Here we show that the recently proposed (short-range) double-well el-ph coupling model[90] also predicts the existence of strongly bound bipolarons with relatively low effective mass in certain regions of the parameter space, thus revealing another possible mechanism for their appearance. Our study uses the Momentum Average (MA) approximation,[1, 12, 62, 90] which we validate with exact diagonalization in an enlarged variational space. Since in the single-particle case the dimensionality of the underlying lattice had little qualitative impact, we focus here on the one-dimensional case.

This work is organized as follows. In Section 4.2 we introduce the Hamiltonian for the double-well model and in Section 4.3 we discuss the methods we use to solve it. In Section 4.4 we present results for the bipolaron binding energy and effective mass, and in Section 4.5 we summarize our conclusions and an outlook for future work.

4.2 Model

The double-well el-ph coupling model was introduced in the previous chapter, where its single polaron was studied. For ease of reference, we repeat some of its motivation and introduction here.

The model is relevant for crystals whose structure is such that a sublatt-

tice of light ions is symmetrically intercalated with one of much heavier ions; the latter are assumed to be immobile. Moreover, charge transport occurs on the sublattice of the light ions. An example is the one-dimensional intercalated chain shown in Fig. 4.1(a). Another example is a two-dimensional CuO layer, sketched in Fig. 4.1(b), where the doping holes move on the light oxygen ions placed in between the heavy copper ions. In such structures, because in equilibrium each light ion is symmetrically placed between two immobile heavy ions, the potential felt by a carrier located on a light ion must be an even function of that ion's longitudinal displacement from equilibrium, i.e. the first derivative of the local potential must vanish. As a result, the linear electron-phonon coupling is zero by symmetry, and one needs to consider the quadratic coupling. This is what the double-well el-ph coupling model does.

Starting from the single-polaron Hamiltonian describing double-well el-ph coupling, introduced in Ref. [90], we add the appropriate terms for the many-electron problem to obtain

$$\mathcal{H} = \hat{T} + \Omega \sum_i b_i^\dagger b_i + U \sum_i \hat{n}_{i\uparrow} \hat{n}_{i\downarrow} + g_2 \sum_{i\sigma} c_{i\sigma}^\dagger c_{i\sigma} (b_i^\dagger + b_i)^2 + \sum_i g_4^{(n_i)} (b_i^\dagger + b_i)^4. \quad (4.1)$$

Here, $c_{i\sigma}$ and b_i are annihilation operators for a spin- σ carrier at site i and a phonon at site i , respectively. \hat{T} describes hopping of free carriers on the sublattice of light ions in an intercalated lattice like that sketched in Fig. 4.1. For simplicity, we consider nearest-neighbor hopping only, $\hat{T} = -t \sum_{\langle i,j \rangle, \sigma} c_{i\sigma}^\dagger c_{j\sigma} + h.c.$, although our method can also treat longer-range finite hopping [2]. The next two terms describe a single branch of dispersionless optical phonons with energy Ω , and the Hubbard on-site Coulomb repulsion with strength U . The last two terms describe the el-ph coupling in the double-well model. As mentioned, in lattices like that sketched in Fig. 4.1, the coupling depends only on even powers of the light-ion displacement $\delta \hat{x}_i \propto b_i^\dagger + b_i$ (the heavy ions are assumed to be immobile). As a result,

the lowest order el-ph coupling is the quadratic term whose characteristic energy g_2 can have either sign, depending on modeling details. As discussed at length in the previous chapter, the interesting physics occurs when $g_2 < 0$ so that the el-ph coupling “softens” the lattice potential. For sufficiently negative g_2 this renders the lattice locally unstable in the harmonic approximation and requires the inclusion of quartic terms in the lattice potential. For consistency, one should then also include quartic terms in the el-ph coupling. Under reasonable assumptions the quartic lattice terms can be combined with the quartic el-ph coupling term on sites hosting a carrier and ignored on all other sites. Because the resulting quartic term contains contributions from both the lattice potential and from the el-ph interaction, it should not be assumed to be linear in the carrier number, unlike the quadratic term which arises purely from el-ph coupling. Instead, we use the general form

$$g_4^{(n_i)} = g_4 \cdot \begin{cases} 0, & \text{if } n_i = 0 \\ 1, & \text{if } n_i = 1 \\ \alpha, & \text{if } n_i = 2 \end{cases}$$

where $n_i = \sum_{\sigma} c_{i\sigma}^{\dagger} c_{i\sigma}$ is the number of carriers on site i , and α is a constant between 1 and 2. Setting $\alpha = 2$ assumes that quartic lattice effects are negligible compared to the quartic el-ph terms, whereas $\alpha = 1$ is the opposite extreme. For the remainder of this article we set $\alpha = 1$, so that $g_4^{(1)} = g_4^{(2)} = g_4$. This case leads to stronger coupling, since a lower g_4 results in deeper wells that are further apart,[90] and thus represents the parameter regime we are interested in. Physically, this describes the situation where the quartic lattice terms are much larger than the quartic el-ph coupling; however they are still negligible compared to the quadratic lattice terms and therefore can be ignored at sites without a carrier.

4.2.1 Summary of model assumptions

In addition to the assumptions that went into the quadratic Holstein model from the previous chapter, our assumptions are as follows:

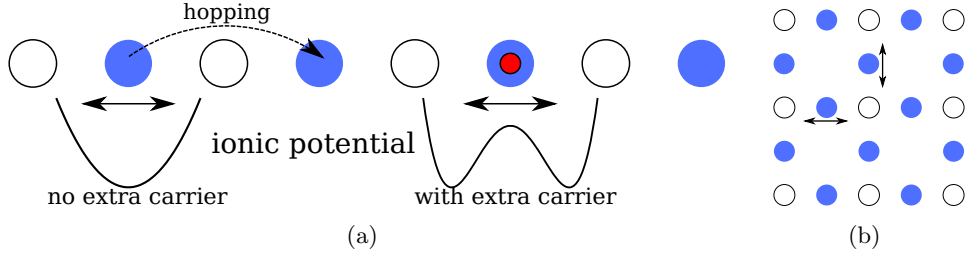


Figure 4.1: Sketch of the crystal structures discussed in this work: (a) 1D chain, and (b) 2D plane, consisting of light atoms (filled circles) intercalated between heavy atoms (empty circles). In the absence of carriers, the ionic potential of a light atom is a simple harmonic well. In the presence of a carrier, the ionic potential of the light atom hosting it remains an even function of its longitudinal displacement, so the linear e-ph coupling vanishes. In suitable conditions the effective ionic potential becomes a double well. (Reproduced from the previous chapter)

First, the Coulomb interaction between carriers is on-site only. This is a valid approximation in the presence of reasonable screening, since in the intercalated lattices we consider, the charge-carrying ions are separated by a large distance, with another ion in between.

Second, we carry out our calculations for the strongest coupling case for the quartic coupling term, which is assumed to contain contributions from both the coupling and the free-phonon part. Using a different case will change the results only quantitatively, not qualitatively.

4.3 Formalism

We compute the bipolaron binding energy and effective mass using the momentum average (MA) approximation [1, 12, 62, 90]. Since we are interested in strongly-bound bipolarons which have a large probability of having both carriers on the same site, the version of MA used here is the variational approximation that discounts states where the two carriers occupy different sites. This results in an analytic expression of the two-particle Green's function which is used to efficiently explore the whole parameter space. The

accuracy of this flavor of MA is verified by performing exact diagonalization in a much larger variational subspace (details are provided below). In the regime of interest the agreement is very favorable, showing that the effort required to perform the analytical calculation for a flavor of MA describing a bigger variational space is not warranted.

4.3.1 Momentum average approximation

We define states with both carriers at the same site, $|i\rangle = c_{i\uparrow}^\dagger c_{i\downarrow}^\dagger |0\rangle$, and states of given total momentum \mathbf{k} with both carriers at the same site,

$$|\mathbf{k}\rangle = \frac{1}{\sqrt{N}} \sum_i e^{i\mathbf{k}\cdot\mathbf{r}_i} |i\rangle.$$

The bipolaron dispersion $E_{\text{bp}}(\mathbf{k})$ is obtained from the lowest energy pole of the two-particle Green's function

$$G(\mathbf{k}, \omega) = \langle \mathbf{k} | [\omega - \mathcal{H} + i\eta]^{-1} | \mathbf{k} \rangle,$$

where $\eta \rightarrow 0^+$ is a small convergence factor. The effective bipolaron mass is $1/m_{\text{bp}} = \partial^2 E_{\text{bp}} / \partial k^2 |_{k=0}$. Throughout this work we set $\hbar = 1, a = 1$.

We split the Hamiltonian into $\mathcal{H} = \mathcal{H}_0 + \mathcal{H}_1$ with $\mathcal{H}_0 = \hat{T} + \Omega \sum_i b_i^\dagger b_i$ describing the free system and \mathcal{H}_1 containing the interaction terms. We apply Dyson's identity $\hat{G}(\omega) = \hat{G}_0(\omega) + \hat{G}(\omega) \mathcal{H}_1 \hat{G}_0(\omega)$ where

$$\hat{G}_0(\omega) = [\omega - \mathcal{H}_0 + i\eta]^{-1}$$

is the resolvent of \mathcal{H}_0 and we also define

$$G_0(\mathbf{k}, \omega) = \langle \mathbf{k} | \hat{G}_0(\omega) | \mathbf{k} \rangle = \frac{1}{N} \sum_{\mathbf{q}} \frac{1}{\omega + i\eta - \epsilon(\mathbf{k} - \mathbf{q}) - \epsilon(\mathbf{q})}$$

as a non-interacting two-particle propagator, where $\epsilon(\mathbf{k})$ is the free carrier dispersion. $N \rightarrow \infty$ is the number of light-ion sites of the lattice. In 1D, $G_0(\mathbf{k}, \omega)$ equals the momentum-averaged *single-particle* free propagator in one dimension for an effective hopping integral $2t \cos(k/2)$, for which an

analytic expression is known [91]. In higher dimensions, such propagators can be calculated as discussed in Ref. [92].

As mentioned, in a variational sense the MA used here amounts to neglecting all states where the carriers are not on the same site. This approximation is justified for the description of the strongly bound on-site (S0) bipolaron, which is expected to have most of its weight in the sector where both carriers are on the same site. Another way to look at this is that the bipolaron ground-state energy in the strongly-bound case must be well below the non-interacting two-particle continuum, and the free two-particle propagator will have vanishingly small off-diagonal matrix elements at such energies. Ignoring them, the equation of motion becomes $G(\mathbf{k}, \omega) \approx G_0(\mathbf{k}, \omega) + \langle \mathbf{k} | \hat{G}(\omega) \mathcal{H}_1 | \mathbf{k} \rangle G_0(\mathbf{k}, \omega)$, and thus:

$$G(\mathbf{k}, \omega) = G_0(\mathbf{k}, \omega) \left(1 + \sum_i \frac{e^{ikR_i}}{\sqrt{N}} \left[(g_2 + 6g_4) F_1(\mathbf{k}, \omega, i) + g_4 F_2(\mathbf{k}, \omega, i) + U F_0(\mathbf{k}, \omega, i) \right] \right).$$

where $F_n(\mathbf{k}, \omega, i) = \langle \mathbf{k} | \hat{G}(\omega) b_i^{\dagger, 2n} | i \rangle$ is a generalized two-particle propagator. Equations of motion for the F_n propagators are obtained in the same way, and read:

$$\begin{aligned} F_n(\mathbf{k}, \omega, i) = & \bar{g}_0(\omega - 2n\Omega) \left[g_4 (2n)^{\bar{4}} F_{n-2}(\mathbf{k}, \omega, i) \right. \\ & + ((2g_2 + 6g_4)(2n)^{\bar{2}} + 4g_4(2n)^{\bar{3}}) F_{n-1}(\mathbf{k}, \omega, i) \\ & + (8ng_2 + 12ng_4 + 24n^2g_4 + U) F_n(\mathbf{k}, \omega, i) \\ & \left. + (2g_2 + 6g_4 + 8ng_4) F_{n+1}(\mathbf{k}, \omega, i) + g_4 F_{n+2}(\mathbf{k}, \omega, i) \right]. \quad (4.2) \end{aligned}$$

where we use the shorthand notation $x^{\bar{n}} = x!/(x-n)!$ and have introduced

4.3. Formalism

the *momentum-averaged* free two-carrier propagator,

$$\begin{aligned}\bar{g}_0(\omega) &:= \langle i | \hat{G}_0(\omega) | i \rangle = \frac{1}{N} \sum_{\mathbf{k}} G_0(\mathbf{k}, \omega) \\ &= \frac{1}{N^2} \sum_{\mathbf{k}, \mathbf{q}} \frac{1}{\omega - \epsilon(\mathbf{k} - \mathbf{q}) - \epsilon(\mathbf{q}) + i\eta}.\end{aligned}$$

In 1D, $\bar{g}_0(\omega)$ equals the diagonal element of the free propagator for a particle in 2D, which can be expressed in terms of elliptical functions and calculated efficiently [91]. Similar considerations hold in higher dimensions [92].

The equations of motions are then solved following the procedure described at length in Refs. [62, 90]. For consistency, we sketch the main steps here. First, we introduce vectors $W_n = (F_{2n-1}, F_{2n})^T$ for $n \geq 0$ (the arguments \mathbf{k}, ω, i of the propagators are not written explicitly from now on). Note that with this definition, $W_0 = (F_{-1}, F_0)$, yet F_{-1} is not properly defined. However, the final result has no dependence on F_{-1} , as we show below. The equations of motion are then rewritten in terms of W_n to read $\gamma_n W_n = \alpha_n W_{n-1} + \beta_n W_{n+1}$. The matrix elements of the 2×2 matrices $\alpha_n, \beta_n, \gamma_n$, are easily read off Eq. (4.2).

Defining $A_n = [\gamma_n - \beta_n A_{n+1}]^{-1} \alpha_n$, the physical solution of these recurrence equations is $W_n = A_n W_{n-1}$. Introducing a sufficiently large cut-off N_c where $W_{N_c} = 0$, we can then compute A_1 and have $W_1 = A_1 W_0$, i.e.,

$$\begin{pmatrix} F_1 \\ F_2 \end{pmatrix} = A_1 \begin{pmatrix} F_{-1} \\ F_0 \end{pmatrix} = \begin{pmatrix} a_{11} & a_{12} \\ a_{21} & a_{22} \end{pmatrix} \begin{pmatrix} F_{-1} \\ F_0 \end{pmatrix}.$$

One can easily check that $a_{11} = a_{21} = 0$. Thus, we obtain $F_1 = a_{12} F_0$ and $F_2 = a_{22} F_0$. Substituting these results back into the EOM for G we obtain

$$\begin{aligned}G(\mathbf{k}, \omega) &= G_0(\mathbf{k}, \omega) \left[1 + \right. \\ &\quad \left. \sum_i \frac{e^{i\mathbf{k}\mathbf{R}_i}}{\sqrt{N}} ((2g_2 + 6g_4)a_{12} + g_4 a_{22} + U) F_0(\mathbf{k}, \omega, i) \right].\end{aligned}$$

Since, by definition, $G(\mathbf{k}, \omega) = \sum_i \frac{e^{i\mathbf{k}\mathbf{R}_i}}{\sqrt{N}} F_0(\mathbf{k}, \omega, i)$, and given that a_{12}, a_{22}

are functions of ω only, we find:

$$G(\mathbf{k}, \omega) = \frac{1}{G_0^{-1}(\mathbf{k}, \omega) - (2g_2 + 6g_4)a_{12} - g_4a_{22} - U}. \quad (4.3)$$

Note that the coefficients a_{12} and a_{22} depend on all parameters of the model, including U . As a result, the position of the lowest pole of Eq. (4.3) is *not* simply linear in U , although this is a good approximation for the strongly bound bipolaron.

We emphasize that this MA expression becomes exact in two limiting cases. First, in the atomic limit $t \rightarrow 0$ the free propagator has no off-diagonal terms and thus no error is introduced by dropping them from the equations of motion. Second, without el-ph interactions ($g_n = 0$) the Hamiltonian reduces to the Hubbard model which is exactly solvable in the two-particle case [93]. In both cases MA gives the exact solution.

4.3.2 Exact diagonalization

The results obtained via MA as outlined above are checked against exact diagonalization results in a bigger variational subspace designed to describe well the strongly bound S0 bipolaron. Hence, we only consider states where all the phonons are located on the same lattice site and at least one of the two electrons is close to this cloud. The basis states are of the form

$$|\mathbf{k}, n, \delta_1, \delta_2\rangle = \sum_i \frac{e^{i\mathbf{k}\mathbf{r}_i}}{\sqrt{N}} b_i^{\dagger, n} c_{i+\delta_1, \uparrow}^{\dagger} c_{i+\delta_2, \downarrow}^{\dagger} |0\rangle$$

with the constraint that either δ_1 or δ_2 is below a certain cut-off. In addition, a global cut-off N_c is imposed on $n + \delta_1 + \delta_2$. The ground state within the variational space is then computed using standard eigenvalue techniques.

The main difference between these ED and MA results is that MA discards contributions from configurations where the carriers are at different lattice sites. Comparing the two therefore allows us to gauge the importance of such terms, and to decide whether the speed gained from using the analytical MA expressions counterbalances the loss of accuracy.

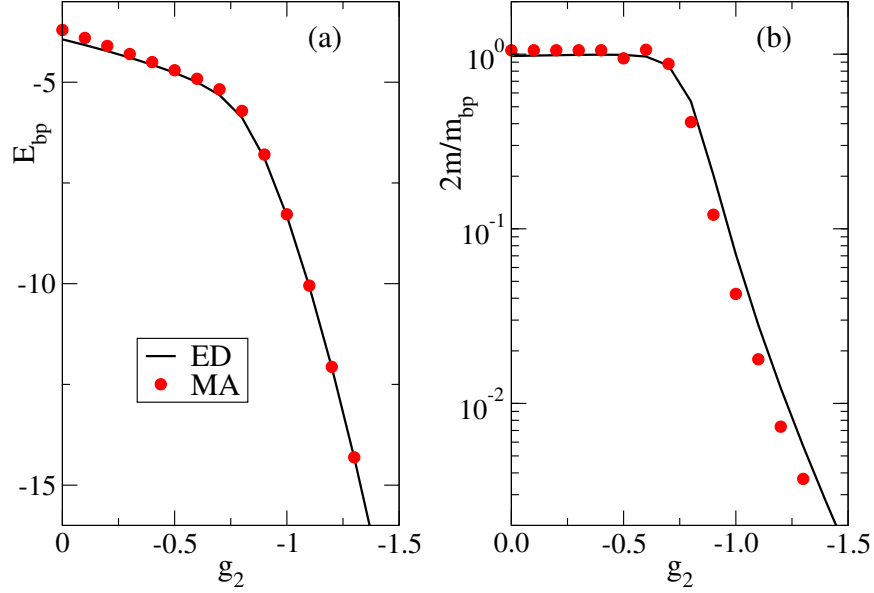


Figure 4.2: (a) Bipolaron ground-state energy, and (b) inverse effective mass for $t = 1, \Omega = 0.5, g_4 = 0.1$, computed with ED (solid black line) and MA (red dots).

4.4 Results

From now on we focus on the one-dimensional (1D) case, since our results from the previous chapter suggests that going to higher dimensions leads to qualitatively similar results.

Before discussing the MA results, we first compare them to those obtained from ED in the larger variational subspace discussed above. A typical comparison (for $t = 1, \Omega = 0.5$ and $g_4 = 0.1$) is shown in Fig. 4.2. The left panel shows the ground state energy and the right panel shows the inverse effective mass of the bipolaron. In the regime where the bipolaron is strongly bound, *i.e.* where its energy decreases fast and its effective mass increases sharply as $|g_2|$ increases, we find excellent agreement for the energy. The masses also agree reasonably well, but MA systematically *overestimates* the bipolaron mass. This is a direct result of the more restrictive nature of the MA approximation: By discarding configurations where the carriers occupy

4.4. Results

different sites, the mobility of the bipolaron is underestimated and thus the effective mass is overestimated. Nonetheless, this error is not very large, and only means that the bipolarons in the double well model are even lighter than calculated by MA. Due to similarly good agreement in all cases we verified, for the remainder of this work we only discuss results obtained with the more efficient MA method.

We emphasize that our approximation for computing the Green's function is only valid in the regime of strong binding and does not describe correctly the physics at weak coupling. Since neither MA nor ED, as implemented here, allow for the formation of two phonon clouds, neither describes the formation of a weakly bound S1 bipolaron (where polarons form on neighboring sites and interact with each other's clouds via virtual hoppings), nor the dissociation into two polarons as the coupling is further decreased [67, 68]. Accuracy in these parameter regimes can be improved by applying more sophisticated – yet much more tedious – versions of MA or ED for suitably expanded variational spaces. Here, however, we want to focus on the strong-coupling regime, where our results are accurate.

We show the ground-state properties of the bipolaron compared to those of two single polarons in Figs. 4.3, 4.4 for two different values of Ω . In all those panels, we have set $U = 0$ for simplicity; the role of finite U will be discussed at the end of this section.

The ground state energy of the bipolaron behaves qualitatively similar for all values of Ω and g_4 in that it shows a kink at some g_2 where the slope becomes steeper. This signifies the onset of the strong-coupling regime where the bipolaron energy is well below the energy of two independent polarons, consistent with a strongly bound bipolaron. At weaker coupling the results are not accurate since – as explained above – our version of MA cannot describe the dissociation of the bipolaron.

Consider now the behavior of the effective masses. For all parameters considered here, we see that the single polaron mass m_p starts out slightly above the free electron mass m , then decreases until it is almost as light as the free electron, before increasing again. This turnaround in the polaron mass is due to partial cancellation effects of the quadratic and quartic el-

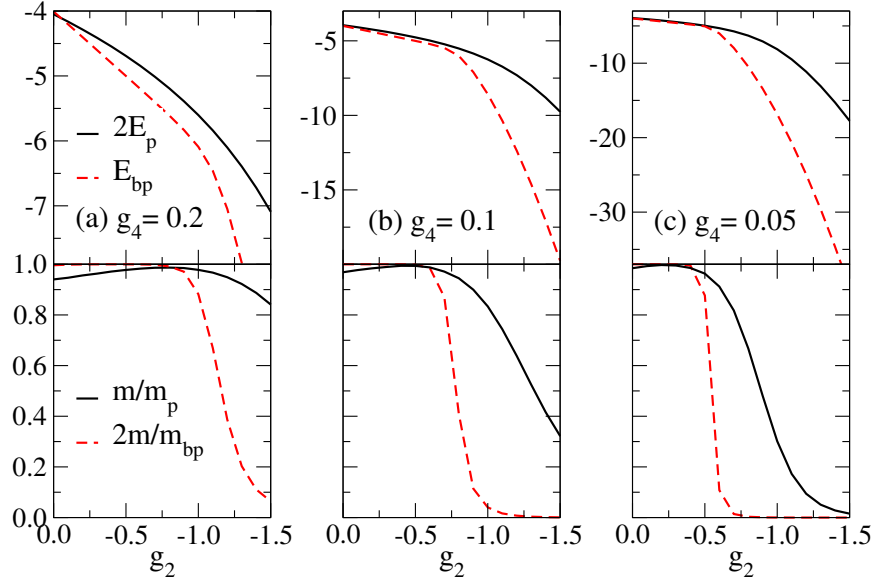


Figure 4.3: Ground-state properties (total energy and inverse mass) of the S0 bipolaron and two independent polarons for $t = 1$, $\Omega = 0.5$ and $g_4 = 0.2$, 0.1, and 0.05 for a), b), and c), respectively. For all panels, $U = 0$.

ph coupling terms, as discussed in Ref. [90]. We observe that when the *bipolaron* is already quite strongly bound, the single polaron can still be very light. Empirically, we find that in the strong-coupling regime $m_p \sim m \exp(-\gamma \Delta_p / \Omega)$ where $\Delta_p = -2t - E_p$ is the single-polaron binding energy and γ is a small numerical prefactor. This behavior is also found in the Holstein model[11] in the strong-coupling limit, where $\gamma = 1$, $\Delta_p = -g^2/\Omega$. The prefactor γ can be much smaller in the double well model because of the nature of the ionic potential. This was explained in detail in Ref. [90], and will be discussed in the context of bipolarons later in this section.

The bipolaron effective mass fluctuates around the value of $2m$ in the weak coupling regime. As explained above, here our method does not describe two independent polarons, but two independent free electrons whose effective mass should just be $2m$. However, the two-particle spectral function in this case does not have a low-energy quasi-particle peak. Instead, it has a continuum spanning the allowed two-particle continuum.

4.4. Results

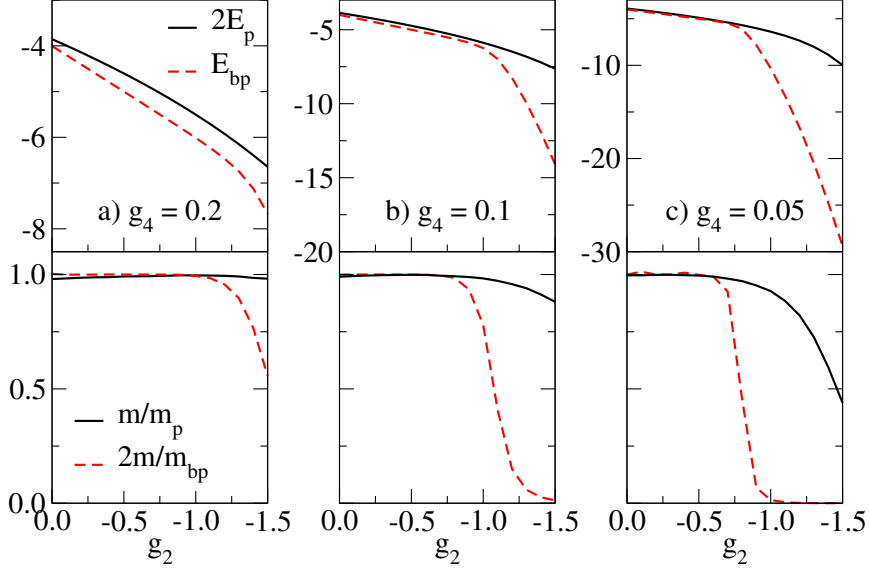


Figure 4.4: Ground-state properties (total energy and inverse mass) of the S0 bipolaron and two independent polarons for $t = 1, \Omega = 2$ and $g_4 = 0.2, 0.1,$ and 0.05 for a), b), and c), respectively. For all panels, $U = 0$.

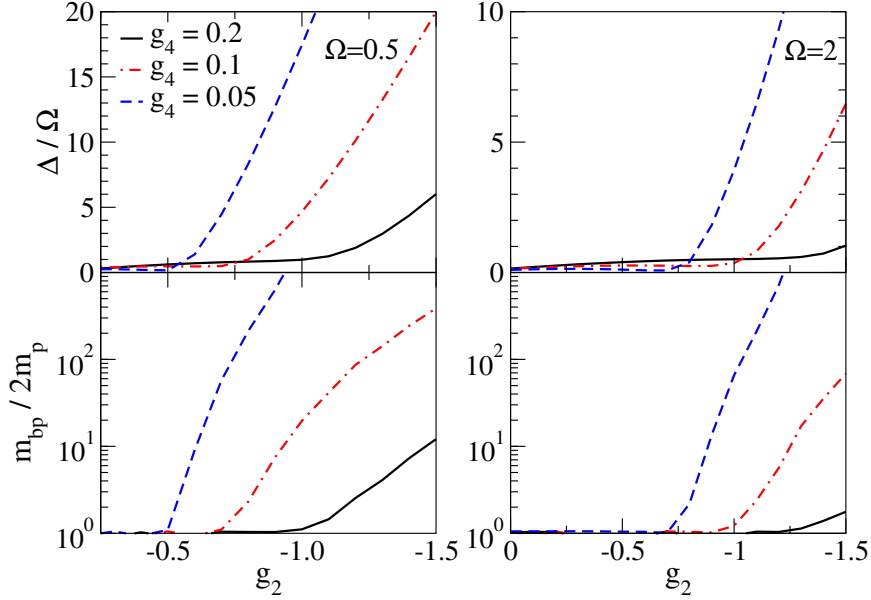


Figure 4.5: Binding energy Δ and effective-mass ratio $m_{\text{bp}}/2m_{\text{p}}$ of the bipolarons for $\Omega = 0.5$ and $\Omega = 2$ at different values of g_4 .

4.4. Results

Table 4.1: Some example values of the bipolaron binding energy and effective mass.

Ω	g_4	$ g_2 $	Δ/t	$m_{\text{bp}}/2m$
0.5	0.1	0.9	1.25	8.3
	0.2	1.3	1.48	4.4
2	0.1	1.3	3.11	5.9
	0.2	1.5	1.03	1.8

These issues disappear at stronger coupling where a strongly bound bipolaron forms and MA becomes accurate. The figures show that here the bipolaron quickly gains mass with increased coupling strength $|g_2|$, and that this increase is stronger the *smaller* g_4 is. Note that a smaller g_4 actually means stronger coupling, because the wells are deeper and further apart [90].

The same data is displayed in a different way in Fig. 4.5, where we show the magnitude of the bipolaron binding energy $\Delta = 2E_p - E_{\text{bp}}$ and the ratio of bipolaron to single-polaron masses, $m_{\text{bp}}/2m_p$. The strongly bound bipolaron regime (where the results are accurate) is reached when these quantities vary fast with g_2 . In particular, the results for $m_{\text{bp}}/2m_p$ show that here the bipolaron mass increases much more quickly than the polaron mass. This is not surprising for models like this, where the phonons modulate the on-site energy of the carrier. At strong coupling the results can be understood starting from the atomic limit $t = 0$, treating hopping as a perturbation. Since both carriers must hop in order for the bipolaron to move, one expects that $m_{\text{bp}}/m \propto (m_p/m)^2$; indeed, we find this relation to be valid for a wide range of parameters for our model.

Although in this regime the bipolaron quickly gains mass, there are parameter ranges where its mass is still rather light while the bipolaron is strongly bound. Examples of such parameters are given in Table 4.1. We note that qualifiers such as "strongly bound" and "light" are subjective. In our case, we take the bipolaron as strongly bound when the binding energy $\Delta/\Omega > 1$ and the ratio $m_{\text{bp}}/2m < 10 - 20$, consistent with other references [89, 86].

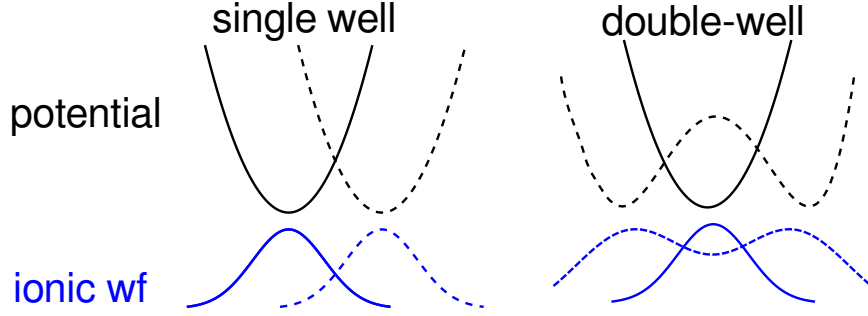


Figure 4.6: Ionic potential (above) and ionic ground-state wavefunction (below) in the single-well and double-well models. Solid lines correspond to the situation without an additional carrier, dashed lines to the situation with an additional carrier.

Light but strongly bound bipolarons were previously found for long-range el-ph coupling [86]. The explanation is that in such models, carriers induce a spatially extended lattice deformation, not one that is located in the immediate vicinity of the carrier as is the case at strong coupling in local el-ph coupling models. Because of their extended nature, the overlap between clouds displaced by one lattice site (which controls the effective hopping) remains rather large, meaning that the polarons and bipolarons remain rather light in such models.

Even though it is due to a local el-ph coupling, the mechanism resulting in light bipolarons in our model is qualitatively similar, as illustrated in Fig. 4.6. In the linear Holstein model the effect of an additional carrier added to a lattice site is to shift the equilibrium position of the ionic potential. The ionic wavefunctions corresponding to an empty and an occupied site therefore have only small overlap, which strongly reduces the effective carrier hopping. In the double-well model, in contrast, the ionic wavefunction for the doubly-occupied site has appreciable overlap with the ionic wavefunction for an empty or a singly-occupied site and thus does not reduce the effective hopping as much.

We conclude with a brief discussion of the effects of a finite, repulsive U . For a very strongly coupled S0 bipolaron, most of the weight is in states

with both carriers on the same site. In this regime, the binding energy decreases (nearly) linearly with U , $\Delta_{\text{bp}}(U) \approx \Delta_{\text{bp}}(U = 0) - U$. However, increasing U increases the energy cost of the S0 state and thus encourages hybridization with off-site states, which results in an overall smaller effective mass. We show results for the bipolaron energy and effective mass as a function of U in Fig. 4.7. We stay within the regime $U < \Delta_{\text{bp}}$ where the bipolaron remains strongly bound. As predicted, the energy of the bipolaron increases linearly with U , which in turn means that the binding energy Δ_{bp} decreases linearly with U . The effective mass also decreases (approximately) linearly with U . This can be demonstrated for the strong coupling limit via second order perturbation theory in the hopping. Following along the lines in Refs. [67, 68], the effective hopping of the S0 bipolaron is of the form

$$m_{\text{bp}}^{-1} \propto t_{\text{eff}} \sim \frac{-t^2 e^{-\gamma\Delta/\Omega}}{2E_p - U}$$

for some constant γ . We see that the mass itself decreases linearly with U , with a steeper slope the larger the effective mass at $U = 0$.

In essence, provided that it is not large enough to break the bonding, a finite U does not change the overall picture and merely tunes the balance between the bipolaron binding energy and its effective mass.

4.5 Conclusions and outlook

In conclusion, we have investigated the bipolaron ground-state properties in the dilute limit of the double-well el-ph coupling model at strong coupling. We have demonstrated that due to the particular nature of the carrier-induced ionic potential, the double-well bipolaron can be strongly bound while remaining light compared to the bipolaron in the Hubbard-Holstein model. This suggests a new route to stabilizing such bipolarons, in addition to previously discussed mechanisms based on long-range el-ph coupling or special lattice geometries. We expect that a combination of these mechanisms will lead to even lighter bipolarons.

In this work, we have used and validated a simple extension of the Mo-

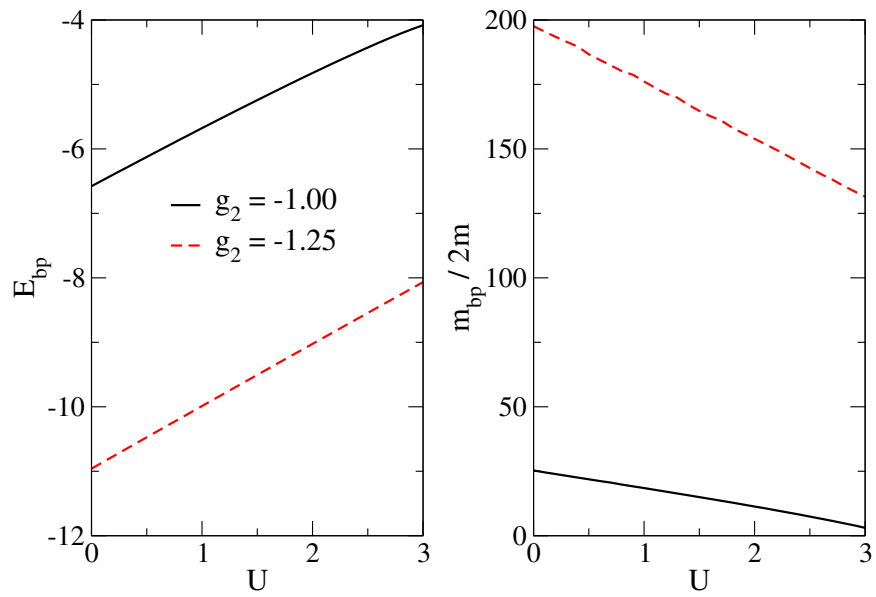


Figure 4.7: Bipolaron energy (left) and effective mass (right) as a function of the Hubbard U , for $t = 1, \Omega = 0.4$ and $g_4 = 0.1$. Similar results are found for other parameters if U is not large enough to lead to bipolaron dissociation.

4.5. *Conclusions and outlook*

mentum Average approximation to the two-carrier case. While this generalization is appropriate to describe a strongly bound S0 bipolaron, it cannot describe the off-site (S1) bipolaron that forms at larger Hubbard repulsion U , or the unbinding of the bipolaron at even larger U . A more sophisticated version of MA, currently under development, will give us insight into the full phase diagram of the double-well model.

Chapter 5

Single-polaron dispersion in the insulating limit of tetragonal CuO

We argue that tetragonal CuO (T-CuO) has the potential to finally settle one long-standing modelling issue for cuprate physics. We compare the one-hole quasiparticle (qp) dispersion of T-CuO to that of cuprates, in the framework of the strongly-correlated ($U_{dd} \rightarrow \infty$) limit of the three-band Emery model. Unlike in CuO_2 , magnetic frustration in T-CuO breaks the C_4 rotational symmetry and leads to strong deviations from the Zhang-Rice singlet picture in parts of the reciprocal space. Our results are consistent with angle-resolved photoemission spectroscopy data but in sharp contradiction to those of a one-band model previously suggested for them. These differences identify T-CuO as an ideal material to test a variety of scenarios proposed for explaining cuprate phenomenology.

5.1 Introduction

Understanding the high-temperature superconductivity in cuprates [22] is one of the biggest challenges in condensed matter physics. These layered materials contain two-dimensional (2D) CuO_2 layers which exhibit antiferromagnetic (AFM) order in the undoped limit, and host the superconducting Cooper pairs upon doping. Consequently, it is widely believed that understanding the behaviour of a doped CuO_2 layer is the key to understand the unusual properties of these materials.

5.1. Introduction

The first step in this quest is to understand the nature and dynamics of the quasiparticle (qp) that forms when one hole is doped into a CuO_2 layer. Despite huge efforts on the theory side, this issue is not yet fully settled.

The most relevant orbitals for the physics of the CuO_2 layer are the Cu $3d_{x^2-y^2}$ and the O $2p$ ligand orbitals, and the appropriate model is the three-band Emery Hamiltonian [24]. Zhang and Rice argued, however, that the resulting quasiparticle is a Zhang-Rice singlet⁵ (ZRS) hopping on the Cu sublattice and is thus well described by the much simpler one-band t - J or Hubbard Hamiltonians [26–30]. A lot of effort focusing on these (relatively) simpler one-band models was thus to follow. In the absence of exact solutions or accurate approximations for these strongly-correlated 2D Hamiltonians, progress was made through numerical studies of finite-size clusters. These showed that the qp dispersion is strongly influenced by the quantum fluctuations of the AFM background [94], and that longer-range hopping is needed to obtain a dispersion in quantitative agreement with what was measured experimentally [95–97, 16]. Similar results are obtained within Cluster Dynamical Mean Field Theory [31]. The longer-range hoppings required to achieve this agreement are similar to those calculated theoretically [32–34]. This was taken as proof that these extended one-band models provide the correct description, and the focus shifted to studying them at finite hole concentrations. Surprisingly, a lot of this work discards the longer-range hopping terms despite their proven relevance. While much such work was done in the past two decades, the lack even of consensus that these one-band models support robust, high-temperature superconductivity raises strong doubts about how appropriate they are to describe the hole-doped side of the phase diagram. It is much more likely that the one-band models (with properly adjusted longer-range hopping) describe correctly the physics of the electron-doped side, because in this case the full O bands are inert spectators.

There are two reasons why the one-band models might fail to find the desired physics at finite doping: (i) they may describe the single qp cor-

⁵We give a proper definition of the ZRS state later in this chapter when discussing the low-energy effective model. A sketch is given in Fig. 5.3.

rectly yet fail to appropriately model the effective interactions between qps , responsible for pairing. This was shown to occur when different degrees of freedom on different sublattices are mapped onto an effective single band model [98, 99]. Because in cuprates the doped holes reside on oxygen whereas the magnons reside on copper sites [100], a one-band model may thus fail to mimic the correct interaction between them; (ii) they may predict the correct qp dispersion for the wrong reasons, by describing different physics even at the single hole level. Support for the latter view comes from our recent work on the $U_{dd} \rightarrow \infty$ limit of the three-band Emery model; the resulting Hamiltonian has spins at the Cu sites and the doped holes move on the O sublattice [100]. In stark contrast to one-band models where spin fluctuations are key to obtaining the correct qp dispersion, here it is recovered even in the absence of spin fluctuations [3]. This qualitative difference shows that although the quasiparticles of these models have similar dispersion, this is driven by different physics [5].

To decisively settle the question of whether these one- and three-band models are equivalent, one must compare them for a material similar enough to CuO_2 that it should be described by similar Hamiltonians, however one for which they give different predictions so that (at least) one of them can be falsified experimentally. In this Letter we show that layers of tetragonal CuO (T-CuO) are precisely such a material, whose careful investigation can finally resolve these fundamental modeling issues.

Thin films of several unit cells of T-CuO were recently grown epitaxially on a SrTiO_3 substrate [101, 102]. They can be thought of as a stack of weakly-interacting CuO layers, whose structure is depicted in Fig. 5.1(a) and consists of two intercalated CuO_2 lattices (sharing the same O). A CuO_2 layer is sketched in Fig. 5.1(b). Because Cu $3d_{x^2-y^2}$ orbitals only hybridize with their ligand O $2p$ orbitals, shown in the same color in Fig. 5.1, the two CuO_2 sublattices would be effectively decoupled if pp hopping between the two sets of O $2p$ orbitals was absent.

In this case, a hole doped into one sublattice would evolve just like in a regular CuO_2 layer, and the same (now doubly-degenerate) qp dispersion would be predicted by both one- and three-band models, as already dis-

cussed.

However, the CuO₂ sublattices are coupled by pp hopping between the two sets of O $2p$ orbitals, which lifts this degeneracy. The resulting qp dispersion was measured by angle resolved photoemission spectroscopy (ARPES) [4]. It was found to be overall quite similar to that of CuO₂ and seemed to be well described by a small cluster study of a t - t' - t'' - J model. As we show next, this conclusion is opposite to the one we find for the $U_{dd} \rightarrow \infty$ limit of the three-band model. We predict a qualitatively different dispersion for T-CuO and CuO₂, but these differences are masked in magnetically twinned samples.

We give a detailed presentation of the model in section 5.2. In section 5.3 we describe the method we use to solve it. Results and discussions are given in section 5.4.

5.2 Model

We study the $U_{dd} \rightarrow \infty$ limit of the Emery model, with spins at the Cu sites and a single doped hole on the O sublattice. This limit is justified because U_{dd} is much larger than the other energy scales [25]. For a CuO₂ layer, the corresponding Hamiltonian, see Fig. 5.1(b), is [100]:

$$\hat{H} = \hat{T}_{pp} + \hat{T}_{swap} + \hat{H}_{J_{pd}} + \hat{H}_{J_{dd}}. \quad (5.1)$$

For simplicity of notation, we provide here the explicit expressions for the terms in the CuO₂ Hamiltonian, assuming that only the ligand O $2p$ orbitals are included. Generalization to including both sets of O $2p$ orbitals, and also to T-CuO, is straightforward. With the sign of positive/negative lobes as pictured in Fig. 5.1 and using $p_{i,\sigma}^\dagger$ as the creation operator for a hole in the ligand O $2p$ orbital located at i , we have:

$$T_{pp} = t_{pp} \sum_{i \in \text{O}, \delta, \sigma} r_\delta p_{i,\sigma}^\dagger p_{i+\delta, \sigma} - t'_{pp} \sum_{i \in \text{O}, \sigma} p_{i,\sigma}^\dagger (p_{i-\epsilon, \sigma} + p_{i+\epsilon, \sigma}). \quad (5.2)$$

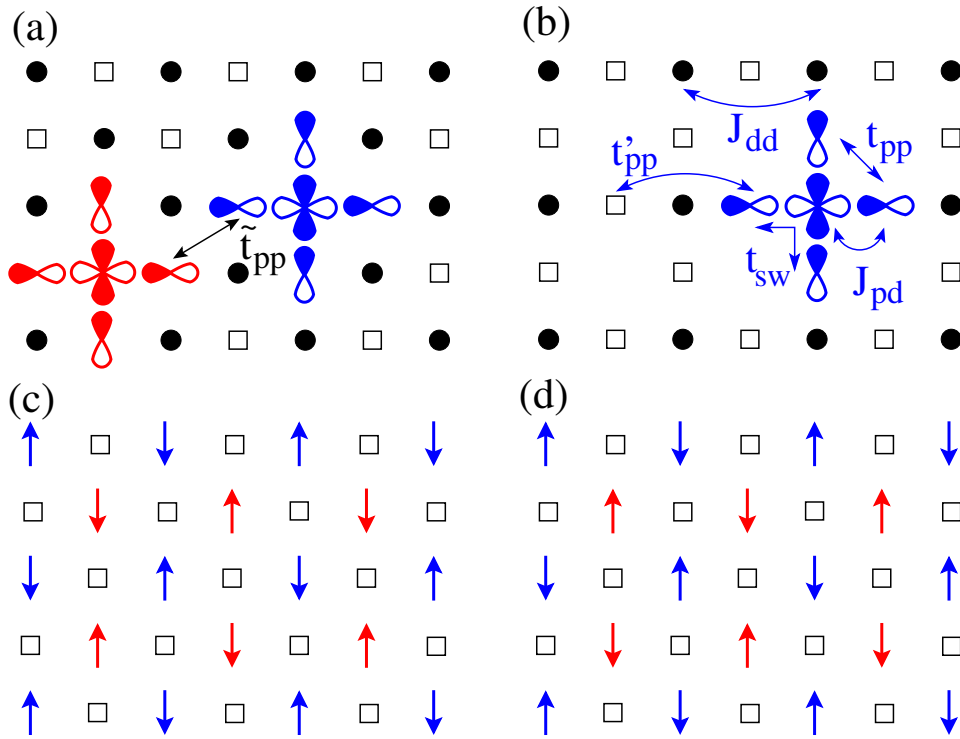


Figure 5.1: Structure of a layer of (a) T-CuO, and (b) CuO₂. Full circles are Cu, empty squares are O. The Cu $3d_{x^2-y^2}$ orbitals are drawn at a few sites, with white/dark lobes showing our choice for positive/negative signs. The corresponding ligand O $2p$ orbitals are also indicated on neighboring O sites. The T-CuO layer can be thought of as two intercalated CuO₂ layers sharing common O. The coppers of the two sublattices hybridize with different O $2p$ orbitals. Panels (c) and (d) show the two degenerate ground-states of the undoped T-CuO layer. Different colors are used for the Cu spins on the two sublattices for better visibility.

5.2. Model

The lattice constant is set to $a = 1$. The vectors $\boldsymbol{\delta} = \pm(0.5, 0.5), \pm(0.5, -0.5)$ are the distances between any O and its four nn O sites, and $r_{\boldsymbol{\delta}} = \pm 1$ sets the sign of each nn pp hopping integral in accordance with the overlap of the $2p$ orbitals involved. Next nn hopping is included only between O $2p$ orbitals pointing toward a common bridging Cu, separated by $\boldsymbol{\varepsilon} = (1, 0)$ or $(0, 1)$; hybridization with the $4s$ orbital of the bridging Cu further boosts the value of this hopping integral.

T_{swap} describes Cu-mediated effective hopping accompanied by a spin-swap. Specifically, the hole at a Cu site adjacent to the doped hole hops to one of its other neighbor O sites, followed by the doped hole falling into the vacated Cu orbital. Because the original doped hole replaces the Cu hole, their spins are swapped. Thus

$$T_{\text{swap}} = -t_{sw} \sum_{i \in \text{Cu}, \mathbf{u} \neq \mathbf{u}', \sigma, \sigma'} s_{\mathbf{u}-\mathbf{u}'} p_{i+\mathbf{u}, \sigma}^\dagger p_{i+\mathbf{u}', \sigma'} |i_{\sigma'}\rangle \langle i_{\sigma}|, \quad (5.3)$$

where $\mathbf{u}, \mathbf{u}' = (\pm 0.5, 0), (0, \pm 0.5)$ are the distances between a Cu and its four nn O sites. It shows the change of the Cu spin located at \mathbf{R}_i from σ to σ' as the doped hole changes its spin from σ' to σ while moving to another O. The sign $s_{\boldsymbol{\eta}} = \pm 1$ is due to the overlaps of the orbitals involved in the process, and the overall minus is because of the interchange in the order of holes⁶.

The origin of

$$\hat{H}_{J_{pd}} = J_{pd} \sum_{i, \mathbf{u}} \mathbf{S}_i \cdot \mathbf{S}_{i+\mathbf{u}} \quad (5.4)$$

is similar, except that now the Cu hole hops onto the O that is hosting the doped hole, followed by one of the two holes returning to the Cu. Unlike for \hat{T}_{swap} , charge is not moved in this process; instead, it gives rise to AFM exchange between the spin $\mathbf{s}_{i+\mathbf{u}}$ of the doped hole and that of its neighbor Cu, \mathbf{S}_i .

⁶We have not specified a canonical order of fermions in the many-body states because we only deal with a single explicit charge carrier. However, whatever order for the basis states we choose, the swap process will exchange an electron on a copper site and an electron on an oxygen sign, leading to the minus sign.

5.2. Model

Finally,

$$\hat{H}_{J_{dd}} = J_{dd} \sum_{\langle i,j \rangle'} \mathbf{S}_i \cdot \mathbf{S}_j \quad (5.5)$$

is the usual AFM coupling between neighbor Cu spins. The sum runs over all nearest-neighbor copper pairs except the one that has the bridging oxygen occupied by the doped hole. The energy scale $J_{dd} \sim 150$ meV is taken as the unit of energy, in terms of which $t_{pp} = 4.1$, $t'_{pp} = 0.6t_{pp}$, $t_{sw} = 3.0$ and $J_{pd} = 2.8$ [25]. Note that the oxygen Hubbard repulsion U_{pp} is not included in Eq. (5.1) because we consider only the case of a single doped hole.

In CuO_2 the important O $2p$ orbitals are the ligand orbitals, but it is straightforward to generalize the model to also include the in-plane non-ligand orbitals [3]. Because they do not hybridize with the Cu $3d_{x^2-y^2}$ orbitals, their addition does not change \hat{T}_{swap} , $\hat{H}_{J_{pd}}$ or $\hat{H}_{J_{dd}}$, all of which arise from such hybridization. Only \hat{T}_{pp} must be supplemented accordingly. By symmetry, nn hopping between two non-ligand orbitals is the same t_{pp} as for ligand orbitals, with signs dictated by the lobes' overlap. Hopping between nn ligand and non-ligand orbitals, which we call \hat{T}_{mix} and is shown by the black arrow in Fig. 5.1(a), has magnitude $\tilde{t}_{pp}/t_{pp} = (t_{pp,\sigma} - t_{pp,\pi})/(t_{pp,\sigma} + t_{pp,\pi}) = 0.6$ because $t_{pp,\sigma} = 4t_{pp,\pi}$ [103]. Thus, adding the non-ligand orbitals does not introduce new energy scales. For CuO_2 , their inclusion has a minor effect on the qp dispersion [3].

The Hamiltonian for T-CuO is a straightforward generalization of Eq. (5.1). The pp hopping is unchanged and described by the same $\hat{T}_{pp} + \hat{T}_{mix}$ discussed above. Because of the two intercalated Cu sublattices, there are two sets of terms \hat{T}_{swap} , $\hat{H}_{J_{pd}}$ and $\hat{H}_{J_{dd}}$ which couple Cu spins on each sublattice to each other and to the doped hole – if the latter occupies a $2p$ orbital that has ligand character for that Cu sublattice. We use the same parameters for T-CuO like for CuO_2 (the results remain qualitatively similar if the parameters are varied within reasonable ranges) and focus on the effect of \hat{T}_{mix} , which moves the hole between the two sets of $2p$ orbitals and changes to which Cu sublattice it is coupled.

For completeness, we note that in Ref. [4] a small nn exchange $\tilde{J}_{dd} \sim 0.04$ was also included between Cu spins on the different sublattices. We have

considered this term, as well as a weak \tilde{J}_{pd} coupling between the doped hole occupying a non-ligand orbital and its neighbor Cu spins (FM exchange is favored by Hund's coupling when the Cu hole hops into the O orbital orthogonal to that hosting the doped hole). None of these terms were found to lead to qualitative changes, and because of their relatively small magnitude, their quantitative effects are minor. As a result, we ignore them from now on.

5.2.1 Summary of model assumptions

There are quite a few assumptions going into the derivation of this model. For ease of reference, we summarize them here.

The first assumption concern the nature of the hopping terms included in the Hamiltonian. Longer-range hoppings could be considered, but are neglected because in the case of CuO_2 they were shown to have negligible effect [17].

The next assumption concerns the degree to which the $U_{dd} \rightarrow \infty$ limit is treated perturbatively. The resulting terms give rise to magnetic interactions and are carried out to leading order. Higher-order terms only serve to slightly renormalize already present terms [6].

The biggest assumption is in treating the magnetic interaction between holes on the copper ions with an Ising term instead of a Heisenberg term. In effect, this means neglecting the copper's spin fluctuations; the only way copper spins can get flipped is through their interaction with the oxygen hole. In essence, this assumption is similar to the assumption made for the double-well electron-phonon coupling model where quartic free-phonon terms were absorbed into the quartic el-ph interaction term. The justification, however, is a different one. The timescale of spin fluctuations would be $1/J_{dd}$, which is lower than the other timescales in the system. As such, it is not immediately clear that neglecting these fluctuations is valid. However, the results in [3] clearly justify this approximation *a posteriori*.

Additional assumptions concern terms arising from the interaction between the two intercalated layers. Here, we only explicitly include nearest-

neighbor hopping between them. Certain higher-order magnetic terms were found to have little effect on the ground state properties and are therefore neglected.

5.3 Method

As discussed in Ref. [3], we extract the qp dispersion $E_{qp}(\mathbf{k})$ from the one-hole propagator computed variationally in a restricted Hilbert space that allows up to n_m magnons to be created by the doped hole through \hat{T}_{swap} and $\hat{H}_{J_{pd}}$ processes, assuming that it was injected in a Néel-like background. Of course, in reality there are spin fluctuations in the AFM background, but because their energy scale J_{dd} is small, they occur so slowly as to have little effect on the qp dispersion: the hole creates and moves its magnon cloud on a timescale faster than that controlling the spin fluctuations, so the latter can be ignored [3, 5]. If the T-CuO energy scales are similar, and given the weak coupling between the two Cu sublattices, this approximation should remain valid.

In undoped T-CuO, each Cu sublattice has AFM order due to its $\hat{H}_{J_{dd}}$ term. As a result, any weak coupling \tilde{J}_{dd} between the two Cu sublattices is fully frustrated: a spin on one sublattice interacts with equal numbers of up and down spins from the other sublattice. Nevertheless, order by disorder selects one of the two degenerate states depicted in Fig. 5.1(c), (d) as the ground-state of the undoped system [104–106]. Because they have FM chains running along either the $x = y$ or $x = -y$ diagonals, they are related by a C_4 rotation so it suffices to study one case. Unlike in CuO_2 , for T-CuO in either of these states we expect that the quasiparticle dispersion $E_{qp}(\mathbf{k})$ is not invariant to C_4 rotations, only to C_2 ones.

Let us now discuss our variational method in a bit more detail. For any given momentum \mathbf{k} , our corresponding variational Hilbert space contains all states with at most n_m magnons and with a restriction on the maximum allowed magnon-hole distances, as discussed next.

Zero-magnon states are the eight Bloch states of momentum \mathbf{k} , one for each of the eight oxygen orbitals in the magnetic unit cell. States with

5.3. Method

magnons are Bloch states of total momentum \mathbf{k} for given hole and magnons configurations with fixed relative distances between holes and magnons. For example, the one-magnon states have the form

$$|\mathbf{k}, \alpha, \boldsymbol{\delta}\rangle = \frac{1}{\sqrt{N}} \sum_i e^{i\mathbf{k}\cdot\mathbf{r}_i} p_{i\alpha,\downarrow}^\dagger S_{i+\boldsymbol{\delta}}^+ |\text{Néel}\rangle$$

where i runs over the unit cells, $i\alpha$ denotes oxygen orbital $\alpha = 1, \dots, 8$ within unit cell i , and $S_{i+\boldsymbol{\delta}}^+$ is the magnon creation operator for a down-spin copper of the magnetic unit cell located a distance $\boldsymbol{\delta}$ away from unit cell i . The two-magnon and three-magnon states are constructed similarly by adding magnons in the units cells located at distances $\boldsymbol{\delta}_2$ and $\boldsymbol{\delta}_3$ apart, respectively.

Our restriction is that any $|\boldsymbol{\delta}| \leq N_{\max}$. For the 1- and 2-magnon states, the variational approach together with the Lanczos method [107] can easily handle distances of up to $N_{\max} = 10$, although the low-energy (quasi-particle) results are converged even for $N_{\max} = 2$. This is not surprising because we are concerned with the physics of the polaronic bound state, where the magnons are bound close to the hole. For the 3-magnon states, we set $N_{\max} = 1$, *i.e.* we only include 3-magnon configurations where the 3 magnons are located either in the same unit cell as the hole, or in a unit cell directly adjacent to it. These are the configurations with the highest weight in the quasiparticle cloud but, as the results show, they do not lead to significant changes. Less likely 3-magnon configurations, with the magnons spread further apart, can therefore be safely ignored at these energies.

We note that this approximation is valid for calculating low-energy properties. It would fail at describing higher energy features such as the correct locations for the polaron+one-magnon continuum, since its states necessarily have a magnon far away from the polaron, so the corresponding configurations need to be included to capture such higher energy features.

This approximation is conceptually similar to the momentum average approximation: The creation of bosons (phonons or magnons) lowers the energy available to the charge carrier such that it becomes a good approximation to restrict the presence of bosons to a final (small) number of lattice

sites. A difference is that while a lattice site in the Holstein model can harbour an arbitrary number of phonons, the number of magnons is limited to one per lattice site. The result is, depending on the formulation, a finite set of coupled equations of motion for the propagators or a sparse Hamiltonian of manageable size.

The resulting Hamiltonian matrix in our basis is sparse, because for each configuration there are only a few allowed hoppings and spin flips. Thus, it readily lends itself to the Lanczos method, which provides us with the spectral function $A(\mathbf{k}, \omega)$ relying only on computationally cheap matrix-vector products. The lowest-lying peak in the spectral function then gives us the qp dispersion.

5.4 Results and discussion

Figures 5.2(a)-(c) show $E_{qp}(\mathbf{k})$ for the magnetic order of Fig. 5.1(c) obtained with the variational method for $n_m = 1, 2, 3$, respectively, inside the Brillouin zone (BZ) displayed in Fig. 5.2(d). Full/dashed lines are for T-CuO/CuO₂.

In CuO₂, at the points marked by circles and squares there are equivalent nearly isotropic minima [97, 16]. With increasing n_m , the bandwidth narrows and the dispersion flattens below the polaron+one magnon continuum (both these effects are due to standard polaronic physics discussed in Ref. [3]) but the shape is unchanged. The results are nearly converged at $n_m = 3$ for CuO₂, with a bandwidth of $\sim 2J_{dd}$ in agreement with available exact diagonalization results and with experimental data [3]).

In T-CuO, we verified that for $\hat{T}_{mix} = 0$ the same (but now doubly-degenerate) dispersion is obtained. When \hat{T}_{mix} is turned on, this degeneracy is lifted. Only the low-energy eigenstate is shown in Fig. 5.2. Again, results are essentially converged for $n_m = 3$. As expected, the dispersion loses its invariance to C_4 rotations because the qp is now evolving in a magnetic background that lacks this symmetry. The dispersion in the $k_x = -k_y$ quadrants again displays deep, isotropic minima around $\pm(\frac{\pi}{2}, -\frac{\pi}{2})$ (full squares) and is thus rather similar to that in CuO₂. The difference, however,

5.4. Results and discussion

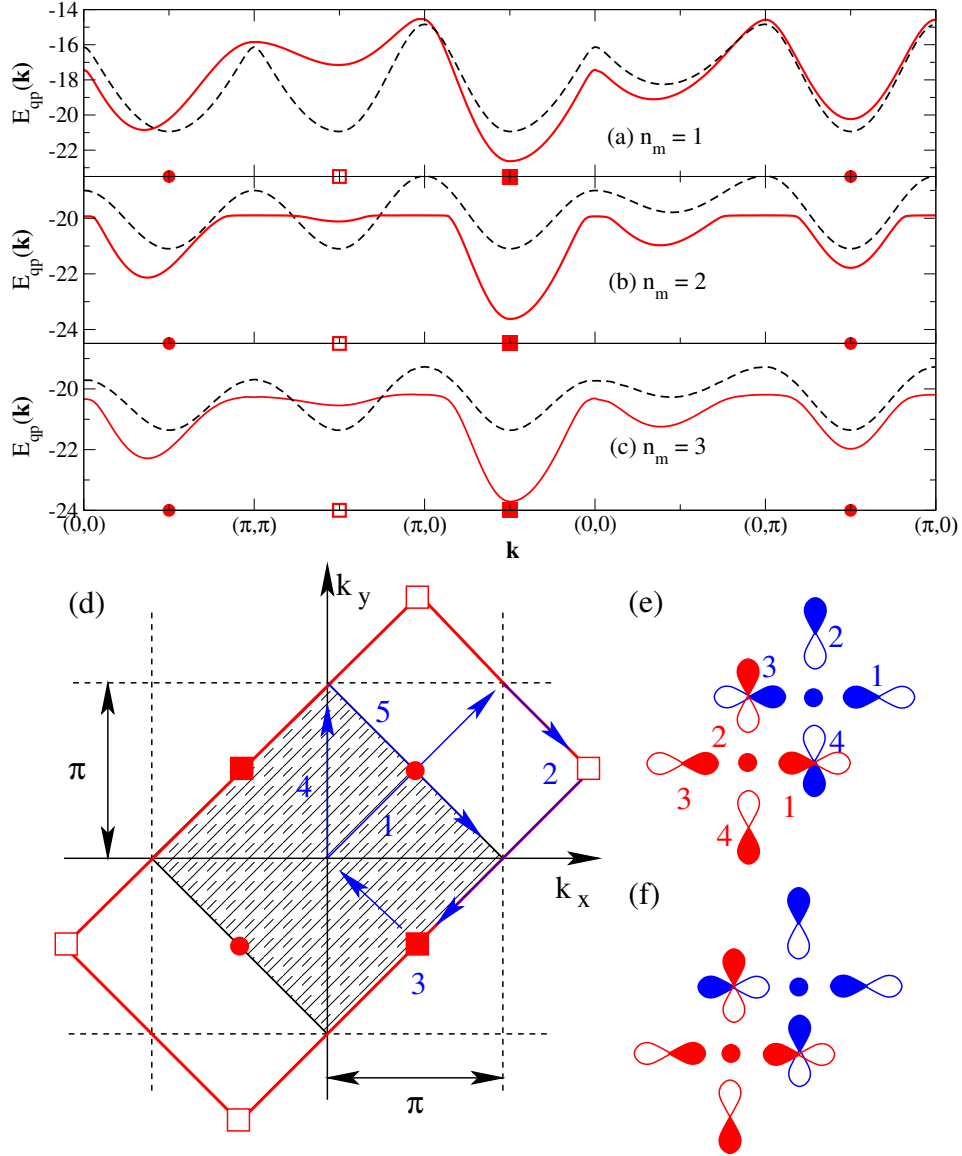


Figure 5.2: Qp dispersion in units of J_{dd} for (a) $n_m = 1$, (b) $n_m = 2$, and (c) $n_m = 3$ with full/dashed lines for T-CuO/CuO₂. The Brillouin zone for the magnetic order of Fig. 5.1(c) is shown in red in (b). The shaded area is the smaller BZ for CuO₂. The points marked by circles and empty/full squares are equivalent in CuO₂ but not in T-CuO. (d) Hopping between two adjacent ZRSs, and (e) between a ZRS (red) and one with $x - y$ symmetry (blue). See text for more details.

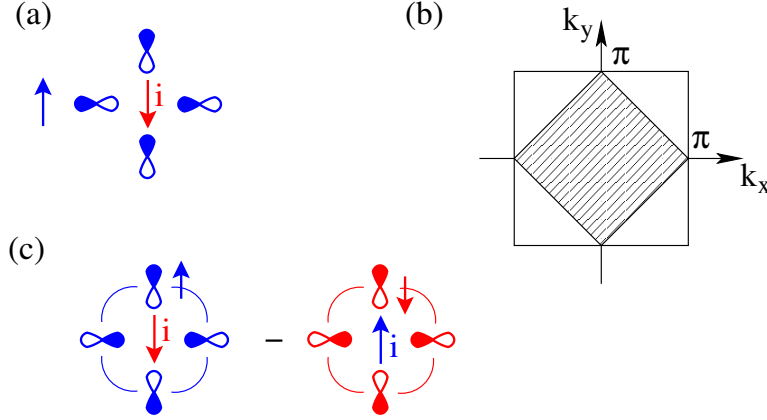


Figure 5.3: (a) Unit cell for CuO₂, with two Cu spins and four ligand O orbitals. We use the location i of the down-spin Cu as the reference point. The white/shaded areas indicate our choice for positive/negative lobes. (b) Magnetic Brillouin zone (shaded region) vs. full Brillouin zone (unshaded). (c) ZRS between a hole occupying the linear combination of ligand orbitals with $x^2 - y^2$ symmetry, and the spin of the central Cu. The Bloch state is obtained from its translations on the corresponding magnetic sublattice.

is significant in the $k_x = k_y$ quadrants near the $\pm(\frac{\pi}{2}, \frac{\pi}{2})$ points (circles). Not only are energies here higher than at the $\pm(\frac{\pi}{2}, -\frac{\pi}{2})$ points, but these minima are shifted toward the Γ point. Note also that the BZ corners (empty squares) continue to mark local minima, but now lying at high energies just below the polaron+one magnon continuum.

5.4.1 The ZRS Bloch state

Before we can continue our discussion of the results, we have to describe in more detail the nature of the Zhang-Rice singlet state. For the CuO₂ lattice, taking into consideration the AFM order of the Cu spins, we can choose the unit cell as shown in Fig. 5.3(a), with the corresponding magnetic Brillouin zone shown in Fig. 5.3(b).

To define a ZRS Bloch state, we first introduce:

$$p_{x^2-y^2, i, \sigma}^\dagger = \frac{1}{2} \left[p_{i+\frac{x}{2}, \sigma}^\dagger + p_{i+\frac{y}{2}, \sigma}^\dagger - p_{i-\frac{x}{2}, \sigma}^\dagger - p_{i-\frac{y}{2}, \sigma}^\dagger \right] \quad (5.6)$$

which describes the doped hole occupying a linear combination of ligand orbitals with $x^2 - y^2$ symmetry, centered on the Cu located at i . The ZRS is obtained when a hole occupying such a state is locked in a singlet with the Cu spin, therefore a ZRS Bloch state can be defined as⁷:

$$|d, \mathbf{k}\rangle = \sum_{i \in \text{Cu}_\downarrow} \frac{e^{i\mathbf{k} \cdot \mathbf{R}_i}}{\sqrt{N}} \frac{p_{x^2-y^2, i, \uparrow}^\dagger - p_{x^2-y^2, i, \downarrow}^\dagger S_i^+}{\sqrt{2}} |\text{Néel}\rangle. \quad (5.7)$$

Here, \mathbf{k} is any momentum in the magnetic Brillouin zone and the sum is only over sites in the spin-down Cu sublattice (since a spin-up doped hole can form a ZRS only with these spins).

Of course, one can also define Bloch states associated with singlets that have other symmetries for the linear combination of O orbitals. Of all these states, in CuO₂ the ZRS Bloch state is found to have the largest overlap with the low-energy quasiparticle wavefunction.

Its first excited state, on the other hand, is found to have the largest overlap with Bloch states based on the singlet with $x - y$ symmetry, *i.e.* the singlet obtained using $p_{x-y, i, \sigma}^\dagger = \frac{1}{2} \left[p_{i+\frac{x}{2}, \sigma}^\dagger + p_{i+\frac{y}{2}, \sigma}^\dagger + p_{i-\frac{x}{2}, \sigma}^\dagger + p_{i-\frac{y}{2}, \sigma}^\dagger \right]$ instead of $p_{x^2-y^2, i, \sigma}^\dagger$ in Eq. (5.7). We call this state $|p, \mathbf{k}\rangle$.

5.4.2 Low-energy effective model

We now prove that the unusual dispersion for T-CuO involves physics beyond the Zhang-Rice singlet. As such, it cannot be described by one-band models obtained through a projection onto these states.

We start by estimating the effect of \hat{T}_{mix} on the two CuO₂-like degenerate eigenstates that appear in its absence, and whose energy $E_0(\mathbf{k})$ is shown by the dashed lines in Fig. 5.2. Especially near the $(\pm\frac{\pi}{2}, \pm\frac{\pi}{2})$ points, the CuO₂ quasiparticle indeed has a large overlap with a ZRS Bloch state [5], and the hole occupies the $x^2 - y^2$ linear combination of O $2p$ ligand orbitals

⁷On occasion, reviewers have asked whether this expression misses an S_i^- operator, corresponding to the S_i^+ in the second term within the sum. We emphasize that the expression is correct as it stands and is *not* lacking a S_i^- term. It correctly describes a state that is a superposition of intact AFM order and one-magnon AFM order.

sketched for two nn sites in Fig. 5.2(e). For T-CuO, these two Bloch states combine into one Bloch state $|d, \mathbf{k}\rangle$ with a momentum \mathbf{k} in the bigger, T-CuO Brillouin zone. If we use it as an approximation for the low-energy eigenstate, then the T-CuO dispersion becomes $E_{qp}(\mathbf{k}) \approx E_0(\mathbf{k}) + \delta E(\mathbf{k})$, where $\delta E(\mathbf{k}) = \langle d, \mathbf{k} | \hat{T}_{mix} | d, \mathbf{k} \rangle$ is calculated in the following.

Previously, we have viewed T-CuO as two copies of a CuO₂ lattice, by adding two more Cu ions and four more oxygen orbitals to the unit cell while keeping the same lattice vectors. An alternative view is to use the same unit cell as for CuO₂, i.e., two copper ions and four oxygen orbitals, but have one of the lattice vectors shortened by a factor 2, depending on the relative magnetic ordering of the sublattices. If the copper spins are aligned ferromagnetically along the main diagonal, the proper lattice vectors are $\mathbf{a}_1 = a(1/2, 1/2)^T$ and $\mathbf{a}_2 = a(-1, 1)^T$.

While both views are valid, the latter view has the smallest possible unit cell and thus does not exhibit folding of the true Brillouin zone.

For a very simple effective theory, we use perturbation theory to investigate the influence of the inter-sublattice hopping \hat{T}_{mix} . Because this operator moves the hole between the two sets of O orbitals but cannot move magnons between the different Cu sublattices, only the magnon-free part of the quasi-particle wavefunction will contribute to matrix elements of this operator. Consider a two-dimensional Hilbert space containing the d - and p -wave ZRS states of momentum \mathbf{k} . Without \hat{T}_{mix} , we have

$$H = \begin{pmatrix} E_0 & 0 \\ 0 & E_1 \end{pmatrix}$$

where $E_0(\mathbf{k})$ and $E_1(\mathbf{k})$ are the CuO₂ dispersions of the groundstate and the first excited state.

We now apply \hat{T}_{mix} to each of the four oxygen basis states from which the ZRS-type states are built. Let

$$|1, \mathbf{k}\rangle := \sum_{i \in \text{Cu}_\downarrow} \frac{e^{i\mathbf{k} \cdot \mathbf{R}_i}}{\sqrt{N}} p_{i+\frac{\mathbf{x}}{2}, \uparrow}^\dagger |\text{Néel}\rangle.$$

and $|2, \mathbf{k}\rangle$, $|3, \mathbf{k}\rangle$ and $|4, \mathbf{k}\rangle$ defined analogously for the other oxygen orbitals enumerated counter-clockwise around the same copper ion. Note that here the sum is over all down-spins in the T-CuO lattice. Taking care of the proper phases for the hoppings, we have

$$\begin{aligned}\hat{T}_{mix} |1, \mathbf{k}\rangle &= -2\tilde{t}_{pp} \cos(\mathbf{k} \cdot \mathbf{a}_1) |1, \mathbf{k}\rangle - \tilde{t}_{pp} \left[e^{-i\mathbf{k} \cdot \mathbf{a}_1} + e^{-i\mathbf{k} \cdot (\mathbf{a}_1 - \mathbf{a}_2)} \right] |3, \mathbf{k}\rangle \\ \hat{T}_{mix} |2, \mathbf{k}\rangle &= -2\tilde{t}_{pp} \cos(\mathbf{k} \cdot \mathbf{a}_1) |2, \mathbf{k}\rangle - \tilde{t}_{pp} \left[e^{-i\mathbf{k} \cdot \mathbf{a}_1} + e^{-i\mathbf{k} \cdot (\mathbf{a}_1 + \mathbf{a}_2)} \right] |4, \mathbf{k}\rangle \\ \hat{T}_{mix} |3, \mathbf{k}\rangle &= -2\tilde{t}_{pp} \cos(\mathbf{k} \cdot \mathbf{a}_1) |3, \mathbf{k}\rangle - \tilde{t}_{pp} \left[e^{i\mathbf{k} \cdot \mathbf{a}_1} + e^{i\mathbf{k} \cdot (\mathbf{a}_1 - \mathbf{a}_2)} \right] |1, \mathbf{k}\rangle \\ \hat{T}_{mix} |4, \mathbf{k}\rangle &= -2\tilde{t}_{pp} \cos(\mathbf{k} \cdot \mathbf{a}_1) |4, \mathbf{k}\rangle - \tilde{t}_{pp} \left[e^{i\mathbf{k} \cdot \mathbf{a}_1} + e^{i\mathbf{k} \cdot (\mathbf{a}_1 + \mathbf{a}_2)} \right] |2, \mathbf{k}\rangle\end{aligned}$$

From this, we can now compute $\langle d/p, \mathbf{k} | \hat{T}_{mix} | d/p, \mathbf{k} \rangle$.

$$\begin{aligned}\langle d, \mathbf{k} | \hat{T}_{mix} | d, \mathbf{k} \rangle &= \tilde{t}_{pp} \cos(\mathbf{k} \cdot \mathbf{a}_1) [\cos(\mathbf{k} \cdot \mathbf{a}_2) - 1] \\ \langle p, \mathbf{k} | \hat{T}_{mix} | p, \mathbf{k} \rangle &= \tilde{t}_{pp} \cos(\mathbf{k} \cdot \mathbf{a}_1) [\cos(\mathbf{k} \cdot \mathbf{a}_2) - 3] \\ \langle p, \mathbf{k} | \hat{T}_{mix} | d, \mathbf{k} \rangle &= i\tilde{t}_{pp} \sin(\mathbf{k} \cdot \mathbf{a}_1) [\cos(\mathbf{k} \cdot \mathbf{a}_2) + 1]\end{aligned}$$

Strictly speaking, these matrix elements should be weighted by the appropriate quasiparticle weights $Z_{\mathbf{k}}$ corresponding to projection of the true qp eigenstate onto these non-interacting Bloch states. However, these weights are known to be rather featureless near the $(\pi/2, \pi/2)$ points that are most relevant in this discussion, so we ignore them in the following. This will affect results quantitatively, but not qualitatively.

If we ignore the p -wave states and only take into consideration the d -wave ZRS state, then the change in energy due to \hat{T}_{mix} becomes

$$\delta E(\mathbf{k}) = -\tilde{t}_{pp} \cos \frac{k_x + k_y}{2} [1 - \cos(k_x - k_y)]. \quad (5.8)$$

Because $\delta E(k_x = -k_y) = -2\tilde{t}_{pp} \sin^2 k_x$ and $\delta E(k_y = k_x \mp \pi) = -2\tilde{t}_{pp} \sin |k_x|$, the minima at $\pm(\frac{\pi}{2}, -\frac{\pi}{2})$ (full squares) are pushed to lower energies. Similarly, the minima at the corners of the BZ (empty squares) are pushed to high energies, which agrees with the results of Fig. 5.2.

However, things are different near the $\pm(\frac{\pi}{2}, \frac{\pi}{2})$ points (circles). Because

$\delta E(k_x = k_y) = 0$, here the dispersion should remain unchanged instead of the minima moving toward the Γ point. Moreover, we find that the overlap of the T-CuO quasiparticle wavefunction with the ZRS Bloch state $|d, \mathbf{k}\rangle$ *vanishes* at $\mathbf{k} = \pm(\frac{\pi}{2}, \frac{\pi}{2})$. These facts clearly prove that the changes near the $\pm(\frac{\pi}{2}, \frac{\pi}{2})$ points cannot be due to Zhang-Rice singlet physics.

Indeed, \hat{T}_{mix} hopping between $x^2 - y^2$ linear combinations centred at nn Cu sites is suppressed, see Fig. 5.2(e): *eg.*, a hole at site 1 of the lower Cu (red) hops into $p_1^\dagger + p_3^\dagger$ of the upper Cu (blue), which is orthogonal to its $x^2 - y^2$ linear combination. Instead, here hopping between adjacent $x^2 - y^2$ and $x - y$ combinations is enhanced, see Fig. 5.2(f). The shift of the $\pm(\frac{\pi}{2}, \frac{\pi}{2})$ minima toward Γ is due to a large mixing of the singlet with $x - y$ symmetry into the quasiparticle eigenstate, which thus loses its ZRS nature. Note that experiments like Refs. [108–110], which are sensitive only to the local singlet character, cannot distinguish between a ZRS singlet and one of such mixed symmetry.

Since the d -wave ZRS state alone cannot explain the dispersion of T-CuO, we now turn our focus to the Hilbert space spanned by the d -wave and p -wave ZRS states. It turns out that considering \hat{T}_{mix} in this two-dimensional Hilbert space is already sufficient to explain qualitatively the quasi-particle physics of T-CuO.

Let us consider the special case of the $k_x = k_y = k$ line, where $\mathbf{k} \cdot \mathbf{a}_2 = 0$ and $\mathbf{k} \cdot \mathbf{a}_1 = ka$. We then have

$$T_{mix}(k) = \begin{pmatrix} 0 & -2i\tilde{t}_{pp} \sin(ka) \\ 2i\tilde{t}_{pp} \sin(ka) & -2\tilde{t}_{pp} \cos(ka) \end{pmatrix}$$

The full numerical results showed that the minimum along this line gets shifted from $k = \pi/2$ closer to the Γ -point, and this readily follows from the simple form here: The off-diagonal elements provide mixing of the d - and p -states, and the energy $-2\tilde{t}_{pp} \cos(ka)$ of the p -state then moves the minimum to a lower k .

On the other hand, for $k_x = \pi - k_y = k$ we find that $T_{dd} = T_{pp} = 0$ and $T_{pd} = i\tilde{t}_{pp} [1 + \cos(\pi - 2k)]$. In this case, the Hamiltonian is symmetric

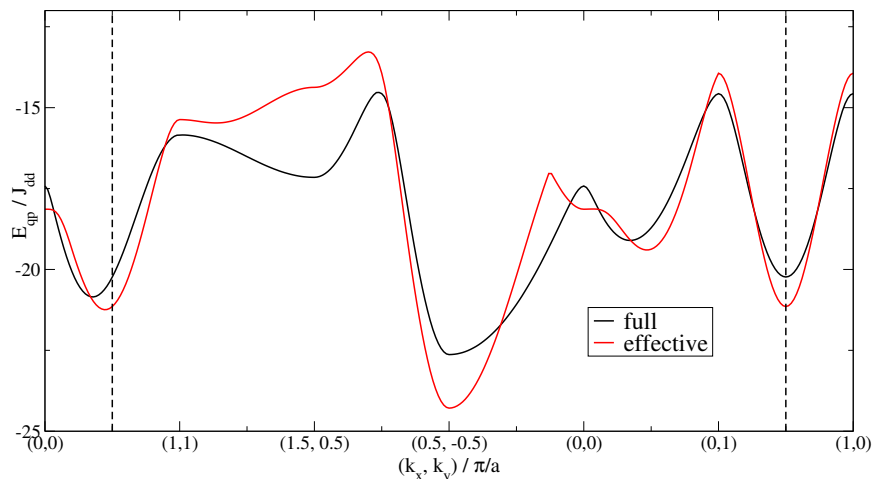


Figure 5.4: Comparison between the one-magnon numerical dispersion and the effective calculations involving both the low-energy and first excited state quasiparticles. The results are in qualitative agreement, in particular the shift of the minimum along $k_x = k_y$. The dashed lines are a guide to the eye to demonstrate that the peak along $\Gamma - M$ gets shifted away from $\mathbf{k} = (\pi/2, \pi/2)$ yet remains there along $X - X'$.

around $k = \pi/2$, and thus the minimum gets only shifted down in energy while remaining at $k = \pi/2$. Other directions can be considered similarly.

In Fig. 5.4 we compare the full numerical results to the effective low-energy results from the 2×2 Hamiltonian. The qualitative agreement is striking, in particular the shift of the minimum from $(\frac{\pi}{2}, \frac{\pi}{2})$ towards the Γ point emerges as predicted. Of course, quantitative disagreements result from the crudeness of our approximation: we neglected the quasiparticle weights which would narrow the bandwidth for this effective low-energy result, we ignored other higher-energy eigenstates as well as the fact that the CuO_2 low-energy and first excited quasiparticles are not pure $x^2 - y^2$ - and $x - y$ ZRS-like Bloch states, respectively. Nonetheless, the results satisfactorily show that the changes near $(\frac{\pi}{2}, \frac{\pi}{2})$ arise as a result of mixing between states with d - and p -symmetry. This mixing, in turn, results from a desire to gain kinetic energy from hopping between the sublattices, which is not possible in the pure ZRS subspace: for this relative arrangement of the two Néel

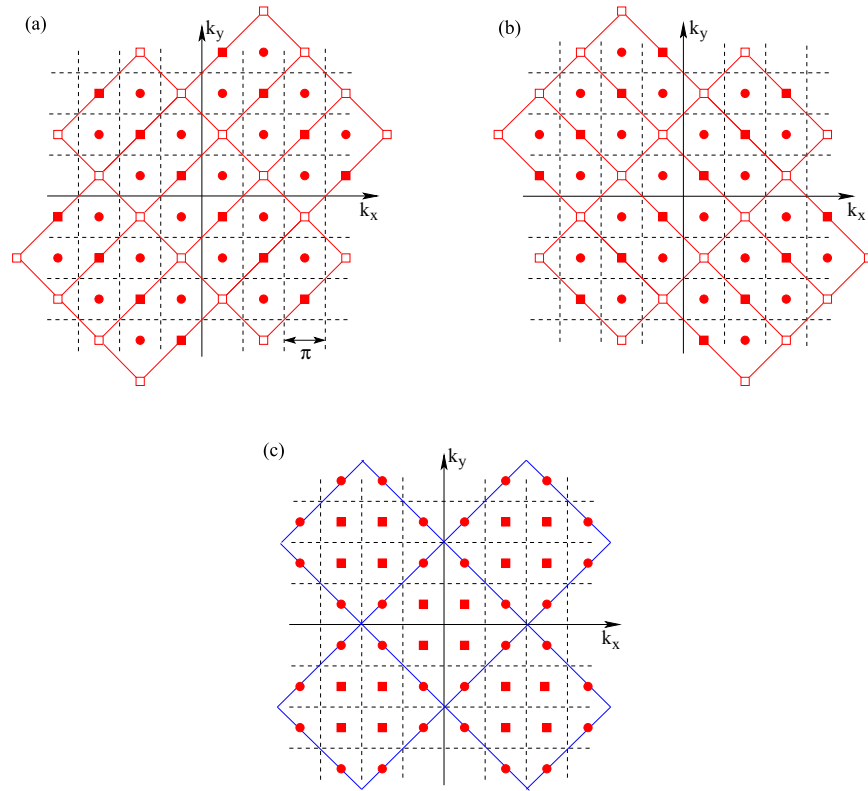


Figure 5.5: The first two panels show the Brillouin zones corresponding to the two possible magnetic orders of Fig. 5.1(c) and (d). The symbols mark the deep minima (full squares), displaced shallower minima (circles) and very shallow minima (empty squares). The two figures are related by a C_4 rotation. The third panel shows the average of these two patterns, where at each special point the deepest local minimum was selected. This pattern has a restored C_4 symmetry and a Brillouin zone (blue line) corresponding to one Cu site/unit cell. The pattern of deep/shallower minima is like that found experimentally.

Cu sublattices, \hat{T}_{mix} cannot hop a ZRS with momentum $k_x = k_y$ between neighbor Cu sites, see Fig. 2(d) of the main text. Higher-energy physics, of non-ZRS origin, then becomes relevant.

We checked that adding terms like \tilde{J}_{dd} and \tilde{J}_{pd} has no qualitative effect: the dispersion remains like in Fig. 5.2. This is expected because their matrix elements are small and/or featureless near $(\pm\frac{\pi}{2}, \pm\frac{\pi}{2})$. We are therefore confident that our prediction is robust.

5.4.3 Comparison to ARPES

Angular resolved photoelectron spectroscopy (ARPES) finds the T-CuO qp dispersion to obey C_4 symmetry and to have a large Brillouin zone, corresponding to a unit cell containing one Cu and one O atom [4]. Both features are very surprising for the long-range magnetic orders of Figs. 5.1(c), (d), each of which break the C_4 symmetry. Moreover, any AFM-type order has at least two magnetically non-equivalent Cu atoms and thus can have a BZ like in Fig. 5.2(d) or smaller, not larger. Our results become consistent with the ARPES data if we assume the presence of magnetic domains in both ground-states, so that their average is measured experimentally. Indeed, as shown below, averaging the band-structure of Fig. 5.2(d) with its counterpart rotated by 90° leads to an apparent doubling of the Brillouin zone and a new pattern of minima with two different energies, in agreement with those found experimentally.

The result of averaging over domains with both possible orientations is demonstrated in Fig. 5.5. Panel (a) shows the T-CuO Brillouin zones (red rectangles) from Fig. (d) of the main text, which corresponds to the magnetic order of Fig. 5.1(c). The symbols mark the deep minima (full squares), displaced shallower minima (circles) and very shallow minima (empty squares). Panel (b) is obtained by a C_4 rotation and corresponds to the magnetic order of Fig. 5.1(d). Their average is shown in panel (c), where the symbols now mark the lowest-energy local minimum. The resulting pattern agrees with that measured experimentally for T-CuO. The large Brillouin zones (blue squares) corresponding to a unit cell with one Cu per

basis emerges naturally, as do the patterns of deep and shallower minima.

Fig. 5.6 shows the quasiparticle dispersion along the same contour discussed in Fig. 1 of Ref. [4], for both magnetic orientations. Note that our results are in hole language, so to compare with their ARPES data the energies should be reversed, $E_{qp} \rightarrow -E_{qp}$. For ease of comparison, the lower panel shows the same results in this electron picture, with the symmetry points also labelled like in Ref. [4].

We predict that a dispersion like in Fig. 5.2 should appear in the ARPES of “magnetically untwinned” T-CuO films in the insulating limit. This is very different and therefore easily distinguishable from the one-band model prediction [4]. The observation of this pattern, with shallower displaced minima in two of the quadrants, will provide a clear proof of low-energy physics beyond the ZRS, and of the superiority of three-band models to model such materials. If T-CuO films can be doped, for example by gating, this new pattern of minima will open extraordinary opportunities to test many ideas relating the shape of the Fermi surface, location of “hot spots” and possibility of nesting, to much of the cuprate phenomenology, including the symmetry of the pairing and of the superconducting gap, formation of stripes, appearance and relevance of various other ordered phases, etc.

While the feasibility of such experiments remains to be determined, an important lesson from this study is that low-energy physics of non-ZRS nature can arise in such materials in suitable circumstances/symmetries. The presence of disorder, of other nearby quasiparticles, of stripes, charge-density wave or other ordered phases may have a similar effect in CuO₂ layers.

5.4. Results and discussion

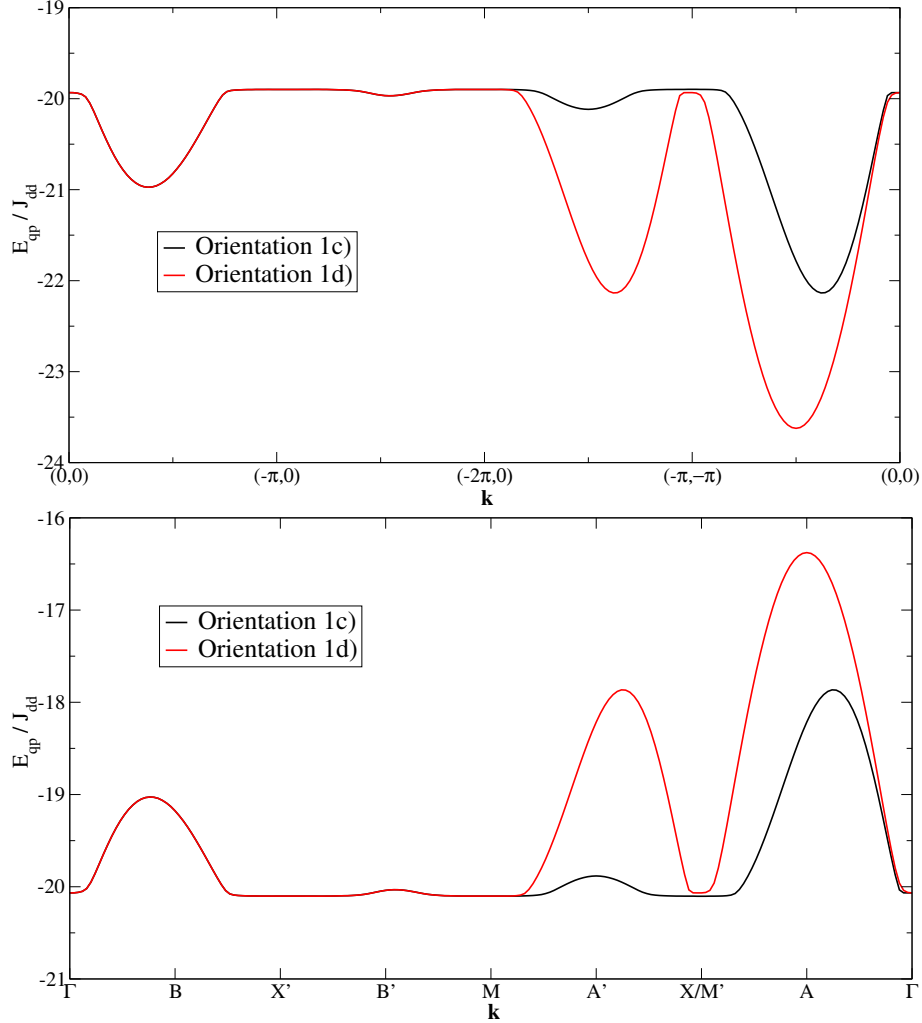


Figure 5.6: Quasiparticle dispersion for the two orientations of the magnetic background, along the contour considered in Ref. [20]. Top panel shows the results in the hole picture used throughout this work, whereas the low panel shows the same results in the electron picture relevant for experiments, with further tuning of the parameters. Also, we note that the slight displacements of the shallower minima have not been observed experimentally. This may be because of the very broad widths of the quasiparticle peaks and the loss of spectral weight on one side of these points, which may mask them. In “untwinned” samples the scattering rate should be lower, which may make the observation of these displacements towards Γ more easily visible. Of course, in that case the lack of C_4 symmetry and existence of really shallow minima should also become visible.

Chapter 6

Conclusions

6.1 Summary of this work

In this thesis, we have studied a variety of simple extensions to commonly used model Hamiltonians. Throughout, we have seen that even seemingly minor alterations can lead to drastic quantitative and, more importantly, qualitative changes in the system's behaviour. Our results highlight that longstanding and commonly held assumptions about certain systems and models can be wrong when they are based on extrapolations of the simple standard Hamiltonian.

In Chapter 2, we first introduced higher-order non-linear terms into the standard Holstein model's electron-phonon coupling. We demonstrate that the most dramatic qualitative changes are due to the quadratic term and thus a-posteriori justify that we focus mainly on this case. By accessing the polaron's ground-state properties via an extension to the momentum-average approximation, it is seen that even a small quadratic term leads to a complete change in the polaron's characteristics, making it much lighter. We argue that these results invalidate a large portion of what is commonly assumed regarding polaronic behaviour: The linear model, by necessity, assumes that lattice deformations are small. In the strong coupling regime, it then predicts that lattice deformations are large. The quadratic model, on the other hand, suffers from no such contradiction: By assuming moderate lattice deformations and thus keeping terms up to second order, the quadratic model predicts only small to moderate lattice deformations and thus remains internally consistent.

In Chapter 3, we consider a different type of non-linear Holstein model, one where the linear term is non-existent due to symmetry. We call this

the double-well electron-phonon coupling model. For this model, we show that its results cannot be reproduced by an effective linear model. We then highlighted similarities and differences between this model's polaron and that of the linear model.

The double-well model's bipolaron is studied in Chapter 4, where we show that the particular nature of the double-well electron-phonon coupling can lead to bipolarons that are strongly bound yet lightweight. Bound quasi-particles with this property were previously believed to be restricted to much more complicated models, either to those with peculiar lattice geometries or much more complicated electron-phonon interactions. In studying this problem, we have also introduced a first step to extending the momentum-average approximation to systems with more than one particle.

Finally, in Chapter 5 we study a novel type of copper-oxide layer, the recently grown tetragonal copper oxide T-CuO. This model can be thought of as an extension of the thoroughly studied CuO_2 layer, extended with a second intercalated copy weakly coupled via inter-sublattice hopping. We used a variational method similar to MA and solved it via exact diagonalization to study the spectral function and dispersion of the resulting quasi-particle. We discover that the dispersion is quite significantly changed from that of CuO_2 in a way that cannot be explained by a one-band Zhang-Rice singlet type of state. Instead, the inclusion of the small inter-band coupling requires us to use a multi-band description. The importance of this result comes from the fact that a long-standing theoretical issue regarding the cuprates is precisely whether the correct model for the cuprates is a single-band model (where spin-fluctuations play an important part) or a multi-band model (where spin-fluctuations are relatively unimportant). We demonstrate how our results establish that T-CuO can be an experimental test case for this important modelling question.

6.2 Further developments

Our calculations for the non-linear Holstein model in Chapter 2 were performed for the single-polaron case. A follow-up question to our results is

whether quadratic terms also have a strong impact at finite density. This requires different techniques. A former member of our group has pursued this avenue for the two-dimensional Hubbard-Holstein model [70, 71] using determinant Quantum Monte Carlo methods. Their results confirm that small non-linear terms remain important, in that they strongly influence the effective electron-lattice coupling and charge-density-wave correlations.

Similarly, the double-well electron-phonon coupling model should be studied at finite temperature and density. An open question would be if the thermodynamic limit shows spontaneous symmetry breaking, which would manifest itself as (anti-)ferroelectricity. Furthermore, with the results of Chapter 4 in mind, a study of the superconducting properties would reveal if the strongly-bound yet lightweight bipolarons of the double-well model can condensate and give rise to polaronic superconductivity.

The immediate follow-up to our study of T-CuO is clear: Experimentalists should aim to grow untwinned samples of T-CuO and carefully study its dispersion, to answer whether the results of our three-band model or of a one-band tJ-model are those realized in the material. Another interesting question is whether there are other effects present in CuO₂ that can give rise to similar non-ZRS physics. Such effects would likely be based on symmetries that are incompatible with a *d*-wave object, similar to how the inter-sublattice hopping leads to destructive interference for the *d*-wave ZRS.

Another avenue of exploration is to follow up on the premise that it is three-band models, not one-band models, that correctly capture the interaction between quasi-particles. Currently ongoing work in our group studies the effective interaction between two holes in a CuO₂ layer in the same $U_{dd} \rightarrow \infty$ limit of the three-band Emery model as we used in our study of T-CuO. The question is whether this model, in contrast to the tJ-model, shows an attractive effective interaction between two holes mediated by magnons.

Apart from the particular model Hamiltonians we have studied in this thesis, our general approach is flexible and can be applied to other models. It proves particularly useful when studying a small number of carriers coupling to gapped bosonic modes. The underlying idea of both MA and the various

6.2. *Further developments*

variational approaches is that creation of these bosonic modes costs energy. In the MA view, this means that the carrier loses energy when it creates a boson. At energies below the free carrier's ground state, its real-space propagator decays exponentially, justifying its replacement by a simplified version. In the variational view, subspaces with different boson numbers are well separated, justifying a cut-off at relatively small boson number. In addition, a combination of the MA and variational arguments justifies variational approximations where the carrier is forced to stay close to the bosonic modes it excites.

Bibliography

- [1] Mona Berciu. Green's function of a dressed particle. *Phys. Rev. Lett.*, 97:036402, Jul 2006. doi: 10.1103/PhysRevLett.97.036402. URL <http://link.aps.org/doi/10.1103/PhysRevLett.97.036402>.
- [2] M Möller, A Mukherjee, CPJ Adolphs, DJJ Marchand, and M Berciu. Efficient computation of lattice green functions for models with longer range hopping. *Journal of Physics A: Mathematical and Theoretical*, 45(11):115206–115214, 2012.
- [3] Hadi Ebrahimnejad, George A Sawatzky, and Mona Berciu. The dynamics of a doped hole in a cuprate is not controlled by spin fluctuations. *Nature Physics*, 2014.
- [4] S. Moser, L. Moreschini, H.-Y. Yang, D. Innocenti, F. Fuchs, N. H. Hansen, Y. J. Chang, K. S. Kim, A. L. Walter, A. Bostwick, E. Rotenberg, F. Mila, and M. Grioni. Angle-resolved photoemission spectroscopy of tetragonal cuo: Evidence for intralayer coupling between cupratelike sublattices. *Phys. Rev. Lett.*, 113:187001, Oct 2014. doi: 10.1103/PhysRevLett.113.187001. URL <http://link.aps.org/doi/10.1103/PhysRevLett.113.187001>.
- [5] H Ebrahimnejad, G A Sawatzky, and M Berciu. Differences between the insulating limit quasiparticles of one-band and three-band cuprate models. *Journal of Physics: Condensed Matter*, 28(10):105603, 2016.
- [6] Bayo Lau. *Modeling Polarons in Transition-Metal Oxides*. PhD thesis, The University Of British Columbia (Vancouver), 2011.

Bibliography

- [7] P. Hohenberg and W. Kohn. Inhomogeneous electron gas. *Phys. Rev.*, 136:B864–B871, Nov 1964. doi: 10.1103/PhysRev.136.B864. URL <http://link.aps.org/doi/10.1103/PhysRev.136.B864>.
- [8] W. Kohn and L. J. Sham. Self-consistent equations including exchange and correlation effects. *Phys. Rev.*, 140:A1133–A1138, Nov 1965. doi: 10.1103/PhysRev.140.A1133. URL <http://link.aps.org/doi/10.1103/PhysRev.140.A1133>.
- [9] M. Born and R. Oppenheimer. Zur quantentheorie der molekeln. *Annalen der Physik*, 389(20):457–484, 1927. ISSN 1521-3889. doi: 10.1002/andp.19273892002. URL <http://dx.doi.org/10.1002/andp.19273892002>.
- [10] Neil W Ashcroft, N David Mermin, and Sergio Rodriguez. Solid-statephysics. *American Journal of Physics*, 46(1):116–117, 1978.
- [11] T Holstein. Studies of polaron motion: Part i. the molecular-crystal model. *Annals of Physics*, 8(3):325 – 342, 1959. ISSN 0003-4916. doi: [http://dx.doi.org/10.1016/0003-4916\(59\)90002-8](http://dx.doi.org/10.1016/0003-4916(59)90002-8). URL <http://www.sciencedirect.com/science/article/pii/0003491659900028>.
- [12] Glen L Goodvin, Mona Berciu, and George A Sawatzky. Greens function of the holstein polaron. *Physical Review B*, 74(24):245104, 2006.
- [13] Mona Berciu and Glen L Goodvin. Systematic improvement of the momentum average approximation for the greens function of a holstein polaron. *Physical Review B*, 76(16):165109, 2007.
- [14] Glen L. Goodvin and Mona Berciu. Momentum average approximation for models with electron-phonon coupling dependent on the phonon momentum. *Phys. Rev. B*, 78:235120, Dec 2008. doi: 10.1103/PhysRevB.78.235120. URL <http://link.aps.org/doi/10.1103/PhysRevB.78.235120>.
- [15] Gerald D Mahan. *Many-particle physics*. Springer Science & Business Media, 2013.

Bibliography

- [16] Andrea Damascelli, Zahid Hussain, and Zhi-Xun Shen. Angle-resolved photoemission studies of the cuprate superconductors. *Rev. Mod. Phys.*, 75:473–541, Apr 2003. doi: 10.1103/RevModPhys.75.473. URL <http://link.aps.org/doi/10.1103/RevModPhys.75.473>.
- [17] Hadi Ebrahimnejad. *Variational studies of dressed quasiparticles properties and their interactions with external potentials*. PhD thesis, University of British Columbia, Dec 2014. URL <https://open.library.ubc.ca/cIRcle/collections/24/items/1.0166096>.
- [18] Richard D Mattuck. *A guide to Feynman diagrams in the many-body problem*. Courier Corporation, 2012.
- [19] C. Slezak, A. Macridin, G. A. Sawatzky, M. Jarrell, and T. A. Maier. Spectral properties of holstein and breathing polarons. *Phys. Rev. B*, 73:205122, May 2006. doi: 10.1103/PhysRevB.73.205122. URL <http://link.aps.org/doi/10.1103/PhysRevB.73.205122>.
- [20] William H Press. *Numerical recipes 3rd edition: The art of scientific computing*. Cambridge university press, 2007.
- [21] Mona Berciu. Berciu replies:. *Phys. Rev. Lett.*, 98:209702, May 2007. doi: 10.1103/PhysRevLett.98.209702. URL <http://link.aps.org/doi/10.1103/PhysRevLett.98.209702>.
- [22] J.G. Bednorz and K.A. Mller. Possible high T_c superconductivity in the balacuo system. *Zeitschrift fr Physik B Condensed Matter*, 64 (2):189–193, 1986. ISSN 0722-3277. doi: 10.1007/BF01303701. URL <http://dx.doi.org/10.1007/BF01303701>.
- [23] J. Zaanen, G. A. Sawatzky, and J. W. Allen. Band gaps and electronic structure of transition-metal compounds. *Phys. Rev. Lett.*, 55:418–421, Jul 1985. doi: 10.1103/PhysRevLett.55.418. URL <http://link.aps.org/doi/10.1103/PhysRevLett.55.418>.
- [24] V. J. Emery. Theory of high- T_c superconductivity in oxides. *Phys. Rev.*

- Lett.*, 58:2794–2797, Jun 1987. doi: 10.1103/PhysRevLett.58.2794. URL <http://link.aps.org/doi/10.1103/PhysRevLett.58.2794>.
- [25] Masao Ogata and Hidetoshi Fukuyama. The t - j model for the oxide high- T_c superconductors. *Reports on Progress in Physics*, 71(3):036501, 2008. URL <http://stacks.iop.org/0034-4885/71/i=3/a=036501>.
- [26] F. C. Zhang and T. M. Rice. Effective hamiltonian for the superconducting cu oxides. *Phys. Rev. B*, 37:3759–3761, Mar 1988. doi: 10.1103/PhysRevB.37.3759. URL <http://link.aps.org/doi/10.1103/PhysRevB.37.3759>.
- [27] H. Eskes and G. A. Sawatzky. Tendency towards local spin compensation of holes in the high- T_c copper compounds. *Phys. Rev. Lett.*, 61:1415–1418, Sep 1988. doi: 10.1103/PhysRevLett.61.1415. URL <http://link.aps.org/doi/10.1103/PhysRevLett.61.1415>.
- [28] K A Chao, J Spalek, and A M Oles. Kinetic exchange interaction in a narrow s -band. *Journal of Physics C: Solid State Physics*, 10(10):L271, 1977. URL <http://stacks.iop.org/0022-3719/10/i=10/a=002>.
- [29] K. A. Chao, J. Spalek, and A. M. Oleś. Canonical perturbation expansion of the hubbard model. *Phys. Rev. B*, 18:3453–3464, Oct 1978. doi: 10.1103/PhysRevB.18.3453. URL <http://link.aps.org/doi/10.1103/PhysRevB.18.3453>.
- [30] Masao Ogata and Hiroyuki Shiba. Holes in two-dimensional cuo_2 system pairing mechanism emerging from small-cluster studies. *Journal of the Physical Society of Japan*, 57(9):3074–3088, 1988. doi: 10.1143/JPSJ.57.3074. URL <http://dx.doi.org/10.1143/JPSJ.57.3074>.
- [31] A. I. Lichtenstein and M. I. Katsnelson. Antiferromagnetism and d -wave superconductivity in cuprates: A cluster dynamical mean-field theory. *Phys. Rev. B*, 62:R9283–R9286, Oct 2000. doi: 10.1103/PhysRevB.62.R9283. URL <http://link.aps.org/doi/10.1103/PhysRevB.62.R9283>.

- [32] E. Pavarini, I. Dasgupta, T. Saha-Dasgupta, O. Jepsen, and O. K. Andersen. Band-structure trend in hole-doped cuprates and correlation with t_{cmax} . *Phys. Rev. Lett.*, 87:047003, Jul 2001. doi: 10.1103/PhysRevLett.87.047003. URL <http://link.aps.org/doi/10.1103/PhysRevLett.87.047003>.
- [33] O.K. Andersen, A.I. Liechtenstein, O. Jepsen, and F. Paulsen. {LDA} energy bands, low-energy hamiltonians, t , t , t (k), and j . *Journal of Physics and Chemistry of Solids*, 56(12):1573 – 1591, 1995. ISSN 0022-3697. doi: [http://dx.doi.org/10.1016/0022-3697\(95\)00269-3](http://dx.doi.org/10.1016/0022-3697(95)00269-3). URL <http://www.sciencedirect.com/science/article/pii/0022369795002693>. Proceedings of the Conference on Spectroscopies in Novel Superconductors.
- [34] H. Eskes and G. A. Sawatzky. Single-, triple-, or multiple-band hubbard models. *Phys. Rev. B*, 44:9656–9666, Nov 1991. doi: 10.1103/PhysRevB.44.9656. URL <http://link.aps.org/doi/10.1103/PhysRevB.44.9656>.
- [35] Hiroyuki Matsui, Andrei S. Mishchenko, and Tatsuo Hasegawa. Distribution of localized states from fine analysis of electron spin resonance spectra in organic transistors. *Phys. Rev. Lett.*, 104:056602, Feb 2010. doi: 10.1103/PhysRevLett.104.056602. URL <http://link.aps.org/doi/10.1103/PhysRevLett.104.056602>.
- [36] S. Ciuchi and S. Fratini. Band dispersion and electronic lifetimes in crystalline organic semiconductors. *Phys. Rev. Lett.*, 106:166403, Apr 2011. doi: 10.1103/PhysRevLett.106.166403. URL <http://link.aps.org/doi/10.1103/PhysRevLett.106.166403>.
- [37] A Lanzara, PV Bogdanov, XJ Zhou, SA Kellar, DL Feng, ED Lu, T Yoshida, H Eisaki, Atsushi Fujimori, K Kishio, et al. Evidence for ubiquitous strong electron–phonon coupling in high-temperature superconductors. *Nature*, 412(6846):510–514, 2001.

- [38] KM Shen, F Ronning, DH Lu, WS Lee, NJC Ingle, W Meevasana, F Baumberger, A Damascelli, NP Armitage, LL Miller, et al. Missing quasiparticles and the chemical potential puzzle in the doping evolution of the cuprate superconductors. *Physical review letters*, 93(26): 267002, 2004.
- [39] Dmitri Reznik, L Pintschovius, M Ito, S Iikubo, M Sato, H Goka, M Fujita, K Yamada, GD Gu, and JM Tranquada. Electron–phonon coupling reflecting dynamic charge inhomogeneity in copper oxide superconductors. *Nature*, 440(7088):1170–1173, 2006.
- [40] Jinho Lee, K Fujita, K McElroy, JA Slezak, M Wang, Y Aiura, H Bando, M Ishikado, T Masui, J-X Zhu, et al. Interplay of electron–lattice interactions and superconductivity in $\text{Bi}_2\text{Sr}_2\text{CaCu}_2\text{O}_{8+\delta}$. *Nature*, 442(7102):546–550, 2006.
- [41] C Gadermaier, AS Alexandrov, VV Kabanov, P Kusar, T Mertelj, X Yao, C Manzoni, D Brida, G Cerullo, and D Mihailovic. Electron-phonon coupling in high-temperature cuprate superconductors determined from electron relaxation rates. *Physical review letters*, 105(25): 257001, 2010.
- [42] O Gunnarsson and O Rösch. Interplay between electron–phonon and coulomb interactions in cuprates. *Journal of Physics: Condensed Matter*, 20(4):043201, 2008.
- [43] Norman Mannella, Wanli L Yang, Xing Jiang Zhou, Hong Zheng, John F Mitchell, Jan Zaanen, Thomas P Devereaux, Naoto Nagaosa, Zahid Hussain, and Z-X Shen. Nodal quasiparticle in pseudogapped colossal magnetoresistive manganites. *Nature*, 438(7067): 474–478, 2005.
- [44] T Yildirim, O Gülseren, JW Lynn, CM Brown, TJ Udovic, Q Huang, N Rogado, KA Regan, MA Hayward, JS Slusky, et al. Giant anharmonicity and nonlinear electron-phonon coupling in MgB_2 : a com-

- bined first-principles calculation and neutron scattering study. *Physical review letters*, 87(3):037001, 2001.
- [45] Amy Y Liu, II Mazin, and Jens Kortus. Beyond eliashberg superconductivity in mgb 2: anharmonicity, two-phonon scattering, and multiple gaps. *Physical Review Letters*, 87(8):087005, 2001.
- [46] II Mazin and VP Antropov. Electronic structure, electron–phonon coupling, and multiband effects in mgb 2. *Physica C: Superconductivity*, 385(1):49–65, 2003.
- [47] Hyoung Joon Choi, David Roundy, Hong Sun, Marvin L Cohen, and Steven G Louie. The origin of the anomalous superconducting properties of mgb2. *Nature*, 418(6899):758–760, 2002.
- [48] A Kaminski, M Randeria, JC Campuzano, MR Norman, H Fretwell, J Mesot, T Sato, T Takahashi, and K Kadowaki. Renormalization of spectral line shape and dispersion below T_c in $\text{Bi}_2\text{Sr}_2\text{CaCu}_2\text{O}_{8+\delta}$. *Physical Review Letters*, 86(6):1070, 2001.
- [49] TK Kim, AA Kordyuk, SV Borisenko, A Koitzsch, M Knupfer, H Berger, and J Fink. Doping dependence of the mass enhancement in $(\text{Pb}, \text{Bi})_2\text{Sr}_2\text{CaCu}_2\text{O}_8$ at the antinodal point in the superconducting and normal states. *Physical review letters*, 91(16):167002, 2003.
- [50] C. N. Veenstra, G. L. Goodvin, M. Berciu, and A. Damascelli. Spectral function tour of electron-phonon coupling outside the migdal limit. *Phys. Rev. B*, 84:085126, Aug 2011. doi: 10.1103/PhysRevB.84.085126. URL <http://link.aps.org/doi/10.1103/PhysRevB.84.085126>.
- [51] H. Frhlich. Electrons in lattice fields. *Advances in Physics*, 3(11):325–361, 1954. doi: 10.1080/00018735400101213. URL <http://dx.doi.org/10.1080/00018735400101213>.

- [52] AS Mishchenko and Naoto Nagaosa. Electron-phonon coupling and a polaron in the t- j model: From the weak to the strong coupling regime. *Physical review letters*, 93(3):036402, 2004.
- [53] AS Mishchenko, N Nagaosa, Z-X Shen, G De Filippis, V Cataudella, TP Devereaux, Christian Bernhard, Kyung Wan Kim, and J Zaanen. Charge dynamics of doped holes in high t c cuprate superconductors: a clue from optical conductivity. *Physical review letters*, 100(16):166401, 2008.
- [54] Felipe Herrera and Roman V Krems. Tunable holstein model with cold polar molecules. *Physical Review A*, 84(5):051401, 2011.
- [55] JP Hague and C MacCormick. Quantum simulation of electron-phonon interactions in strongly deformable materials. *New Journal of Physics*, 14(3):033019, 2012.
- [56] Vladimir M Stojanović, Tao Shi, C Bruder, and J Ignacio Cirac. Quantum simulation of small-polaron formation with trapped ions. *Physical review letters*, 109(25):250501, 2012.
- [57] Felipe Herrera, Kirk W. Madison, Roman V. Krems, and Mona Berciu. Investigating polaron transitions with polar molecules. *Phys. Rev. Lett.*, 110:223002, May 2013. doi: 10.1103/PhysRevLett.110.223002. URL <http://link.aps.org/doi/10.1103/PhysRevLett.110.223002>.
- [58] O Entin-Wohlman, H Gutfreund, and M Weger. Mass and frequency renormalization for quadratic electron-phonon coupling. *Solid State Communications*, 46(1):1–5, 1983.
- [59] O Entin-Wohlman, H Gutfreund, and M Weger. Band narrowing and susceptibility enhancement by a quadratic electron-phonon interaction. *Journal of Physics C: Solid State Physics*, 18(3):L61, 1985.
- [60] Vincent H Crespi and Marvin L Cohen. Anharmonic phonons and

- high-temperature superconductivity. *Physical Review B*, 48(1):398, 1993.
- [61] VM Kenkre. What do polarons owe to their harmonic origins? *Physica D: Nonlinear Phenomena*, 113(2):233–241, 1998.
- [62] C. P. J. Adolphs and M. Berciu. Going beyond the linear approximation in describing electron-phonon coupling: Relevance for the holstein model. *EPL (Europhysics Letters)*, 102(4):47003, 2013. URL <http://stacks.iop.org/0295-5075/102/i=4/a=47003>.
- [63] H Fehske and SA Trugman. Numerical solution of the holstein polaron problem. In *Polarons in Advanced Materials*, pages 393–461. Springer, 2007.
- [64] G Herzberg. Dissociation energy and ionization potential of molecular hydrogen. *Physical review letters*, 23(19):1081, 1969.
- [65] Christopher Gerry and Peter Knight. *Introductory quantum optics*. Cambridge university press, 2005.
- [66] David Stoler. Equivalence classes of minimum uncertainty packets. *Physical Review D*, 1(12):3217, 1970.
- [67] J Bonca, T Katrasnik, and SA Trugman. Mobile bipolaron. *Physical review letters*, 84(14):3153, 2000.
- [68] Alexandru Macridin, GA Sawatzky, and Mark Jarrell. Two-dimensional hubbard-holstein bipolaron. *Physical Review B*, 69(24):245111, 2004.
- [69] AR Davenport, JP Hague, and PE Kornilovitch. Mobile small bipolarons on a three-dimensional cubic lattice. *Physical Review B*, 86(3):035106, 2012.
- [70] Shaozhi Li and S. Johnston. The effects of non-linear electron-phonon interactions on superconductivity and charge-density-wave correlations. *Europhysics Letters*, 109:27007, 2015.

- [71] Shaozhi Li, EA Nowadnick, and S Johnston. Quasiparticle properties of the nonlinear holstein model at finite doping and temperature. *Physical Review B*, 92(6):064301, 2015.
- [72] Y. Zolotaryuk, P. L. Christiansen, and J. Juul Rasmussen. Polaron dynamics in a two-dimensional anharmonic holstein model. *Phys. Rev. B*, 58:14305–14319, Dec 1998. doi: 10.1103/PhysRevB.58.14305. URL <http://link.aps.org/doi/10.1103/PhysRevB.58.14305>.
- [73] S Raghavan and V M Kenkre. Quantum mechanical bound rotator as a generalized harmonic oscillator. *Journal of Physics: Condensed Matter*, 6(47):10297, 1994. URL <http://stacks.iop.org/0953-8984/6/i=47/a=013>.
- [74] N. K. Voulgarakis and G. P. Tsironis. Stationary and dynamical properties of polarons in the anharmonic holstein model. *Phys. Rev. B*, 63:014302, Dec 2000. doi: 10.1103/PhysRevB.63.014302. URL <http://link.aps.org/doi/10.1103/PhysRevB.63.014302>.
- [75] P. Maniadis, G. Kalosakas, K. Ø. Rasmussen, and A. R. Bishop. Polaron normal modes in the peyrard-bishop-holstein model. *Phys. Rev. B*, 68:174304, Nov 2003. doi: 10.1103/PhysRevB.68.174304. URL <http://link.aps.org/doi/10.1103/PhysRevB.68.174304>.
- [76] J. K. Freericks, M. Jarrell, and D. J. Scalapino. Holstein model in infinite dimensions. *Phys. Rev. B*, 48:6302–6314, Sep 1993. doi: 10.1103/PhysRevB.48.6302. URL <http://link.aps.org/doi/10.1103/PhysRevB.48.6302>.
- [77] D. Meyer, A. C. Hewson, and R. Bulla. Gap formation and soft phonon mode in the holstein model. *Phys. Rev. Lett.*, 89:196401, Oct 2002. doi: 10.1103/PhysRevLett.89.196401. URL <http://link.aps.org/doi/10.1103/PhysRevLett.89.196401>.
- [78] Keisuke Mitsumoto and Yoshiaki no. Phonon softening and double-well potential formation due to electronphonon interaction in heavy-fermion systems. *Physica C: Superconductivity*, 426431, Part 1:330

- 334, 2005. ISSN 0921-4534. doi: <http://dx.doi.org/10.1016/j.physc.2004.12.021>. URL <http://www.sciencedirect.com/science/article/pii/S092145340500273X>. Proceedings of the 17th International Symposium on Superconductivity (ISS 2004) Advances in Superconductivity {XVIIProceedings} of the 17th International Symposium on Superconductivity (ISS 2004).
- [79] A. Bussmann-Holder, A. Simon, and H. Büttner. Possibility of a common origin to ferroelectricity and superconductivity in oxides. *Phys. Rev. B*, 39:207–214, Jan 1989. doi: 10.1103/PhysRevB.39.207. URL <http://link.aps.org/doi/10.1103/PhysRevB.39.207>.
- [80] O. Rösch and O. Gunnarsson. Electron-phonon interaction in the t - j model. *Phys. Rev. Lett.*, 92:146403, Apr 2004. doi: 10.1103/PhysRevLett.92.146403. URL <http://link.aps.org/doi/10.1103/PhysRevLett.92.146403>.
- [81] Bayo Lau, Mona Berciu, and George A. Sawatzky. Single-polaron properties of the one-dimensional breathing-mode hamiltonian. *Phys. Rev. B*, 76:174305, Nov 2007. doi: 10.1103/PhysRevB.76.174305. URL <http://link.aps.org/doi/10.1103/PhysRevB.76.174305>.
- [82] S. Johnston, F. Vernay, B. Moritz, Z.-X. Shen, N. Nagaosa, J. Zaanen, and T. P. Devereaux. Systematic study of electron-phonon coupling to oxygen modes across the cuprates. *Phys. Rev. B*, 82:064513, Aug 2010. doi: 10.1103/PhysRevB.82.064513. URL <http://link.aps.org/doi/10.1103/PhysRevB.82.064513>.
- [83] O. S. Barišić. Calculation of excited polaron states in the holstein model. *Phys. Rev. B*, 69:064302, Feb 2004. doi: 10.1103/PhysRevB.69.064302. URL <http://link.aps.org/doi/10.1103/PhysRevB.69.064302>.
- [84] Mona Berciu. Momentum average approximations for the holstein polaron. *Canadian Journal of Physics*, 86(4):523–527, 2008.

- [85] A.S. Alexandrov. Superconducting polarons and bipolarons. In A.S. Alexandrov, editor, *Polarons in Advanced Materials*, volume 103 of *Springer Series in Materials Science*, pages 257–310. Springer Netherlands, 2007. ISBN 978-1-4020-6347-3. doi: 10.1007/978-1-4020-6348-0_7. URL http://dx.doi.org/10.1007/978-1-4020-6348-0_7.
- [86] J. Bonča and S. A. Trugman. Bipolarons in the extended holstein hubbard model. *Phys. Rev. B*, 64:094507, Aug 2001. doi: 10.1103/PhysRevB.64.094507. URL <http://link.aps.org/doi/10.1103/PhysRevB.64.094507>.
- [87] J. P. Hague, P. E. Kornilovitch, J. H. Samson, and A. S. Alexandrov. Superlight small bipolarons in the presence of a strong coulomb repulsion. *Phys. Rev. Lett.*, 98:037002, Jan 2007. doi: 10.1103/PhysRevLett.98.037002. URL <http://link.aps.org/doi/10.1103/PhysRevLett.98.037002>.
- [88] A. S. Alexandrov, J. H. Samson, and G. Sica. Superlight small bipolarons from realistic long-range coulomb and fröhlich interactions. *Phys. Rev. B*, 85:104520, Mar 2012. doi: 10.1103/PhysRevB.85.104520. URL <http://link.aps.org/doi/10.1103/PhysRevB.85.104520>.
- [89] J. P. Hague and P. E. Kornilovitch. Light and stable triplet bipolarons on square and triangular lattices. *Phys. Rev. B*, 82:094301, Sep 2010. doi: 10.1103/PhysRevB.82.094301. URL <http://link.aps.org/doi/10.1103/PhysRevB.82.094301>.
- [90] Clemens P. J. Adolphs and Mona Berciu. Single-polaron properties for double-well electron-phonon coupling. *Phys. Rev. B*, 89:035122, Jan 2014. doi: 10.1103/PhysRevB.89.035122. URL <http://link.aps.org/doi/10.1103/PhysRevB.89.035122>.
- [91] Eleftherios N Economou. Green’s functions in quantum physics. *Green’s Functions in Quantum Physics*., *Springer Series in Solid-State*

Sciences, Volume 7. ISBN 978-3-540-28838-1. Springer-Verlag Berlin Heidelberg, 2006, 1, 2006.

- [92] Mona Berciu. Few-particle green's functions for strongly correlated systems on infinite lattices. *Phys. Rev. Lett.*, 107:246403, Dec 2011. doi: 10.1103/PhysRevLett.107.246403. URL <http://link.aps.org/doi/10.1103/PhysRevLett.107.246403>.
- [93] G. A. Sawatzky. Quasiatomic auger spectra in narrow-band metals. *Phys. Rev. Lett.*, 39:504–507, Aug 1977. doi: 10.1103/PhysRevLett.39.504. URL <http://link.aps.org/doi/10.1103/PhysRevLett.39.504>.
- [94] S. A. Trugman. Interaction of holes in a hubbard antiferromagnet and high-temperature superconductivity. *Phys. Rev. B*, 37:1597–1603, Feb 1988. doi: 10.1103/PhysRevB.37.1597. URL <http://link.aps.org/doi/10.1103/PhysRevB.37.1597>.
- [95] P. W. Leung and R. J. Gooding. Dynamical properties of the single-hole $t - J$ model on a 32-site square lattice. *Phys. Rev. B*, 52:R15711–R15714, Dec 1995. doi: 10.1103/PhysRevB.52.R15711. URL <http://link.aps.org/doi/10.1103/PhysRevB.52.R15711>.
- [96] P. W. Leung, B. O. Wells, and R. J. Gooding. Comparison of 32-site exact-diagonalization results and arpes spectral functions for the antiferromagnetic insulator $\text{sr}_2\text{cuo}_2\text{cl}_2$. *Phys. Rev. B*, 56:6320–6326, Sep 1997. doi: 10.1103/PhysRevB.56.6320. URL <http://link.aps.org/doi/10.1103/PhysRevB.56.6320>.
- [97] B. O. Wells, Z. X. Shen, A. Matsuura, D. M. King, M. A. Kastner, M. Greven, and R. J. Birgeneau. e versus k relations and many body effects in the model insulating copper oxide $\text{sr}_2\text{cuo}_2\text{cl}_2$. *Phys. Rev. Lett.*, 74:964–967, Feb 1995. doi: 10.1103/PhysRevLett.74.964. URL <http://link.aps.org/doi/10.1103/PhysRevLett.74.964>.
- [98] Mirko Möller, George A. Sawatzky, and Mona Berciu. Magnon-mediated interactions between fermions depend strongly on the lat-

- tice structure. *Phys. Rev. Lett.*, 108:216403, May 2012. doi: 10.1103/PhysRevLett.108.216403. URL <http://link.aps.org/doi/10.1103/PhysRevLett.108.216403>.
- [99] Mirko Möller, George A. Sawatzky, and Mona Berciu. Role of the lattice structure in determining the magnon-mediated interactions between charge carriers doped into a magnetically ordered background. *Phys. Rev. B*, 86:075128, Aug 2012. doi: 10.1103/PhysRevB.86.075128. URL <http://link.aps.org/doi/10.1103/PhysRevB.86.075128>.
- [100] Bayo Lau, Mona Berciu, and George A. Sawatzky. High-spin polaron in lightly doped cuo₂ planes. *Phys. Rev. Lett.*, 106:036401, Jan 2011. doi: 10.1103/PhysRevLett.106.036401. URL <http://link.aps.org/doi/10.1103/PhysRevLett.106.036401>.
- [101] Wolter Siemons, Gertjan Koster, Dave H. A. Blank, Robert H. Hammond, Theodore H. Geballe, and Malcolm R. Beasley. Tetragonal cuo: End member of the 3d transition metal monoxides. *Phys. Rev. B*, 79:195122, May 2009. doi: 10.1103/PhysRevB.79.195122. URL <http://link.aps.org/doi/10.1103/PhysRevB.79.195122>.
- [102] D. Samal, Haiyan Tan, Y. Takamura, W. Siemons, Jo Verbeeck, G. Van Tendeloo, E. Arenholz, C. A. Jenkins, G. Rijnders, and Gertjan Koster. Direct structural and spectroscopic investigation of ultrathin films of tetragonal cuo: Six-fold coordinated copper. *EPL (Europhysics Letters)*, 105(1):17003, 2014. URL <http://stacks.iop.org/0295-5075/105/i=1/a=17003>.
- [103] W.A. Harrison. *Elementary Electronic Structure*. Elementary Electronic Structure. World Scientific, 1999. ISBN 9789810238957. URL <https://books.google.ca/books?id=eAfi3ajSTcUC>.
- [104] Christopher L. Henley. Ordering due to disorder in a frustrated vector antiferromagnet. *Phys. Rev. Lett.*, 62:2056–2059, Apr 1989. doi:

- 10.1103/PhysRevLett.62.2056. URL <http://link.aps.org/doi/10.1103/PhysRevLett.62.2056>.
- [105] P. Chandra, P. Coleman, and A. I. Larkin. Ising transition in frustrated heisenberg models. *Phys. Rev. Lett.*, 64:88–91, Jan 1990. doi: 10.1103/PhysRevLett.64.88. URL <http://link.aps.org/doi/10.1103/PhysRevLett.64.88>.
- [106] Cédric Weber, Luca Capriotti, Grégoire Misguich, Federico Becca, Maged Elhajal, and Frédéric Mila. Ising transition driven by frustration in a 2d classical model with continuous symmetry. *Phys. Rev. Lett.*, 91:177202, Oct 2003. doi: 10.1103/PhysRevLett.91.177202. URL <http://link.aps.org/doi/10.1103/PhysRevLett.91.177202>.
- [107] Cornelius Lanczos. *An iteration method for the solution of the eigenvalue problem of linear differential and integral operators*. United States Governm. Press Office, 1950.
- [108] L. H. Tjeng, B. Sinkovic, N. B. Brookes, J. B. Goedkoop, R. Hesper, E. Pellegrin, F. M. F. de Groot, S. Altieri, S. L. Hulbert, E. Shekel, and G. A. Sawatzky. *Spin* -resolved photoemission on *Anti* -ferromagnets: Direct observation of zhang-rice singlets in cuo. *Phys. Rev. Lett.*, 78:1126–1129, Feb 1997. doi: 10.1103/PhysRevLett.78.1126. URL <http://link.aps.org/doi/10.1103/PhysRevLett.78.1126>.
- [109] N. B. Brookes, G. Ghiringhelli, O. Tjernberg, L. H. Tjeng, T. Mizokawa, T. W. Li, and A. A. Menovsky. Detection of zhang-rice singlets using spin-polarized photoemission. *Phys. Rev. Lett.*, 87:237003, Nov 2001. doi: 10.1103/PhysRevLett.87.237003. URL <http://link.aps.org/doi/10.1103/PhysRevLett.87.237003>.
- [110] N. B. Brookes, G. Ghiringhelli, A.-M. Charvet, A. Fujimori, T. Kakeshita, H. Eisaki, S. Uchida, and T. Mizokawa. Stability of the zhang-rice singlet with doping in lanthanum strontium copper oxide across the superconducting dome and above. *Phys. Rev. Lett.*,

115:027002, Jul 2015. doi: 10.1103/PhysRevLett.115.027002. URL <http://link.aps.org/doi/10.1103/PhysRevLett.115.027002>.

- [111] Erik Koch. The lanczos method. In Eva Pavarini, Erik Koch, Dieter Vollhardt, and Alexander Lichtenstein, editors, *The LDA+DMFT approach to strongly correlated materials*, volume 1, 2011. URL <http://www.cond-mat.de/events/correl11/manuscript/Koch.pdf>.

Appendix A

Various formal methods

Appendix B

Appendix for Nonlinear Holstein Model

B.1 Free propagator for the quadratic model

The Hamiltonian whose diagonal (in real space) Green's function we need to compute is

$$\mathcal{H}_0 = \mathcal{H}_{el} + \mathcal{H}_{ph} + g_2 \sum_i c_i^\dagger c_i \left(2b_i^\dagger b_i + 1 \right).$$

We look at the Green's function

$$G_0(j-i, \omega - n\Omega) = \langle 0 | c_j b_i^n \hat{G}_0(\omega) (b_i^\dagger)^n c_i^\dagger | 0 \rangle,$$

which describes free propagation of an electron from the side of the phonon cloud to another site j . We split the Hamiltonian \mathcal{H}_0 as

$$\mathcal{H}_{00} = \mathcal{H}_{el} + \mathcal{H}_{ph} + g_2, \quad \mathcal{H}_{01} = 2g_2 \sum_i c_i^\dagger c_i b_i^\dagger b_i$$

B.2. Equations of motion for quartic model

and use Dyson's identity to obtain

$$\begin{aligned}
G_0(j-i, \omega - n\Omega) &= G_{00}(j-i, \omega - n\Omega - g_2) \\
&\quad + \sum_l \langle 0 | b_i^n c_j \hat{G}_0(\omega) H_1 c_l^\dagger (b_i^\dagger)^n | 0 \rangle \cdot G_{00}(l-i, \omega - n\Omega - g_2) \\
&= G_{00}(j-i, \omega - n\Omega - g_2) \\
&\quad + 2g_2 G_0(j-i, \omega; n) G_{00}(i-i, \omega - n\Omega - g_2) \\
&= \frac{G_{00}(j-i, \omega - n\Omega - g_2)}{1 - 2g_2 \tilde{g}_0(\omega - n\Omega - g_2)}.
\end{aligned}$$

$G_{00}(j-i, \omega) = \frac{1}{N} \sum_{\mathbf{k}} \frac{e^{i\mathbf{k} \cdot (\mathbf{R}_j - \mathbf{R}_i)}}{\omega - \epsilon_{\mathbf{k}} + i\eta}$ is the free propagator for the electron, and $\tilde{g}_0(\omega) = G_{00}(i-i, \omega)$ is a short-hand notation. The only dependence of G_0 on the distance of sites $j-i$ is in the free electron propagator G_{00} . For energies below the free tight-binding model's ground state energy, this quantity decays exponentially with distance $j-i$, which justifies the MA approximation [1].

$$G_0(j-i, \omega) \approx \delta_{ij} G_0(j-i, \omega).$$

With $\bar{g}_0(\omega - n\Omega) = G_0(i-i, \omega - n\Omega)$, we obtain

$$\bar{g}_0(\omega, n) = \frac{1}{[\tilde{g}_0(\omega - n\Omega - g_2)]^{-1} - 2g_2 n}. \quad (\text{B.1})$$

We can obtain $\bar{g}_0(\omega; n)$ for any lattice model whose single-electron propagator we can compute. This includes the tight-binding model in any dimension with next-neighbor and finite-range hopping [2].

B.2 Equations of motion for quartic model

In the quartic model, the el-ph coupling term is given by $\sum_{n=1}^4 g_n (b + b^\dagger)^n$. The equation of motion for the generalized Green's functions then depends on the expansion of these terms.

The first two terms have already been treated in the main text; they

B.2. Equations of motion for quartic model

reproduce the quadratic model. For the third and fourth term, we have to expand $(b + b^\dagger)^3$ and $(b + b^\dagger)^4$, respectively. This is a tedious and boring exercise in correctly applying the bosonic commutation relations to group all terms together. Once this is done, we see that the third-order term will link a propagator F_n to propagators $F_{n\pm 3}$ as well as $F_{n\pm 1}$. The latter comes from terms such as $b^\dagger b^2$ and $bb^\dagger b$ from the expansion, which changes the overall phonon number by -1 . Expanding the fourth-order bracket, then, shows that this term couples F_n to $F_{n\pm 4}$, $F_{n\pm 2}$ and F_n itself.

Hence, instead of having vectors W_n of size 2 and matrices $\alpha_n, \beta_n, \gamma_n$ of size 2×2 , we now have vectors of size 4 and matrices of size 4×4 , with $\mathbf{W}_n = (F_{4n-3}, F_{4n-2}, F_{4n-1}, F_{4n})$. Inserting the expansions for the various coupling terms into Dyson's identity then allows us again to collect the generalized propagators of the appropriate order to obtain an EOM in matrix form, where we give the matrix elements below, using the following notational conventions:

- $x^{\bar{n}} = x(x-1)(x-2)\dots(x-n+1)$.
- $g_0^n = g_0(\omega, n)$, with

$$g_0(\omega, n) = \left[\frac{1}{\bar{g}_0(\omega - n\Omega - g_2 - 3g_4)} - n \times (2g_2 + 6g_4 + 6ng_4) \right]^{-1}$$

and \bar{g}_0 being the bare free electron propagator.

B.2. Equations of motion for quartic model

With this, we can then write the non-zero matrix elements as follows:

$$\begin{aligned}
 \alpha_{11} &= g_0^{4n-3} \cdot (4n-3)^{\bar{4}} \cdot g_4 \\
 \alpha_{12} &= g_0^{4n-3} \cdot (4n-3)^{\bar{3}} \cdot g_3 \\
 \alpha_{13} &= g_0^{4n-3} \cdot (4n-3)^{\bar{2}} \cdot (g_2 + (16n-14)g_4) \\
 \alpha_{14} &= g_0^{4n-3} \cdot (4n-3) \cdot (g_1 + (12n-9)g_3) \\
 \alpha_{22} &= g_0^{4n-2} \cdot (4n-2)^{\bar{4}} \cdot g_4 \\
 \alpha_{23} &= g_0^{4n-2} \cdot (4n-2)^{\bar{3}} \cdot g_3 \\
 \alpha_{24} &= g_0^{4n-2} \cdot (4n-2)^{\bar{2}} \cdot (g_2 + (16n-10)g_4) \\
 \alpha_{33} &= g_0^{4n-1} \cdot (4n-1)^{\bar{4}} \cdot g_4 \\
 \alpha_{34} &= g_0^{4n-1} \cdot (4n-1)^{\bar{3}} \cdot g_3 \\
 \alpha_{44} &= g_0^{4n} \cdot (4n)^{\bar{4}} \cdot g_4
 \end{aligned}$$

$$\begin{aligned}
 \beta_{11} &= g_0^{4n-3} \cdot g_4 \\
 \beta_{21} &= g_0^{4n-2} \cdot g_3 \\
 \beta_{22} &= g_0^{4n-2} \cdot g_4 \\
 \beta_{31} &= g_0^{4n-1} \cdot (g_2 + (16n-4)g_4) \\
 \beta_{32} &= g_0^{4n-1} \cdot g_3 \\
 \beta_{33} &= g_0^{4n-1} \cdot g_4 \\
 \beta_{41} &= g_0^{4n} \cdot (g_1 + (12n+3)g_3) \\
 \beta_{41} &= g_0^{4n} \cdot (g_2 + (16n+6)g_4) \\
 \beta_{41} &= g_0^{4n} \cdot g_3 \\
 \beta_{41} &= g_0^{4n} \cdot g_4
 \end{aligned}$$

B.2. Equations of motion for quartic model

$$\begin{aligned}
\gamma_{11} &= 1 \\
\gamma_{12} &= -g_0^{4n-3} \cdot (g_1 + (12n - 6)g_3) \\
\gamma_{13} &= -g_0^{4n-3} \cdot (g_2 + (16n - 6)g_4) \\
\gamma_{14} &= -g_0^{4n-3} \cdot g_3 \\
\gamma_{21} &= -g_0^{4n-2} \cdot (4n - 2) \cdot (g_1 + (12n - 6)g_3) \\
\gamma_{22} &= 1 \\
\gamma_{23} &= -g_0^{4n-2} \cdot (g_1 + (12n - 3)g_3) \\
\gamma_{24} &= -g_0^{4n-2} \cdot (g_2 + (16n - 2)g_4) \\
\gamma_{31} &= -g_0^{4n-1} \cdot (4n - 1)^2 \cdot (g_2 + (16n - 4)g_4) \\
\gamma_{32} &= -g_0^{4n-1} \cdot (4n - 1) \cdot (g_1 + (12n - 3)g_3) \\
\gamma_{33} &= 1 \\
\gamma_{34} &= -g_0^{4n-1} \cdot (g_1 + 12ng_3) \\
\gamma_{41} &= -g_0^{4n} \cdot (4n)^3 \cdot g_3 \\
\gamma_{42} &= -g_0^{4n} \cdot (4n)^2 \cdot (g_2 + (16n - 2)g_4) \\
\gamma_{43} &= -g_0^{4n} \cdot (4n) \cdot (g_1 + 12ng_3) \\
\gamma_{44} &= 1
\end{aligned}$$

Then, the recursion defined by $\gamma_n \mathbf{W}_n = \alpha_n \mathbf{W}_{n-1} + \beta_n \mathbf{W}_{n+1}$ is solved in the same manner as outlined in the main text.

Appendix C

Appendix for Quadratic Holstein Model

C.1 Details for the even-sector

C.1.1 Coupling matrices

The matrices appearing in Eq. (3.11) are:

$$\begin{aligned}\gamma_n^-|_{11} &= 1 - \bar{g}_0(\omega - 4n\Omega)(8ng_2 + 24ng_4 + 96n^2g_4) \\ \gamma_n^-|_{12} &= -\bar{g}_0(\omega - 4n\Omega)(g_2 + 6g_4 + 16ng_4) \\ \gamma_n^-|_{21} &= -\bar{g}_0(\omega - (4n + 2)\Omega)((g_2 + 6g_4)(4n + 2)^2 + \\ &\quad 4g_4(4n + 2)^3) \\ \gamma_n^-|_{22} &= 1 - \bar{g}_0(\omega - (4n + 2)\Omega)((8n + 4)g_2 + \\ &\quad (24n + 12)g_4 + 24(2n + 1)^2g_4)\end{aligned}$$

$$\begin{aligned}\alpha_n^-|_{11} &= \bar{g}_0(\omega - 4n\Omega)(g_4(4n)^4) \\ \alpha_n^-|_{12} &= \bar{g}_0(\omega - 4n\Omega) \left((g_2 + 6g_4)(4n)^2 + 4g_4(4n)^3 \right) \\ \alpha_n^-|_{21} &= 0 \\ \alpha_n^-|_{22} &= \bar{g}_0(\omega - (4n + 2)\Omega) \left(g_4(4n + 2)^4 \right)\end{aligned}$$

$$\begin{aligned}
\beta_n^-|_{11} &= \bar{g}_0(\omega - 4n\Omega)g_4 \\
\beta_n^-|_{12} &= 0 \\
\beta_n^-|_{21} &= \bar{g}_0(\omega - (4n + 2)\Omega)(g_2 + 6g_4 + (16n + 8)g_4) \\
\beta_n^-|_{22} &= \bar{g}_0(\omega - (4n + 2)\Omega)g_4
\end{aligned}$$

The matrices for \neq sector are the same if we substitute $n \rightarrow n - 1/2$ everywhere except in the argument of $\bar{g}_0(\omega)$.

C.1.2 Manipulation of the EOMs

We can rewrite the EOM of F_1 by inserting the matrices A_1^- and A_1^\neq and collecting terms. This results in

$$\begin{aligned}
F_1(ij) &= G_0(j - i, \omega - 2\Omega) [a_0^- G(j) + a_1^- F_1^-(j)] \\
&\quad + \sum_{l \neq j} G_0(l - i, \omega - 2\Omega) a^\neq F_1^\neq(lj). \quad (\text{C.1})
\end{aligned}$$

where we omit the arguments k and ω for shorter notation. We give expressions for the various coefficients below. For now, we rewrite the EOM as

$$\begin{aligned}
F_1(ij) &= G_0(j - i, \omega - 2\Omega) \times \left[a_0^- G(j) + (a_1^- - a_1^\neq) F_1^-(j) \right] \\
&\quad + \sum_l G_0(l - i, \omega - 2\Omega) a^\neq F_1(lj). \quad (\text{C.2})
\end{aligned}$$

Defining $G_0(\omega)_{ij} := G_0(j - i, \omega)$, we can write this as a matrix product:

$$\begin{aligned}
\sum_l \left[\delta_{il} - a^\neq G_0(\omega - 2\Omega)_{il} \right] F_1(lj) &= \\
G_0(\omega - 2\Omega)_{ij} \left[a_0^- G(j) + (a_1^- - a_1^\neq) F_1(jj) \right]. &
\end{aligned}$$

We multiply this from the left with $G_0^{-1}(\omega - 2\Omega)$ and obtain

$$\sum_l \left[G_0^{-1}(\omega - 2\Omega)_{rl} - a^\neq \delta_{rl} \right] F_1(lj) = \delta_{rj} \left[a_0^\neq G(j) + (a_1^- - a^\neq) F_1(jj) \right].$$

Next, we use the fact that $G_0^{-1}(\omega - 2\Omega)_{rl} = \delta_{rl}(\omega - 2\Omega) - \hat{H}_{rl}$, so subtracting $a^\neq \delta_{rl}$ from this just shifts its frequency to obtain $G_0^{-1}(\omega - 2\Omega - a^\neq)_{rl}$. As a result:

$$F_1(ij) = G_0(\omega - 2\Omega - a^\neq)_{ij} \times \left[a_0^- G(j) + (a_1^- - a_1^\neq) F_1(jj) \right].$$

Since in the EOM for G we only require $F_1(jj)$, we solve for that diagonal element and obtain

$$F_1(jj) = \frac{\bar{g}_0(\omega - 2\Omega - a^\neq) a_0^- G(j)}{1 - \bar{g}_0(\omega - 2\Omega - a^\neq) (a_1^- - a_1^\neq)}.$$

The coefficients are obtained by just inserting the appropriate matrices A_n into the EOM and collecting terms:

$$\begin{aligned} a_0^- &= 2g_2 + 12g_4 + (g_2 + 14g_4) A_1^- |_{11} + g_4 A_1^- |_{21} \\ a_1^- &= 4g_2 + 36g_4 + (g_2 + 14g_4) A_2^- |_{12} + g_4 A_2^- |_{22} \\ a^\neq &= (g_2 + 6g_4) A_1^\neq |_{12} + g_4 A_1^\neq |_{22} \end{aligned}$$

Finally, $F_1(jj)$ are used in Eq. (3.7) to obtain $G(k, \omega)$.

C.2 Details for the odd-sector

C.2.1 Equations of Motion

Starting from the EOM for $G_{ijl}(\omega)$, we let \mathcal{H}_1 act on the states in those sums, to find for the diagonal state:

$$\mathcal{H}_1 c_l^\dagger b_l^\dagger |0\rangle = (2g_2 + 12g_4) c_l^\dagger b_l^\dagger |0\rangle + (g_2 + 10g_4) c_l^\dagger b_l^{\dagger,3} |0\rangle + g_4 c_l^\dagger b_l^{\dagger,5} |0\rangle$$

while for the off-diagonal ones:

$$\mathcal{H}_1 c_i^\dagger b_l^\dagger |0\rangle = (2g_2 + 6g_4) c_i^\dagger b_l^\dagger |0\rangle + (g_2 + 6g_4) c_i^\dagger b_l^{\dagger,2} b_l^\dagger |0\rangle + g_4 c_i^\dagger b_l^{\dagger,4} b_l^\dagger |0\rangle.$$

We now define the generalized Green functions as:

$$F_n(k, i, j, \omega) = \langle k | \hat{G}(\omega) c_i b_i^{\dagger,2n} b_j | 0 \rangle$$

so we always have the extra phonon at site j . The equation of motion for G then becomes: $G_{ijl}(\omega) = G_0(j - i, \omega - \Omega) + [(2g_2 + 12g_4)F_0^-(l) + (g_2 + 10g_4)F_1^-(l) + g_4F_2^-(l)]G_{iil} + \sum_{i' \neq l} [(2g_2 + 6g_4)F_0^\neq(i', l) + (g_2 + 6g_4)F_1^\neq(i', l) + g_4F_2^\neq(i', l)]G_0(i' - i, \omega - \Omega)$. Again, we start by separating the cases F_n^- and F_n^\neq . The resulting equations of motion for F_n^- are like those of the even-sector F_n^- with $n \rightarrow n + 1/2$, while those for F_n^\neq are like those of the even-sector F_n^\neq with $n \rightarrow n + 1$.

In the spirit of MA⁽²⁾, only the EOM for G , which already has one phonon present, is kept exact, while in the EOMs for all the F_n with $n \geq 1$ we approximate $G_0(i - j, \omega) \rightarrow \delta_{ij} \bar{g}_0(\omega)$. We introduce matrices $W_n = (F_{2n-1}, F_{2n})$. Again we obtain an equation like Eq. (3.11), where now:

$$\begin{aligned} \gamma_{11}^- &= 1 - \bar{g}_0(\omega - (4n - 1)\Omega) \left((4n - 1)(2g_2 + 6g_4 \right. \\ &\quad \left. + 6g_4(4n - 1)) \right) \\ \gamma_{12}^- &= -\bar{g}_0(\omega - (4n - 1)\Omega) (g_2 + 6g_4 + 4g_4(4n - 1)) \\ \gamma_{21}^- &= -\bar{g}_0(\omega - (4n + 1)\Omega) \left((4n + 1)^2 (g_2 + 6g_4) \right. \\ &\quad \left. + (4n + 1)^3 \cdot 4g_4 \right) \\ \gamma_{22}^- &= 1 - \bar{g}_0(\omega - (4n + 1)\Omega) (4n + 1) \\ &\quad \times (2g_2 + 6g_4 + 6g_4(4n + 1)) \end{aligned}$$

$$\begin{aligned}
\alpha_{11}^{\bar{\bar{}}} &= \bar{g}_0(\omega - (4n - 1)\Omega)(4n - 1)^4 g_4 \\
\alpha_{12}^{\bar{\bar{}}} &= \bar{g}_0(\omega - (4n - 1)\Omega) \\
&\quad \times \left((4n - 1)^2(g_2 + 6g_4) + (4n - 1)^3 \cdot 4g_4 \right) \\
\alpha_{21}^{\bar{\bar{}}} &= 0 \\
\alpha_{22}^{\bar{\bar{}}} &= \bar{g}_0(\omega - (4n + 1)\Omega)(4n + 1)^4 g_4 \\
\\
\beta_{11}^{\bar{\bar{}}} &= \bar{g}_0(\omega - (4n - 1)\Omega)g_4 \\
\beta_{12}^{\bar{\bar{}}} &= 0 \\
\beta_{21}^{\bar{\bar{}}} &= \bar{g}_0(\omega - (4n + 1)\Omega)(g_2 + 6g_4 + 4g_4(4n + 1)) \\
\beta_{22}^{\bar{\bar{}}} &= \bar{g}_0(\omega - (4n + 1)\Omega)g_4
\end{aligned}$$

The matrices for W_n^{\neq} are obtained from these by replacing $n \rightarrow n - 1/4$ everywhere except in the argument of \bar{g}_0 . The remaining steps are in close analogy to those for obtaining the even-sector Green's function and not reproduced here.

The coefficients occurring in the final results for the odd-sector Green's function are

$$\begin{aligned}
a_o^{\bar{\bar{}}} &= 2g_2 + 12g_4 + (g_2 + 10g_4)A_1^{\bar{\bar{}}}|_{1,2} + g_4A_1^{\bar{\bar{}}}|_{2,2} \\
a_o^{\neq} &= (g_2 + 6g_4)A_1^{\neq}|_{1,2} + g_4A_1^{\neq}|_{2,2}.
\end{aligned}$$

C.2.2 Momentum space Green's functions

Rather than having the phonon present at a lattice site l , we can construct an electron-phonon state of total momentum K as

$$|K, n\rangle = \sum_i e^{iKR_i} / \sqrt{N} c_i^\dagger b_{i+n}^\dagger |0\rangle$$

where n is the relative electron-phonon distance. It is easy to show that $\langle K, m | \hat{G}(\omega) | K, n \rangle = G_{i, i+n-m, i+n}(\omega) \exp(iKa(n-m))$ where a is the lattice constant. In particular, the odd-polaron propagator $n = m = 0$ is just the

C.3. Quadratic e-ph coupling with $g_2 > 0$

completely local real space propagator $G_{iii}(\omega)$. In other words, the odd-sector polaron shows no dispersion at all.

Another Green's function of interest is given by

$$\langle k', q' | \hat{G}(\omega) | k, q \rangle = \langle 0 | c_{k'} b_{q'} \hat{G}(\omega) b_q^\dagger c_k^\dagger | 0 \rangle$$

where we insert an electron of momentum k into a system where the phonon has momentum q . Conservation of total momentum demands that $k + q = k' + q'$. It is again easy to show that the resulting propagator is

$$\begin{aligned} \langle k', q' | \hat{G}(\omega) | k, q \rangle = \\ \delta_{kk'} \delta_{qq'} G_0(k, \tilde{\omega}) + \frac{1}{N} G_0(k', \tilde{\omega}) G_0(k, \omega) \cdot \frac{a_o^- - a_0^\neq}{1 - \bar{g}_0(\tilde{\omega})(a_o^- - a_0^\neq)}. \end{aligned}$$

Since the latter term vanishes in the thermodynamic limit $N \rightarrow \infty$, we are left with just the even-sector polaron propagator. This is to be expected: In an infinite system, an electron does not scatter off a single impurity. If instead we assume a finite but low density n_p of phonons, the prefactor $1/N$ in the scattering term is replaced with n_p .

This brief analysis shows that the interesting physics of the odd phonon number sector are best observed in real space.

C.3 Quadratic e-ph coupling with $g_2 > 0$

Fig. C.1 shows that for $g_2 > 0$, $g_4 = 0$, the e-ph coupling has an extremely weak effect even in the atomic limit $t = 0$, since the quasiparticle weight Z remains very close to 1 while the average number of phonons is very small. An explanation for this behaviour is sketched in Fig. C.2: in the linear Holstein model, the carrier displaces the harmonic lattice potential of its site, as sketched in the left panel. The overlap between the ground state wavefunctions of the original and the displaced potentials is then the overlap between the tails of two Gaussians with different centers, which decreases exponentially with increasing displacement. Indeed, in the atomic limit for

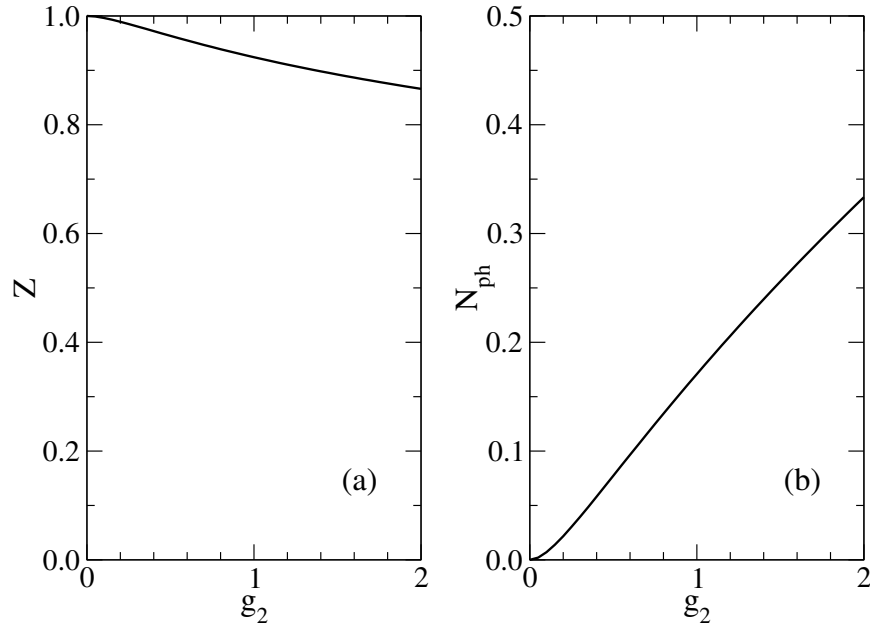


Figure C.1: a) Quasiparticle weight Z , and (b) average number of phonons for a quadratic model with $g_2 > 0, g_4 = 0$ in the atomic limit $t = 0$, for $\Omega = 1$.

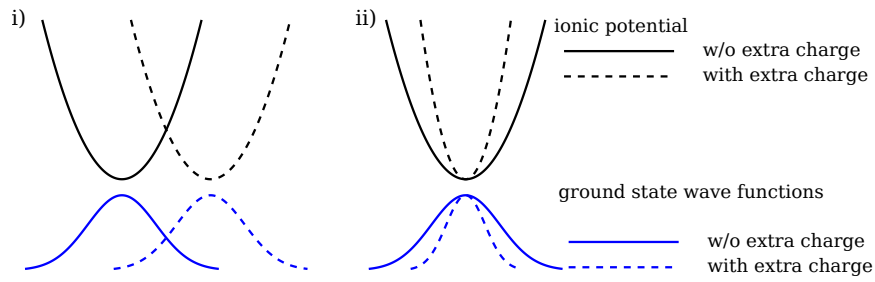


Figure C.2: Sketch of the lattice potential for i) Holstein, and ii) $g_2 > 0$ quadratic models. Full (dashed) lines indicate ionic potential and ground state wavefunction without (with) an extra charge on the site.

the linear Holstein model $Z \sim \exp[-(g/\Omega)^2]$. In the purely quadratic model with positive g_2 , however, the electron merely changes the shape of the well by increasing Ω to Ω_{at} . The overlap between the ground states of the original and modified potential is that of two Gaussians with the same center but different widths. We can calculate this overlap analytically to find

$$Z = \sqrt{1 - \left(\frac{\Omega - \Omega_{\text{at}}}{\Omega + \Omega_{\text{at}}^2}\right)^2} \quad (\text{C.3})$$

For $\Omega = 1.0$, even for $g_2 = 100\Omega$ we still have $Z \approx 0.42$. We conclude that a positive, purely quadratic electron-phonon coupling has negligible effect on the dynamics of a charge carrier. In particular, no crossover into the small polaron regime occurs for positive g_2 for any reasonable coupling strength. Finite t results (not shown) fully support this conclusion.

Appendix D

Appendix for T-CuO

D.1 Exact Diagonalization with Lanczos

The Lanczos algorithm is an efficient method for computing the ground-state and spectral function of a Hamiltonian, provided that the Hamiltonian is sparse, i.e., has a low number of matrix elements [107].

As an iterative method, the Hamiltonian \mathcal{H} enters the Lanczos method only in the computation of matrix-vector products $\mathcal{H}|\psi\rangle$. For many relevant models, the number of non-zero matrix elements per row is a small constant that does not grow with the system size. Therefore, the computational cost of the matrix vector product grows only linearly with the size of the Hilbert space. In contrast, the diagonalization of a dense matrix has a computational cost that grows as the third power of the Hilbert space [20]. Here we give just a very brief introduction to the Lanczos method and refer the reader to the extensive literature that exists on this algorithm.

At its core, the Lanczos method is a variational approach. Let H denote the matrix representation of some Hamiltonian \mathcal{H} . Then, H is diagonalized in a specially constructed subspace: We start with an arbitrary, randomly generated starting vector \mathbf{q}_0 . Then, we set

$$\mathbf{q}_{i+1} = \frac{H\mathbf{q}_i - \alpha_i\mathbf{q}_i - \beta_{i-1}\mathbf{q}_{i-1}}{\beta_i}$$

$$\text{with } \alpha_i = \langle \mathbf{q}_i | H | \mathbf{q}_i \rangle, \quad \beta_i = \|H\mathbf{q}_i - \alpha_i\mathbf{q}_i - \beta_{i-1}\mathbf{q}_{i-1}\|_2.$$

One can show that in the basis of the subspace spanned by the \mathbf{q}_i , the

Hamiltonian has matrix representation T where T is *tridiagonal*,

$$T = \begin{pmatrix} \alpha_0 & \beta_1 & & & \\ \beta_1 & \alpha_1 & \beta_2 & & \\ & \ddots & \ddots & \ddots & \\ & & \beta_{m-1} & \alpha_{m-1} & \beta_m \\ & & & \beta_m & \alpha_m \end{pmatrix}. \quad (\text{D.1})$$

The advantage of the Lanczos method, then, is that the matrix T can be diagonalized very efficiently with algorithms specialized for tridiagonal matrices [20], and that the extremal eigenvalues of T converge rapidly towards those of H , with m much smaller than the size of the full Hilbert space.

The Lanczos method can also be used to compute the spectral function by using as the starting vector not a randomly generated vector but instead the vector for which the spectral function is to be computed. Details of this method can be found in the literature. See for example the lecture notes from [111].